Real-space density functional theory adapted to cyclic and helical symmetry: Application to torsional deformation of carbon nanotubes

Abhiraj Sharma and Phanish Suryanarayana

Phys. Rev. B **103**, 035101 — Published 4 January 2021

DOI: 10.1103/PhysRevB.103.035101

Cyclic+helical symmetry-adapted real-space density functional theory: Application to torsional deformation of carbon nanotubes

Abhiraj Sharma, Phanish Suryanarayana*
College of Engineering, Georgia Institute of Technology, Atlanta, GA 30332, USA
(Dated: December 21, 2020)

We present a cyclic+helical symmetry-adapted formulation and large-scale parallel implementation of real-space Kohn-Sham density functional theory for 1D nanostructures, with application to the mechanical and electronic response of carbon nanotubes subject to torsional deformations. Specifically, employing a semilocal exchange-correlation and a local formulation of the electrostatics, we derive symmetry-adapted variants for the energy functional, variational problem governing the electronic ground state, Kohn-Sham equations, atomic forces, and axial stress, all posed on the fundamental domain. In addition, we develop a representation for twisted nanotubes of arbitrary chirality within this framework. We also develop a high-order finite-difference parallel implementation capable of performing accurate cyclic+helical symmetry-adapted Kohn-Sham calculations in both the static and dynamic setting, and verify it through numerical tests and comparisons with established codes. We use this implementation to perform twist-controlled simulations for a representative set of achiral and chiral carbon nanotubes, in both the small and large deformation regimes. In the linear regime, we find that the torsional moduli are proportional to the cube of the diameter; metallic nanotubes undergo metal-insulator transitions; and both the bandgap as well as effective mass of charge carriers are proportional to the shear strain and sine of thrice the chiral angle. In the nonlinear regime, we find that there is significant Poynting effect, particularly at the ultimate strain, the value of which is determined by the chiral angle; torsional deformations provide a possible mechanism for the irreversible phase transformation from armchair to zigzag nanotubes; and both the bandgap as well as effective mass have an oscillatory behavior, with the period for metal-insulator transitions being inversely proportional to the square of the diameter and sine of thrice the chiral angle. Wherever available, the results are in good agreement with experimental observations and measurements. Overall, the current work opens an avenue for the highly accurate and efficient first principles study of 1D nanostructures that have cyclic and/or helical symmetry, as well as their response to torsional deformations.

I. INTRODUCTION

Over the course of the past few decades, quantum mechanical calculations based on Kohn-Sham density functional theory (DFT)[1,2] have become a cornerstone of materials research by virtue of the unique insights they provide and predictive power they afford. The widespread use of Kohn-Sham DFT — calculations occupy a large fraction of high-performance computing resources around the world every day[3,4] — can be attributed to its generality, simplicity, and high accuracy-to-cost ratio relative to other such ab intio methods[5,6]. However, while less costly than wavefunction based alternatives, the solution of the Kohn-Sham equations remains a challenging task, severely restricting the range of physical systems that can be studied from the first principles of quantum mechanics. In particular, the computational cost and memory requirements for Kohn-Sham calculations generally scale cubically and quadratically with system size, respectively[7], the associated prefactor being particularly large for systematically improvable discretizations, generally the preferred choice for such simulations. In addition, the global nature of the orthonormality constraints on the orbitals limits parallel scalability on large-scale supercomputers[8]. These restrictions become even more acute in structural relaxation and quantum molecular dynamics simulations[5], wherein the Kohn-Sham equations may need to be solved tens to several thousands of times.

The planewave pseudopotential method[7] has been among the most widely used methods for the solution of the Kohn-Sham problem[9–13]. This is because the associated Fourier basis is complete, orthonormal, and provides spectral convergence for smooth problems, making the planewave method accurate, simple to use, and efficient on moderate computational resources through access to effective preconditioning schemes and highly optimized Fast Fourier Transforms. However, the Fourier basis restricts the method to periodic boundary conditions, whereby artificial periodicity is introduced for finite systems such as clusters as well as semi-infinite systems such as surfaces and nanotubes. Moreover, the global nature of the Fourier basis complicates the development of linear-scaling methods[14–16] and hinders scalability on parallel computing platforms, restricting the length and time scales accessible. These limitations have motivated the development of a number of alternative solution strategies that employ systematically improvable, localized representations[17–37]. Among these, perhaps the most mature and widely used to date are the finite-difference methods[38,39], wherein computational locality is maximized by discretizing all quantities on a uniform real-space grid. Convergence is therefore controlled by a single parameter and both periodic and Dirichlet boundary conditions are

naturally accommodated, thus enabling the efficient and accurate treatment of finite, semi-infinite, and bulk systems alike. Moreover, real-space methods are amenable to the development of linear scaling methods[40,41], and large-scale parallel computational resources can be efficiently leveraged by virtue of the method's simplicity, locality, and freedom from communication-heavy transforms[22,33,40–42]. Notably, real-space methods can now achieve substantially reduced solution times compared to established planewave codes in applications to both finite and extended systems.[8,34,43]

The structural symmetry of atomic systems also provides an attractive avenue for the significant reduction in both the cost of Kohn-Sham DFT calculations as well as the complexity associated with the analysis of its results. The most common form of symmetry that is regularly exploited by DFT implementations is translational symmetry, found in extended systems of various dimensionalities, such as crystals, surfaces, and nanotubes. In particular, the Kohn-Sham eigenproblem is reduced to a unit cell through the introduction of Bloch periodic boundary conditions on the orbitals, with the point group symmetries then used to reduce the region in reciprocal space over which Brillouin zone integration needs to be performed.[7] In so doing, the symmetry-adapted eigenproblems at the different Brillouin zone wavevectors can be solved independently of each other, which not only noticeably reduces the cost of computations, but also significantly improves its scaling on parallel machines. Since Kohn-Sham implementations employing systematically improvable discretizations generally work in affine coordinate systems, translational symmetry has been readily incorporated, given their underlying compatibility. However, most other symmetries commonly found in clusters/molecules and one-dimensional nanostructures are not compatible with affine coordinate systems, and therefore have not generally been incorporated/exploited. Note that such issues do not arise when the linear combination of atomic orbitals (LCAO)[44] approximation is used, since the basis is automatically compatible with the symmetry of the system[45,46], and therefore non-translational symmetries are regularly exploited in quantum chemistry codes[47,48].

One-dimensional nanostructures such as nanotubes, nanowires, and nanocoils have received increased attention over the past three decades due to their fascinating mechanical, electronic, optical, and thermal properties.[49] Indeed, such structures are not just limited to those synthesized in the laboratory, but are also commonly found in nature, e.g., DNA, viruses, and proteins. It is common for these systems to possess some form of non-translational symmetry, with cyclic and helical perhaps the most frequent among the symmorphic and non-symmorphic groups, respectively[50,51]. Even otherwise, the close association of bending deformations with cyclic symmetry[51,52], and torsional deformations with helical symmetry[51,52] make them ubiquitous while studying the response of nanostructures to mechanical deformations. Indeed, the tremendous simplication afforded by these symmetries has been exploited even in relatively inexpensive atomistic[51,53–56] and tight binding[52,57–66] calculations. In the context of Kohn-Sham DFT, cyclic+helical symmetry-adaption was first introduced within the real-space method as part of application-focused studies[67–69], however, details of the methodology are not available in literature. In view of this, a cyclic symmetry-adapted real-space formulation and implementation was recently developed for 1D nanostructures[70], which was subsequently extended to cyclic+translational symmetry[71]. This framework has most recently been modified, in concurrent development with the present work, to make it compatible with helical symmetry[72]. However, the formulation is limited to static calculations involving atomic relaxations alone, while being restricted to achiral[134] dipole-free[135] 1D nanostructures with atoms that have spherically symmetric nonlocal projectors, all in the context of local exchange-correlation functionals. Moreover, the implementation is in Matlab, which together with the aforementioned limitations, places restrictions on the physical applications that are accessible.

In this work, we present a cyclic+helical symmetry-adapted formulation and large-scale parallel implementation of real-space Kohn-Sham DFT for 1D nanostructures, with application to the mechanical and electronic response of carbon nanotubes subject to torsional deformations. Specifically, we derive symmetry-adapted variants for the energy functional, electronic ground state's variational problem, Kohn-Sham equations, atomic forces, and axial stress, all posed on the fundamental domain, while employing a semilocal exchange-correlation functional and a local electrostatic formulation. Within this framework, we develop a representation for nanotubes of arbitrary chirality subject to external twists. We develop a high-order finite-difference parallel implementation capable of performing cyclic+helical symmetry-adapted Kohn-Sham calculations in both the static and dynamic setting, and verify its accuracy through numerical tests and comparisons with standard codes. Using this implementaion, we study the mechanical and electronic response of carbon nanotubes to twist-controlled deformations, at both small and large deformations. In the linear regime, we find the torsional moduli to be proportional to the cube of the diameter; metallic nanotubes undergo metal-insulator transitions; and the bandgap as well as effective mass of charge carriers to be proportional to the shear strain and the sine of thrice the chiral angle. In the nonlinear regime, we find that there is significant Poynting effect, particularly at the chiral angle dependent ultimate strain; torsional deformations provide a possible mechanism for the irreversible phase transformation from armchair to zigzag nanotubes; and the bandgap as well as effective mass have an oscillatory behavior, with the period for metal-insulator transitions being inversely proportional to the square of the diameter and sine of thrice the chiral angle. To the best of our knowledge, these results are the first to be obtained in the context of ab initio methods, with the current work being the first to make predictions on the effective mass variations, Poynting effect at large deformations, and phase transformations through torsion, at any level of theory.

The remainder of this manuscript is organized as follows. In Section II, we provide the background for real-space DFT, which is used to develop the cyclic+helical symmetry-adapted formulation in Section III. Next, we describe the symmetry-adapted representation for twisted nanotubes of arbitrary chirality in Section IV. We then discuss the implementation of the proposed formulation in Section V, whose accuracy and performance are verified in Section VI. Next, we use the symmetry-adapted framework to study the effect of torsional deformations on carbon nanotubes in Section VII. Finally, we end with concluding remarks in Section VIII.

II. REAL-SPACE DFT

The energy functional in the framework of finite temperature Kohn-Sham DFT[2,73], while neglecting spin and employing the pseudopotential frozen-core approximation[7], can be written in the real-space formalism as[43]:

$$\mathcal{F}(\Psi,\mathbf{g},\phi,\mathbf{R}) = T_s(\Psi,\mathbf{g}) + E_{xc}(\rho,\nabla\rho) + E_{nl}(\Psi,\mathbf{g},\mathbf{R}) + E_{el}(\rho,\phi,\mathbf{R}) - S(\mathbf{g})\,, \tag{1}$$

where $\Psi = \{\psi_1,\psi_2,\ldots\}$ is the collection of Kohn-Sham orbitals with occupations $\mathbf{g} = \{g_1,g_2,\ldots\}$, ϕ is the electrostatic potential, $\mathbf{R} = \{\mathbf{R}_1,\mathbf{R}_2,\ldots\}$ is the collection of atomic positions, and ρ is the electron density:

$$\rho(\mathbf{x}) = 2\sum_n g_n|\psi_n(\mathbf{x})|^2\,. \tag{2}$$

In addition, T_s is the electronic kinetic energy, E_{xc} is a semilocal variant of the exchange-correlation energy, E_{nl} is the nonlocal pseudopotential energy, E_{el} is the total electrostatic energy, and S is the electronic entropy energy:

$$T_s(\Psi,\mathbf{g}) = 2\sum_n g_n\int_\Omega \psi_n^*(\mathbf{x})\left(-\frac{1}{2}\nabla^2\right)\psi_n(\mathbf{x})\,\mathrm{d}\mathbf{x}\,, \tag{3}$$

$$E_{xc}(\rho,\nabla\rho) = \int_\Omega \varepsilon_{xc}(\rho(\mathbf{x}),|\nabla\rho(\mathbf{x})|)\rho(\mathbf{x})\,\mathrm{d}\mathbf{x}\,, \tag{4}$$

$$E_{nl}(\Psi,\mathbf{g},\mathbf{R}) = 2\sum_n g_n\sum_J\sum_{p=1}^{\mathcal{P}_J}\gamma_{J;p}\left|\int_\Omega \chi_{J;p}^*(\mathbf{x},\mathbf{R}_J)\,\psi_n(\mathbf{x})\,\mathrm{d}\mathbf{x}\right|^2\,, \tag{5}$$

$$E_{el}(\rho,\phi,\mathbf{R}) = -\frac{1}{8\pi}\int_\Omega |\nabla\phi(\mathbf{x})|^2\,\mathrm{d}\mathbf{x} + \int_\Omega \big(\rho(\mathbf{x}) + b(\mathbf{x},\mathbf{R})\big)\phi(\mathbf{x})\,\mathrm{d}\mathbf{x} + E_{sc}(\mathbf{R})\,, \tag{6}$$

$$S(\mathbf{g}) = -2k_BT\sum_n \big(g_n\log g_n + (1-g_n)\log(1-g_n)\big)\,, \tag{7}$$

where Ω denotes the domain (with size approaching infinity), the superscript $(.)^*$ represents the complex conjugate, ε_{xc} is the exchange-correlation energy per particle, the summation index J runs over all atoms in Ω, $\mathcal{P}_J$ is the number of projectors associated with the J^{th} atom—described by functions $\chi_{J;p}$ with normalization factors $\gamma_{J;p}$, $b = \sum_J b_J$ is the total pseudocharge density of the nuclei, E_{sc} corrects for the self-interaction and overlap of the individual pseudocharge densities (Appendix A), and k_BT is the smearing, with k_B and T denoting the Boltzmann constant and electronic temperature, respectively.

The constrained variational problem for the electronic ground state can be written as[43]:

$$\min_{\Psi,\mathbf{g}}\max_{\phi}\mathcal{F}(\Psi,\mathbf{g},\phi,\mathbf{R}) \quad \text{s.t.} \quad \int_\Omega \psi_m^*(\mathbf{x})\psi_n(\mathbf{x})\,\mathrm{d}\mathbf{x} = \delta_{mn}\ \ \forall\, m,n\in\mathbb{N}; \quad \text{and} \quad 2\sum_n g_n = N_e\,, \tag{8}$$

where δ_{mn} is the Kronecker-delta function and N_e is the total number of electrons. The corresponding Kohn-Sham equations take the form:

$$\left(\mathcal{H} \equiv -\frac{1}{2}\nabla^2 + V_{xc} + \phi + V_{nl}\right)\psi_n = \lambda_n\psi_n\,, \quad n = 1,2,\ldots \tag{9}$$

$$g_n = \left(1+\exp\left(\frac{\lambda_n-\lambda_F}{k_BT}\right)\right)^{-1}, \qquad \lambda_F \ \text{is s.t.}\ 2\sum_n g_n = N_e\,, \tag{10}$$

$$-\frac{1}{4\pi}\nabla^2\phi(\mathbf{x},\mathbf{R}) = \rho(\mathbf{x}) + b(\mathbf{x},\mathbf{R})\,, \tag{11}$$

where $\mathcal{H}$ denotes the Hamiltonian with eigenfunctions ψ_n and eigenvalues λ_n, λ_F is the Fermi level, V_{xc} is the exchange-correlation potential:

$$V_{xc} = \frac{\delta E_{xc}}{\delta \rho} = \varepsilon_{xc} + \rho \frac{\partial \varepsilon_{xc}}{\partial \rho} - \nabla \cdot \left(\rho \frac{\partial \varepsilon_{xc}}{\partial (\nabla \rho)} \right) , \tag{12}$$

and V_{nl} is the nonlocal pseudopotential operator whose action on any function f is given by:

$$\left[V_{nl} f \right] (\mathbf{x}) = \sum_{J} \sum_{p=1}^{\mathcal{P}_J} \gamma_{J;p} \, \chi_{J;p}(\mathbf{x}, \mathbf{R}_J) \int_{\Omega} \chi^*_{J;p}(\mathbf{y}, \mathbf{R}_J) f(\mathbf{y}) \, \mathrm{d}\mathbf{y} \, . \tag{13}$$

Once the ground state has been determined, the real-space Hellmann-Feynman atomic forces[43] and stress tensor[74]—along the directions in which the system is extended—can be calculated to determine the structural ground state or perform quantum molecular dynamics (QMD) simulations.

III. CYCLIC+HELICAL SYMMETRY-ADAPTED REAL-SPACE DFT

In this section, we develop a cyclic+helical symmetry-adapted variant of the real-space Kohn-Sham DFT formulation outlined in the previous section. Specifically, we first develop a representation for the structure in terms of the underlying symmetry. Next, we discuss the impact of this symmetry on the electronic quantities, and use it to derive the symmetry-adapted variational problem on the fundamental domain. Thereafter, we derive the symmetry-adapted Kohn-Sham equations, the Hellmann-Feynman atomic forces, and the Hellmann-Feynman stress. Finally, we discuss the manifestation of time-reversal symmetry in the current context.

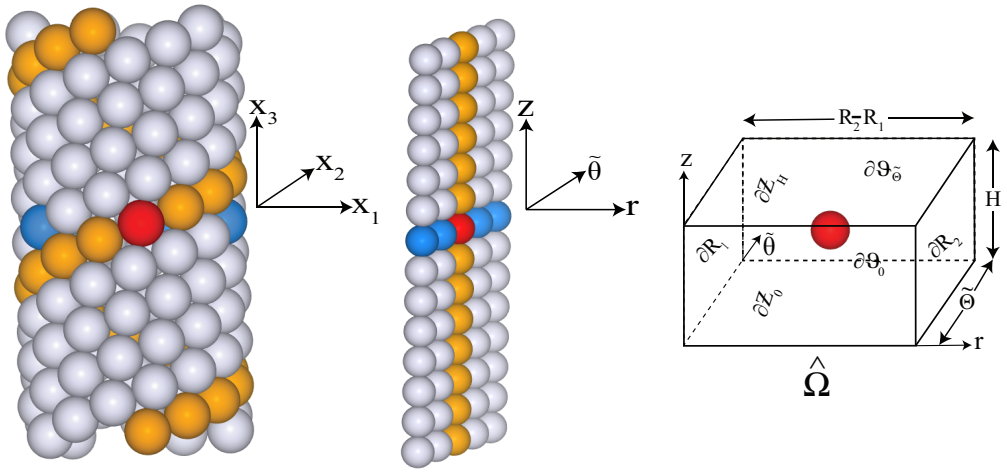

FIG. 1: Left: Illustration of a nanotube structure with cyclic+helical symmetry in Cartesian coordinates, where the *fundamental atom* is colored red and its cyclic and helical images are colored blue and yellow, respectively. Middle: The nanotube structure in helical coordinates. Right: *Fundamental domain* for the nanotube structure in the cyclic+helical symmetry-adapted real-space DFT formulation.

A. Structural symmetry

Consider an atomic structure which has cyclic+helical symmetry, as illustrated in Fig. 1. In such a system, the complete set of atoms can be represented as the orbit of the *fundamental atoms* under the action of the cyclic+helical symmetry group $\mathcal{G}$, i.e.,

$$\mathbf{R} = \bigcup_{J=1}^{N} \mathcal{G} \circ \hat{\mathbf{R}}_J = \bigcup_{J=1}^{N} \{ \Gamma_{\zeta,\mu} \circ \hat{\mathbf{R}}_J = \mathfrak{R}^{\zeta}_{\tilde{\Theta}} \mathfrak{R}^{\mu}_{\varphi} \hat{\mathbf{R}}_J + \mathbf{t}_{\mu} : \zeta = 0, 1, 2, \ldots, \mathfrak{N} - 1, \mu \in \mathbb{Z} \} \, , \tag{14}$$

where $\hat{\mathbf{R}}$ is the set of fundamental atoms with cardinality N, $\mathcal{G}\circ\hat{\mathbf{R}}_J$ is the orbit of the atom $\hat{\mathbf{R}}_J \in \hat{\mathbf{R}}$ under the action of the group:

$$\mathcal{G} = \{\Gamma_{\zeta,\mu} = (\mathfrak{R}^{\zeta}_{\tilde{\Theta}}|\mathbf{t}_0)(\mathfrak{R}^{\mu}_{\varphi}|\mathbf{t}_\mu) : (\mathfrak{R}^{\zeta}_{\tilde{\Theta}}|\mathbf{t}_0) \in \mathcal{C}, (\mathfrak{R}^{\mu}_{\varphi}|\mathbf{t}_\mu) \in \mathcal{S}, \zeta = 0,1,2,\ldots,\mathfrak{N}-1, \mu \in \mathbb{Z}\}\,, \tag{15}$$

written as the direct product of the cyclic and helical (or screw axis) symmetry groups $\mathcal{C}$ and $\mathcal{S}$, respectively[75]:

$$\mathcal{C} = \{(\mathfrak{R}^{\zeta}_{\tilde{\Theta}}|\mathbf{t}_0) : \zeta = 0,1,2,\ldots,\mathfrak{N}-1\}\,, \text{ with } \mathfrak{R}^{\zeta}_{\tilde{\Theta}} = \begin{pmatrix} \cos(\zeta\tilde{\Theta}) & -\sin(\zeta\tilde{\Theta}) & 0 \\ \sin(\zeta\tilde{\Theta}) & \cos(\zeta\tilde{\Theta}) & 0 \\ 0 & 0 & 1 \end{pmatrix}, \tag{16}$$

$$\mathcal{S} = \{(\mathfrak{R}^{\mu}_{\varphi}|\mathbf{t}_\mu) : \mu \in \mathbb{Z}\}\,, \text{with } \mathfrak{R}^{\mu}_{\varphi} = \begin{pmatrix} \cos(\mu\varphi) & -\sin(\mu\varphi) & 0 \\ \sin(\mu\varphi) & \cos(\mu\varphi) & 0 \\ 0 & 0 & 1 \end{pmatrix} \text{ and } \mathbf{t}_\mu = \begin{pmatrix} 0 \\ 0 \\ \mu H \end{pmatrix}. \tag{17}$$

Above, $(\mathfrak{R}^{\zeta}_{\tilde{\Theta}}|\mathbf{t}_0)$ associated with an integer ζ is a rigid body rotation whose action on a point rotates it by an angle $\zeta\tilde{\Theta}$ in the counter-clockwise sense about the screw axis, i.e, x_3-direction. Similarly, $(\mathfrak{R}^{\mu}_{\varphi}|\mathbf{t}_\mu)$ associated with the integer μ is an isometry (i.e., rigid body motion) whose action on a point rotates it by an angle $\mu\varphi$ in the counter-clockwise sense about the screw axis, while also simultaneously translating it by μH along the same axis.

B. Electronic symmetry

The real-space Kohn-Sham DFT problem is formulated in terms of the following electronic quantities: electron density ρ, pseudocharge density b, electrostatic potential ϕ, and Kohn-Sham orbitals Ψ. To develop a symmetry-adapted variant, it is necessary to understand the impact of the cyclic+helical structural symmetry on these electronic quantities. To do so, we start with the assumption that the electron density is commensurate with the structural symmetry: $\rho(\Gamma_{\zeta,\mu}\circ\mathbf{x}) = \rho(\mathbf{x}) \quad \forall\, \Gamma_{\zeta,\mu} \in \mathcal{G}$, an assumption that is necessary in the current context because of the inherently nonlinear nature of the Kohn-Sham problem. Indeed, as we show below, the cyclic+helical symmetry is maintained throughout the DFT simulation, provided that the initial guess for the electron density obeys this symmetry.

The pseudocharge density b can be shown to inherit the symmetry of the structure:

$$\begin{aligned} b(\Gamma_{\zeta,\mu}\circ\mathbf{x}, \hat{\mathbf{R}}, \mathcal{G}) &= \sum_{J=1}^{N}\sum_{\Gamma_{\zeta',\mu'}} b_J(\Gamma_{\zeta,\mu}\circ\mathbf{x}, \Gamma^{-1}_{\zeta',\mu'}\circ\hat{\mathbf{R}}_J) \\ &= \sum_{J=1}^{N}\sum_{\Gamma_{\zeta',\mu'}} b_J(\mathbf{x}, \Gamma^{-1}_{\zeta'+\zeta,\mu'+\mu}\circ\hat{\mathbf{R}}_J) \\ &= \sum_{J=1}^{N}\sum_{\Gamma_{\zeta',\mu'}} b_J(\mathbf{x}, \Gamma^{-1}_{\zeta',\mu'}\circ\hat{\mathbf{R}}_J) \\ &= b(\mathbf{x}, \hat{\mathbf{R}}, \mathcal{G}) \quad \forall\, \Gamma_{\zeta,\mu} \in \mathcal{G}\,, \end{aligned} \tag{18}$$

where the second and third equalities follow from the spherical symmetry and closure property of the symmetry group, respectively.

The electrostatic potential ϕ is the solution of the Poisson problem given in Eq. 11. Since the electron and pseudocharge densities appearing on the right hand side of this equation are commensurate with the structural symmetry, it follows that the electrostatic potential also inherits this symmetry:

$$\phi(\Gamma_{\zeta,\mu}\circ\mathbf{x}) = \phi(\mathbf{x}) \quad \forall\, \Gamma_{\zeta,\mu} \in \mathcal{G}\,, \tag{19}$$

which can be shown using the fact that the Laplacian commutes with the symmetry operations of the group $\mathcal{G}$ (Appendix B), and that the solution to the Poisson equation is unique[76].

The Kohn-Sham orbitals Ψ are eigenfunctions of the Hamiltonian $\mathcal{H}$, as described by Eq. 9. Since $\mathcal{H}$ commutes with the symmetry operations of the cyclic+helical group $\mathcal{G}$ (Appendix B), it follows that the symmetry-adapted orbitals transform as the irreducible representation of the group elements[75], satisfying the relation:

$$\psi_n(\Gamma_{\zeta,\mu}\circ\mathbf{x},\nu,\eta) = e^{i(\nu\zeta\tilde{\Theta}+\eta\mu H)}\psi_n(\mathbf{x},\nu,\eta)\,, \quad \nu \in \{0,1,2,\ldots,\mathfrak{N}-1\},\ \eta \in \left[-\frac{\pi}{H},\frac{\pi}{H}\right], \tag{20}$$

where $\frac{1}{\sqrt{|\mathcal{G}|}}\psi_n(\mathbf{x},\nu,\eta) \in \Psi$ is an orbital characterized by the wavevector (ν,η), with $|\mathcal{G}|$ denoting the order of $\mathcal{G}$. It therefore follows that $\mathcal{H}$ can be block-diagonalized using this symmetry-adapted basis and the eigenvalue problems associated with distinct wavevectors can be solved independently of one another. In view of this, we will henceforth label the eigenvalue and occupation corresponding to the orbital $\psi_n(\nu,\eta)$ by $\lambda_n(\nu,\eta)$ and $g_n(\nu,\eta)$, respectively.

The symmetry in the orbitals can be used to develop the following representation for the electron density:

$$\begin{aligned}\rho(\mathbf{x}) &= 2\sum_n g_n\,|\psi_n(\mathbf{x})|^2 \\ &= \frac{2}{|\mathcal{G}|}\sum_{\nu=0}^{\mathfrak{N}-1}\sum_{\eta}\sum_{n=1}^{N_{\nu,\eta}} g_n(\nu,\eta)\,|\psi_n(\mathbf{x},\nu,\eta)|^2 \\ &= \frac{2}{\mathfrak{N}}\sum_{\nu=0}^{\mathfrak{N}-1}\fint_{-\frac{\pi}{H}}^{\frac{\pi}{H}}\sum_{n=1}^{N_{\nu,\eta}} g_n(\nu,\eta)\,|\psi_n(\mathbf{x},\nu,\eta)|^2\,\mathrm{d}\eta\,,\end{aligned} \tag{21}$$

where $N_{\nu,\eta}$ represents the number of orbitals associated with the (ν,η) wavevector and $\fint$ denotes the average of the integral. The third equality in the above equation is obtained by replacing the infinite summation over η with an integral, a strategy that will used repeatedly henceforth. It then follows that the electron density is commensurate with the cyclic+helical symmetry of the structure, i.e.,

$$\rho(\Gamma_{\zeta,\mu}\circ\mathbf{x}) = \rho(\mathbf{x}) \quad \forall\ \Gamma_{\zeta,\mu}\in\mathcal{G}\,. \tag{22}$$

Therefore, the symmetry in the electron density is maintained throughout the solution of the symmetry-adapted Kohn-Sham problem, provided that the initial electron density has this symmetry, e.g., through superposition of isolated-atom electron densities, a strategy common to DFT implementations, including the one developed here.

C. Fundamental domain

The symmetry in the electronic quantities is naturally suited for implementation within a coordinate system that is compatible with the underlying cyclic+helical symmetry. In view of this, we choose a helical coordinate system[72,77] in which the coordinates $(r,\tilde{\theta},z)$ are related to their Cartesian counterparts (x_1,x_2,x_3) through the relations:

$$\begin{aligned} r &= \sqrt{x_1^2+x_2^2} \\ \tilde{\theta} &= \tan^{-1}\left(\frac{x_2}{x_1}\right) - \alpha x_3 + k\pi\,;\, k = \begin{cases} 0, & \text{if } x_1, x_2 \geq 0 \\ 1, & \text{if } x_1 < 0 \\ 2, & \text{otherwise} \end{cases} \\ z &= x_3\,, \end{aligned} \tag{23}$$

where $\alpha\in\mathbb{R}$ is the screw displacement or twist parameter, defined as the amount of counter-clockwise rotation about the screw axis as one translates along it in the positive direction by a unit length. In this coordinate system, based on the symmetry in the electronic quantities, the *fundamental domain* can be identified to be the cuboid (Fig. 1):

$$\hat{\Omega} := \left\{(r,\tilde{\theta},z)\in\mathbb{R}^3 \middle| 0<R_1\leq r\leq R_2, 0\leq\tilde{\theta}\leq\tilde{\Theta}\leq 2\pi, 0\leq z\leq H\right\}\,, \tag{24}$$

where an annular region is chosen in the radial direction to enable efficient solution for 1D nanostructures, the focus of this work. In addition, the maximum polar angle $\tilde{\Theta}=2\pi/\mathfrak{N}$, where $\mathfrak{N}\in\mathbb{N}$ is the order of the cyclic group $\mathcal{C}$. The boundary of Ω, denoted by $\partial\hat{\Omega}$, is the union of six faces of $\hat{\Omega}$ (Fig. 1):

$$\partial\hat{\Omega} = \partial R_1 \bigcup \partial R_2 \bigcup \partial\vartheta_0 \bigcup \partial\vartheta_{\tilde{\Theta}} \bigcup \partial\mathcal{Z}_0 \bigcup \partial\mathcal{Z}_H\,, \tag{25}$$

where ∂R_1 and ∂R_2 denote the surfaces $r=R_1$ and $r=R_2$, respectively; $\partial\vartheta_0$ and $\partial\vartheta_{\tilde{\Theta}}$ denote the surfaces $\tilde{\theta}=0$ and $\tilde{\theta}=\tilde{\Theta}$, respectively; and $\partial\mathcal{Z}_0$ and $\partial\mathcal{Z}_H$ denote the surfaces $z=0$ and $z=H$, respectively.

D. Symmetry-adapted energy functional

The symmetry in the electronic quantities is now used to reformulate the real-space Kohn-Sham energy functional (Eq. 1). Specifically, the symmetry-adapted energy functional over the fundamental domain $\hat{\Omega}$ can be written as:

$$\hat{\mathcal{F}}(\hat{\Psi},\hat{\mathbf{g}},\phi,\hat{\mathbf{R}},\mathcal{G}) = \hat{T}_s(\hat{\Psi},\hat{\mathbf{g}}) + \hat{E}_{xc}(\rho,\nabla\rho) + \hat{E}_{nl}(\hat{\Psi},\hat{\mathbf{g}},\hat{\mathbf{R}},\mathcal{G}) + \hat{E}_{el}(\rho,\phi,\hat{\mathbf{R}},\mathcal{G}) + \hat{S}(\hat{\mathbf{g}}) \tag{26}$$

where $\hat{\Psi}$ is the collection of symmetry-adapted orbitals $\psi_n(\mathbf{x},\nu,\eta)$, and $\hat{\mathbf{g}}$ is the collection of the corresponding occupations $g_n(\mathbf{x},\nu,\eta)$. We now derive the expressions for each of these symmetry-adapted energy terms.

The symmetry-adapted electronic kinetic energy $\hat{T}_s$ takes the form:

$$\begin{aligned}
\hat{T}_s(\hat{\Psi},\hat{\mathbf{g}}) &= \frac{1}{|\mathcal{G}|}T_s(\Psi,\mathbf{g}) \\
&= \frac{2}{|\mathcal{G}|^2}\sum_{\nu=0}^{\mathfrak{N}-1}\sum_{\eta}\sum_{n=1}^{N_{\nu,\eta}} g_n(\nu,\eta)\int_{\Omega}\psi_n^*(\mathbf{x},\nu,\eta)\left(-\frac{1}{2}\nabla^2\right)\psi_n(\mathbf{x},\nu,\eta)\,\mathrm{d}\mathbf{x} \\
&= \frac{2}{|\mathcal{G}|\mathfrak{N}}\sum_{\nu=0}^{\mathfrak{N}-1}\fint_{-\frac{\pi}{H}}^{\frac{\pi}{H}}\sum_{n=1}^{N_{\nu,\eta}} g_n(\nu,\eta)\int_{\Omega}\psi_n^*(\mathbf{x},\nu,\eta)\left(-\frac{1}{2}\nabla^2\right)\psi_n(\mathbf{x},\nu,\eta)\,\mathrm{d}\mathbf{x}\,\mathrm{d}\eta \\
&= \frac{2}{|\mathcal{G}|\mathfrak{N}}\sum_{\nu=0}^{\mathfrak{N}-1}\fint_{-\frac{\pi}{H}}^{\frac{\pi}{H}}\sum_{n=1}^{N_{\nu,\eta}} g_n(\nu,\eta)\left(\sum_{\Gamma_{\zeta,\mu}}\int_{\Gamma_{\zeta,\mu}\circ\hat{\Omega}}\psi_n^*(\mathbf{x},\nu,\eta)\left(-\frac{1}{2}\nabla^2\right)\psi_n(\mathbf{x},\nu,\eta)\,\mathrm{d}\mathbf{x}\right)\mathrm{d}\eta \\
&= \frac{2}{\mathfrak{N}}\sum_{\nu=0}^{\mathfrak{N}-1}\fint_{-\frac{\pi}{H}}^{\frac{\pi}{H}}\sum_{n=1}^{N_{\nu,\eta}} g_n(\nu,\eta)\int_{\hat{\Omega}}\psi_n^*(\mathbf{x},\nu,\eta)\left(-\frac{1}{2}\nabla^2\right)\psi_n(\mathbf{x},\nu,\eta)\,\mathrm{d}\mathbf{x}\,\mathrm{d}\eta\,,
\end{aligned} \tag{27}$$

where the last equality is obtained by using the symmetry of the orbitals (Eq. 20).

The symmetry-adapted exchange-correlation energy $\hat{E}_{xc}$ takes the form:

$$\begin{aligned}
\hat{E}_{xc}(\rho,\nabla\rho) &= \frac{1}{|\mathcal{G}|}E_{xc}(\rho,\nabla\rho) \\
&= \frac{1}{|\mathcal{G}|}\sum_{\Gamma_{\zeta,\mu}}\int_{\Gamma_{\zeta,\mu}\circ\hat{\Omega}}\varepsilon_{xc}(\rho(\mathbf{x}),|\nabla\rho(\mathbf{x})|)\rho(\mathbf{x})\,\mathrm{d}\mathbf{x} \\
&= \int_{\hat{\Omega}}\varepsilon_{xc}(\rho(\mathbf{x}),|\nabla\rho(\mathbf{x})|)\rho(\mathbf{x})\,\mathrm{d}\mathbf{x}\,,
\end{aligned} \tag{28}$$

where the last equality is obtained by using the symmetry in the electron density (Eq. 22).

The symmetry-adapted nonlocal pseudopotential energy $\hat{E}_{nl}$ takes the form:

$$\begin{aligned}
\hat{E}_{nl}(\hat{\Psi},\hat{\mathbf{g}},\hat{\mathbf{R}},\mathcal{G}) &= \frac{1}{|\mathcal{G}|}E_{nl}(\Psi,\mathbf{g},\mathbf{R}) \\
&= \frac{2}{|\mathcal{G}|^2}\sum_{\nu=0}^{\mathfrak{N}-1}\sum_{\eta}\sum_{n=1}^{N_{\nu,\eta}} g_n(\nu,\eta)\sum_{J}\sum_{p=1}^{\mathcal{P}_J}\gamma_{J;p}\left|\int_{\Omega}\chi_{J;p}^*(\mathbf{x},\mathbf{R}_J)\,\psi_n(\mathbf{x},\nu,\eta)\,\mathrm{d}\mathbf{x}\right|^2 \\
&= \frac{2}{|\mathcal{G}|}\sum_{\nu=0}^{\mathfrak{N}-1}\sum_{\eta}\sum_{n=1}^{N_{\nu,\eta}} g_n(\nu,\eta)\sum_{J=1}^{N}\sum_{p=1}^{\mathcal{P}_J}\gamma_{J;p}\left|\int_{\Omega}\chi_{J;p}^*(\mathbf{x},\hat{\mathbf{R}}_J)\,\psi_n(\mathbf{x},\nu,\eta)\,\mathrm{d}\mathbf{x}\right|^2 \\
&= \frac{2}{\mathfrak{N}}\sum_{\nu=0}^{\mathfrak{N}-1}\fint_{-\frac{\pi}{H}}^{\frac{\pi}{H}}\sum_{n=1}^{N_{\nu,\eta}} g_n(\nu,\eta)\sum_{J=1}^{N}\sum_{p=1}^{\mathcal{P}_J}\gamma_{J;p}\left|\int_{\Omega}\chi_{J;p}^*(\mathbf{x},\hat{\mathbf{R}}_J)\,\psi_n(\mathbf{x},\nu,\eta)\,\mathrm{d}\mathbf{x}\right|^2\mathrm{d}\eta \\
&= \frac{2}{\mathfrak{N}}\sum_{\nu=0}^{\mathfrak{N}-1}\fint_{-\frac{\pi}{H}}^{\frac{\pi}{H}}\sum_{n=1}^{N_{\nu,\eta}} g_n(\nu,\eta)\sum_{J=1}^{N}\sum_{p=1}^{\mathcal{P}_J}\gamma_{J;p}\left|\sum_{\Gamma_{\zeta,\mu}}\int_{\Gamma_{\zeta,\mu}\circ\hat{\Omega}}\chi_{J;p}^*(\mathbf{x},\hat{\mathbf{R}}_J)\psi_n(\mathbf{x},\nu,\eta)\mathrm{d}\mathbf{x}\right|^2\mathrm{d}\eta \\
&= \frac{2}{\mathfrak{N}}\sum_{\nu=0}^{\mathfrak{N}-1}\fint_{-\frac{\pi}{H}}^{\frac{\pi}{H}}\sum_{n=1}^{N_{\nu,\eta}} g_n(\nu,\eta)\sum_{J=1}^{N}\sum_{p=1}^{\mathcal{P}_J}\gamma_{J;p}\left|\sum_{\Gamma_{\zeta,\mu}}\int_{\hat{\Omega}}\chi_{J;p}^*(\Gamma_{\zeta,\mu}\circ\mathbf{x},\hat{\mathbf{R}}_J)\,e^{i(\nu\zeta\tilde{\Theta}+\eta\mu H)}\psi_n(\mathbf{x},\nu,\eta)\,\mathrm{d}\mathbf{x}\right|^2\mathrm{d}\eta
\end{aligned}$$

$$= \frac{2}{\mathfrak{N}} \sum_{\nu=0}^{\mathfrak{N}-1} \fint_{-\frac{\pi}{H}}^{\frac{\pi}{H}} \sum_{n=1}^{N_{\nu,\eta}} g_n(\nu,\eta) \sum_{J=1}^{N} \sum_{p=1}^{\mathcal{P}_J} \gamma_{J;p} \left| \int_{\hat{\Omega}} \widetilde{\chi}^*_{J;p}(\mathbf{x}, \hat{\mathbf{R}}_J, \mathcal{G}, \nu, \eta) \psi_n(\mathbf{x}, \nu, \eta) \, \mathrm{d}\mathbf{x} \right|^2 \mathrm{d}\eta \,, \tag{29}$$

where the symmetry-adapted nonlocal projector:

$$\widetilde{\chi}_{J;p}(\mathbf{x}, \hat{\mathbf{R}}_J, \mathcal{G}, \nu, \eta) = \sum_{\substack{\Gamma_{\zeta,\mu} \\ \hat{\mathbf{R}}_{J'} = \Gamma^{-1}_{\zeta,\mu} \circ \hat{\mathbf{R}}_J}} \chi_{J;p}(\Gamma_{\zeta,\mu} \circ \mathbf{x}, \hat{\mathbf{R}}_J) \, e^{-i(\nu(\tilde{\theta}_J - \tilde{\theta}_{J'}) + \eta(z_J - z_{J'}))} \,, \tag{30}$$

with $\Gamma^{-1}_{\zeta,\mu} = \Gamma_{\mathfrak{N}-\zeta,-\mu}$. In deriving Eq. 29, the third equality is obtained by using the identity that each atom and any of its images—atoms outside the fundamental domain that can be obtained by action of the group $\mathcal{G}$ on the atom of interest—have the same nonlocal pseudopotential energy (Appendix B), and the sixth equality is obtained using the symmetry in the Kohn-Sham orbitals (Eq. 20).

The symmetry-adapted electrostatic energy $\hat{E}_{el}$ takes the form:

$$\begin{aligned}
\hat{E}_{el}(\rho, \hat{\mathbf{R}}, \mathcal{G}) &= \frac{1}{|\mathcal{G}|} E_{el}(\rho, \mathbf{R}) \\
&= \frac{1}{|\mathcal{G}|} \sum_{\Gamma_{\zeta,\mu}} \left(-\frac{1}{8\pi} \int_{\Gamma_{\zeta,\mu} \circ \hat{\Omega}} \left| \nabla \phi(\mathbf{x}) \right|^2 \mathrm{d}\mathbf{x} + \int_{\Gamma_{\zeta,\mu} \circ \hat{\Omega}} \left(\rho(\mathbf{x}) + b(\mathbf{x}, \hat{\mathbf{R}}, \mathcal{G}) \right) \phi(\mathbf{x}) \, \mathrm{d}\mathbf{x} + \hat{E}_{sc}(\hat{\mathbf{R}}, \mathcal{G}) \right) \,, \\
&= -\frac{1}{8\pi} \int_{\hat{\Omega}} \left| \nabla \phi(\mathbf{x}) \right|^2 \mathrm{d}\mathbf{x} + \int_{\hat{\Omega}} \left(\rho(\mathbf{x}) + b(\mathbf{x}, \hat{\mathbf{R}}, \mathcal{G}) \right) \phi(\mathbf{x}) \, \mathrm{d}\mathbf{x} + \hat{E}_{sc}(\hat{\mathbf{R}}, \mathcal{G}) \,,
\end{aligned} \tag{31}$$

where $\hat{E}_{sc}$ is the self-correction energy per unit cell (Appendix A), and the last equality is obtained by using the symmetry in the electrostatic potential (Eq. 19) and the electron density (Eq. 22).

The symmetry-adapted electronic entropy energy $\hat{S}$ takes the form:

$$\begin{aligned}
\hat{S}(\hat{\mathbf{g}}) &= \frac{1}{|\mathcal{G}|} S(\mathbf{g}) \\
&= -\frac{2k_B T}{|\mathcal{G}|} \sum_{\nu=0}^{\mathfrak{N}-1} \sum_{\eta} \sum_{n=1}^{N_{\nu,\eta}} \Big(g_n(\nu,\eta) \log g_n(\nu,\eta) + (1 - g_n(\nu,\eta)) \log(1 - g_n(\nu,\eta)) \Big) \, \mathrm{d}\eta \\
&= -\frac{2k_B T}{\mathfrak{N}} \sum_{\nu=0}^{\mathfrak{N}-1} \fint_{-\frac{\pi}{H}}^{\frac{\pi}{H}} \sum_{n=1}^{N_{\nu,\eta}} \Big(g_n(\nu,\eta) \log g_n(\nu,\eta) + (1 - g_n(\nu,\eta)) \log(1 - g_n(\nu,\eta)) \Big) \, \mathrm{d}\eta \,.
\end{aligned} \tag{32}$$

The derivation of the symmetry-adapted energy functional and its final form have some key differences/advances from that proposed very recently[72]. First, the derivation here is for cyclic+helical symmetry, whereas only helical symmetry is considered previously. Second, the current derivation considers semilocal exchange-correlation functionals, whereas only local exchange-correlation functionals are considered previously. Third, rather than employing the density matrix, the derivation here is in terms of the orbitals and their occupations, which we believe provides more physical insights into the symmetry-adaption, since these are the quantities computed within a Kohn-Sham calculation. Fourth, we perform/derive symmetry-adaption for the electrostatic self-interaction and overlap correction term (Appendix A), which is found to be critical in obtaining the accurate energy[34,43]. Fifth, we do not restrict the derivation for the symmetry-adapted nonlocal pseudopotential energy to spherically symmetric projectors. Specifically, in previous work[72], as currently formulated, the action of symmetry operator in the projector function is transferred from the spatial coordinate to the atomic position, which is only applicable for spherically-symmetric projectors, i.e., chemical elements that only have s-orbital projectors. Indeed, this symmetry-adapted formalism can be generalized to non spherically-symmetric projectors using the strategy outlined here.

E. Symmetry-adapted Kohn-Sham problem

The symmetry-adapted constrained variational problem for the electronic ground state can now be written as:

$$\min_{\hat{\Psi}, \hat{\mathbf{g}}} \max_{\phi} \hat{\mathcal{F}}(\hat{\Psi}, \hat{\mathbf{g}}, \phi, \hat{\mathbf{R}}, \mathcal{G}) \quad \text{s.t.} \int_{\hat{\Omega}} \psi^*_m(\mathbf{x}, \nu, \eta) \psi_n(\mathbf{x}, \nu, \eta) \, \mathrm{d}\mathbf{x} = \delta_{mn} \, \forall \, m, n = 1, \ldots, N_{\nu,\eta}, \, \nu \in \{0, \ldots, \mathfrak{N}-1\}, \, \eta \in \left[-\frac{\pi}{H}, \frac{\pi}{H} \right] \,;$$

$$\text{and } \frac{2}{\mathfrak{N}}\sum_{\nu=0}^{\mathfrak{N}-1}\fint_{-\frac{\pi}{H}}^{\frac{\pi}{H}}\sum_{n=1}^{N_{\nu,\eta}} g_n(\nu,\eta)\,\mathrm{d}\eta = \hat{N}_e\,, \tag{33}$$

where $\hat{N}_e$ is the number of electrons in the fundamental domain. The corresponding Langrangian[74] can be defined as:

$$\begin{aligned}\hat{\mathcal{L}}(\hat{\Psi},\hat{\mathbf{g}},\phi,\hat{\mathbf{R}},\mathcal{G}) = \hat{\mathcal{F}}(\hat{\Psi},\hat{\mathbf{g}},\phi,\hat{\mathbf{R}},\mathcal{G}) - \frac{1}{\mathfrak{N}}\sum_{\nu=0}^{\mathfrak{N}-1}\fint_{-\frac{\pi}{H}}^{\frac{\pi}{H}}\sum_{i,j}\lambda_{ij}(\nu,\eta)\left(\int_{\hat{\Omega}}\psi_i^*(\mathbf{x},\nu,\eta)\psi_j(\mathbf{x},\nu,\eta)\,\mathrm{d}\mathbf{x}-\delta_{ij}\right)\mathrm{d}\eta \\ -\lambda_F\left(\frac{2}{\mathfrak{N}}\sum_{\nu=0}^{\mathfrak{N}-1}\fint_{-\frac{\pi}{H}}^{\frac{\pi}{H}}\sum_{n=1}^{N_{\nu,\eta}} g_n(\nu,\eta)\,\mathrm{d}\eta - \hat{N}_e\right)\,,\end{aligned} \tag{34}$$

where λ_{ij} and λ_F are the Lagrange multipliers used to enforce the constraint of orthonormality on the symmetry-adapted orbitals and the number of electrons in the fundamental domain, respectively.

The symmetry-adapted Kohn-Sham equations—obtained by taking variations of $\hat{\mathcal{L}}$ with respect to $\hat{\Psi}$ and $\hat{\mathbf{g}}$—on the fundamental domain $\hat{\Omega}$, with the prescribed boundary conditions on $\partial\hat{\Omega}$, take the form:

$$\begin{aligned}&\left[\mathcal{H}^{(\nu,\eta)} \equiv -\frac{1}{2}\nabla^2 + V_{xc} + \phi + V_{nl}^{(\nu,\eta)}\right]\psi_n(\mathbf{x},\nu,\eta) = \lambda_n(\nu,\eta)\,\psi_n(\mathbf{x},\nu,\eta)\,,\quad \nu\in\{0,\ldots,\mathfrak{N}-1\},\,\eta\in\left[-\frac{\pi}{H},\frac{\pi}{H}\right]\\ &\text{B.C.}\quad \psi_n(r\le R_1,\tilde{\theta},z,\nu,\eta) = \psi_n(r\ge R_2,\tilde{\theta},z,\nu,\eta) = 0\,,\\ &\qquad\quad \psi_n(r,\tilde{\theta}+\tilde{\Theta},z,\nu,\eta) = e^{i\nu\tilde{\Theta}}\psi_n(r,\tilde{\theta},z,\nu,\eta)\,,\\ &\qquad\quad \psi_n(r,\tilde{\theta},z+H,\nu,\eta) = e^{i\eta H}\psi_n(r,\tilde{\theta},z,\nu,\eta)\,;\end{aligned} \tag{35}$$

$$g_n(\nu,\eta) = \left(1+\exp\left(\frac{\lambda_n(\nu,\eta)-\lambda_F}{k_BT}\right)\right)^{-1},\quad \lambda_F \text{ is s.t. } \frac{2}{\mathfrak{N}}\sum_{\nu=0}^{\mathfrak{N}-1}\fint_{-\frac{\pi}{H}}^{\frac{\pi}{H}}\sum_{n=1}^{N_{\nu,\eta}} g_n(\nu,\eta)\,\mathrm{d}\eta = \hat{N}_e\,; \tag{36}$$

$$\begin{aligned}&-\frac{1}{4\pi}\nabla^2\phi(\mathbf{x},\hat{\mathbf{R}},\mathcal{G}) = \rho(\mathbf{x}) + b(\mathbf{x},\hat{\mathbf{R}},\mathcal{G})\,,\\ &\text{B.C.}\quad \phi(r\le R_1,\tilde{\theta},z,\hat{\mathbf{R}},\mathcal{G}) = \phi_1\,,\quad \phi(r\ge R_2,\tilde{\theta},z,\hat{\mathbf{R}},\mathcal{G}) = \phi_2\,,\\ &\qquad\quad \phi(r,\tilde{\theta}+\tilde{\Theta},z,\hat{\mathbf{R}},\mathcal{G}) = \phi(r,\tilde{\theta},z,\hat{\mathbf{R}},\mathcal{G})\,,\\ &\qquad\quad \phi(r,\tilde{\theta},z+H,\hat{\mathbf{R}},\mathcal{G}) = \phi(r,\tilde{\theta},z,\hat{\mathbf{R}},\mathcal{G})\,;\end{aligned} \tag{37}$$

where the exchange-correlation potential:

$$\begin{aligned}V_{xc}(\mathbf{x}) &= \frac{\delta\hat{E}_{xc}(\rho,\nabla\rho)}{\delta\rho}\\ &= \varepsilon_{xc}(\rho(\mathbf{x}),|\nabla\rho(\mathbf{x})|) + \rho(\mathbf{x})\frac{\partial\varepsilon_{xc}(\rho(\mathbf{x}),|\nabla\rho(\mathbf{x})|)}{\partial\rho(\mathbf{x})} - \nabla\cdot\left(\frac{\rho(\mathbf{x})}{|\nabla\rho(\mathbf{x})|}\frac{\partial\varepsilon_{xc}(\rho(\mathbf{x}),|\nabla\rho(\mathbf{x})|)}{\partial\left(|\nabla\rho(\mathbf{x})|\right)}\nabla\rho(\mathbf{x})\right)\,,\end{aligned} \tag{38}$$

and the symmetry-adapted nonlocal pseudopotential operator:

$$[V_{nl}^{(\nu,\eta)}f](\mathbf{x},\nu,\eta) = \sum_{J=1}^{N}\sum_{p=1}^{\mathcal{P}_J}\gamma_{J;p}\,\widetilde{\chi}_{J;p}(\mathbf{x},\hat{\mathbf{R}}_J,\mathcal{G},\nu,\eta)\int_{\hat{\Omega}}\widetilde{\chi}^*_{J;p}(\mathbf{y},\hat{\mathbf{R}}_J,\mathcal{G},\nu,\eta)f(\mathbf{y},\nu,\eta)\,\mathrm{d}\mathbf{y}\,. \tag{39}$$

The zero-Dirichlet boundary conditions for the orbitals in the r-direction are due to the exponential decay expected along any finite direction[78,79]—indeed, the values of R_1 and R_2 need to be chosen such that the radial boundaries are sufficiently far from the atoms—whereas in the $\tilde{\theta}$ and z-directions, they follow from the symmetry in the orbitals (Eqn. 20). The Dirichlet boundary conditions for the electrostatic potential in the r-direction account for the algebraic decay (if at all there is any decay) in that direction—the values of ϕ_1 and ϕ_2 can be determined through a Fourier-based analysis, as shown in Appendix C—whereas in the $\tilde{\theta}$ and z-directions, they follow from the symmetry in the electrostatic potential (Eqn. 19).

F. Symmetry-adapted atomic forces

The symmetry-adapted Hellmann-Feynman atomic force can be defined as:

$$\mathbf{f}_J(\hat{\mathbf{R}},\mathcal{G}) = -\frac{\partial\hat{\mathcal{L}}(\hat{\Psi},\hat{\mathbf{g}},\phi,\hat{\mathbf{R}},\mathcal{G})}{\partial\hat{\mathbf{R}}_J}\bigg|_{\mathbb{G}}, \tag{40}$$

where $\mathbf{f}_J$ denotes the force on the atom located at position $\hat{\mathbf{R}}_J$, and $\mathbb{G}$ denotes the electronic ground state. The total force $\mathbf{f}_J$ can be decomposed into the local ($\mathbf{f}_J^l$) and nonlocal ($\mathbf{f}_J^{nl}$) components, which arise from the electrostatic and nonlocal pseudopotential energy terms, respectively.

The symmetry-adapted local component of the force can be derived as:

$$\begin{aligned}
\mathbf{f}_J^l(\hat{\mathbf{R}},\mathcal{G}) &= -\int_{\hat{\Omega}} \frac{\partial b(\mathbf{x},\hat{\mathbf{R}},\mathcal{G})}{\partial\hat{\mathbf{R}}_J}\phi(\mathbf{x},\hat{\mathbf{R}},\mathcal{G})\,\mathrm{d}\mathbf{x} + \mathbf{f}_J^{sc}(\hat{\mathbf{R}},\mathcal{G}) \\
&= -\sum_{\Gamma_{\zeta,\mu}}\int_{\hat{\Omega}} \frac{\partial b_J(\mathbf{x},\Gamma_{\zeta,\mu}^{-1}\circ\hat{\mathbf{R}}_J)}{\partial\hat{\mathbf{R}}_J}\phi(\mathbf{x},\hat{\mathbf{R}},\mathcal{G})\,\mathrm{d}\mathbf{x} + \mathbf{f}_J^{sc}(\hat{\mathbf{R}},\mathcal{G}) \\
&= \sum_{\Gamma_{\zeta,\mu}}\mathfrak{R}_\varphi^\mu\mathfrak{R}_{\tilde{\Theta}}^\zeta\int_{\hat{\Omega}} \nabla b_J(\mathbf{x},\Gamma_{\zeta,\mu}^{-1}\circ\hat{\mathbf{R}}_J)\phi(\mathbf{x},\hat{\mathbf{R}},\mathcal{G})\,\mathrm{d}\mathbf{x} + \mathbf{f}_J^{sc}(\hat{\mathbf{R}},\mathcal{G}) \\
&= -\sum_{\Gamma_{\zeta,\mu}}\mathfrak{R}_\varphi^\mu\mathfrak{R}_{\tilde{\Theta}}^\zeta\int_{\hat{\Omega}} b_J(\mathbf{x},\Gamma_{\zeta,\mu}^{-1}\circ\hat{\mathbf{R}}_J)\nabla\phi(\mathbf{x},\hat{\mathbf{R}},\mathcal{G})\,\mathrm{d}\mathbf{x} + \mathbf{f}_J^{sc}(\hat{\mathbf{R}},\mathcal{G}),
\end{aligned} \tag{41}$$

where $\mathbf{f}_J^{sc}$ arises from the energy term $\hat{E}_{sc}$ (Appendix A), ∇ is the Cartesian gradient, the third equality is obtained using the spherical symmetry of b_J, and the fourth equality is obtained by using divergence theorem and integration by parts. The last step is motivated by the generally higher smoothness of ϕ relative to b_J and the increased efficiency for evaluation of forces on all atoms.

The symmetry-adapted nonlocal component of the force can be derived as:

$$\begin{aligned}
\mathbf{f}_J^{nl}(\hat{\mathbf{R}}_J,\mathcal{G}) &= -4\Bigg(\frac{1}{\mathfrak{N}}\sum_{\nu=0}^{\mathfrak{N}-1}\fint_{-\frac{\pi}{H}}^{\frac{\pi}{H}}\sum_{n=1}^{N_{\nu,\eta}} g_n(\nu,\eta)\sum_{p=1}^{\mathcal{P}_J}\gamma_{J;p}\mathrm{Re}\Bigg[\Bigg(\int_{\hat{\Omega}}\widetilde{\chi}_{J;p}(\mathbf{x},\hat{\mathbf{R}}_J,\mathcal{G},\nu,\eta)\psi_n^*(\mathbf{x},\nu,\eta)\,\mathrm{d}\mathbf{x}\Bigg) \\
&\times\Bigg(\int_{\hat{\Omega}}\frac{\partial\widetilde{\chi}_{J;p}^*(\mathbf{x},\hat{\mathbf{R}}_J,\mathcal{G},\nu,\eta)}{\partial\hat{\mathbf{R}}_J}\psi_n(\mathbf{x},\nu,\eta)\,\mathrm{d}\mathbf{x}\Bigg)\Bigg]\mathrm{d}\eta\Bigg) \\
&= -4\Bigg(\frac{1}{\mathfrak{N}}\sum_{\nu=0}^{\mathfrak{N}-1}\fint_{-\frac{\pi}{H}}^{\frac{\pi}{H}}\sum_{n=1}^{N_{\nu,\eta}} g_n(\nu,\eta)\sum_{p=1}^{\mathcal{P}_J}\gamma_{J;p}\mathrm{Re}\Bigg[\Bigg(\int_{\hat{\Omega}}\widetilde{\chi}_{J;p}(\mathbf{x},\hat{\mathbf{R}}_J,\mathcal{G},\nu,\eta)\psi_n^*(\mathbf{x},\nu,\eta)\,\mathrm{d}\mathbf{x}\Bigg) \\
&\times\Bigg(\sum_{\Gamma_{\zeta,\mu}}\int_{\hat{\Omega}}\frac{\partial\chi_{J;p}^*(\Gamma_{\zeta,\mu}\circ\mathbf{x},\hat{\mathbf{R}}_J)}{\partial\hat{\mathbf{R}}_J}e^{i(\nu\zeta\tilde{\Theta}+\eta\mu H)}\psi_n(\mathbf{x},\nu,\eta)\,\mathrm{d}\mathbf{x}\Bigg)\Bigg]\mathrm{d}\eta\Bigg) \\
&= -4\Bigg(\frac{1}{\mathfrak{N}}\sum_{\nu=0}^{\mathfrak{N}-1}\fint_{-\frac{\pi}{H}}^{\frac{\pi}{H}}\sum_{n=1}^{N_{\nu,\eta}} g_n(\nu,\eta)\sum_{p=1}^{\mathcal{P}_J}\gamma_{J;p}\mathrm{Re}\Bigg[\Bigg(\int_{\hat{\Omega}}\widetilde{\chi}_{J;p}(\mathbf{x},\hat{\mathbf{R}}_J,\mathcal{G},\nu,\eta)\psi_n^*(\mathbf{x},\nu,\eta)\,\mathrm{d}\mathbf{x}\Bigg) \\
&\times\Bigg(\sum_{\Gamma_{\zeta,\mu}}\mathfrak{R}_\varphi^\mu\mathfrak{R}_{\tilde{\Theta}}^\zeta\int_{\hat{\Omega}}\chi_{J;p}^*(\Gamma_{\zeta,\mu}\circ\mathbf{x},\hat{\mathbf{R}}_J)e^{i(\nu\zeta\tilde{\Theta}+\eta\mu H)}\nabla\psi_n(\mathbf{x},\nu,\eta)\,\mathrm{d}\mathbf{x}\Bigg)\Bigg]\mathrm{d}\eta\Bigg),
\end{aligned} \tag{42}$$

where the last equality is obtained by using the fact that the projector functions $\chi_{J;p}$ are defined with respect to the atomic positions, i.e., $\chi_{J;p}(\mathbf{x},\hat{\mathbf{R}}_J) = \chi_{J;p}(\mathbf{x}-\hat{\mathbf{R}}_J)$. This step is motivated by the higher smoothness of the orbitals relative to the projectors functions, which results in substantially more accurate atomic forces[34,43,80].

Therefore, the total symmetry-adapted atomic force along the Cartesian directions takes the form:

$$\mathbf{f}_J(\hat{\mathbf{R}},\mathcal{G}) = -\sum_{\Gamma_{\zeta,\mu}}\mathfrak{R}_\varphi^\mu\mathfrak{R}_{\tilde{\Theta}}^\zeta\int_{\hat{\Omega}} b_J(\mathbf{x},\Gamma_{\zeta,\mu}^{-1}\circ\hat{\mathbf{R}}_J)\nabla\phi(\mathbf{x},\hat{\mathbf{R}},\mathcal{G})\,\mathrm{d}\mathbf{x} + \mathbf{f}_J^{sc}(\hat{\mathbf{R}},\mathcal{G})$$

$$- 4\Bigg(\frac{1}{\mathfrak{N}}\sum_{\nu=0}^{\mathfrak{N}-1}\fint_{-\frac{\pi}{H}}^{\frac{\pi}{H}}\sum_{n=1}^{N_{\nu,\eta}} g_n(\nu,\eta)\sum_{p=1}^{\mathcal{P}_J}\gamma_{J;p}\mathrm{Re}\Bigg[\Bigg(\int_{\hat{\Omega}}\widetilde{\chi}_{J;p}(\mathbf{x},\hat{\mathbf{R}}_J,\mathcal{G},\nu,\eta)\psi_n^*(\mathbf{x},\nu,\eta)\,\mathrm{d}\mathbf{x}\Bigg)$$
$$\times\Bigg(\sum_{\Gamma_{\zeta,\mu}}\mathfrak{R}_{\varphi}^{\mu}\mathfrak{R}_{\tilde{\Theta}}^{\zeta}\int_{\hat{\Omega}}\chi_{J;p}^*(\Gamma_{\zeta,\mu}\circ\mathbf{x},\hat{\mathbf{R}}_J)e^{i(\nu\zeta\tilde{\Theta}+\eta\mu H)}\nabla\psi_n(\mathbf{x},\nu,\eta)\,\mathrm{d}\mathbf{x}\Bigg)\Bigg]\mathrm{d}\eta\Bigg). \tag{43}$$

Note that once the forces on the atoms in the fundamental domain have been determined, the forces on any image atom in the structure can be evaluated using the symmetry:

$$\mathbf{f}_{J'} = \mathfrak{R}_{\varphi}^{-\mu}\mathfrak{R}_{\tilde{\Theta}}^{\mathfrak{N}-\zeta}\mathbf{f}_J\,, \tag{44}$$

where $\mathbf{f}_{J'}$ is the force on the atom located at $\hat{\mathbf{R}}_{J'} = \Gamma_{\zeta,\mu}^{-1}\circ\hat{\mathbf{R}}_J$.

The symmetry-adapted force expression derived here has a number of key differences/advances from that proposed recently[72]. First, in the local component of the force, we have the gradient on the electrostatic potential, rather than the pseudocharge. This is desirable because it is not only more efficient, but also because the electrostatic potential is smoother than the pseudocharge, given the limited smoothness of the local part of the pseudopotential[81,82]. Second, we perform/derive symmetry-adaption for the component arising from the electrostatic self-interaction and overlap correction term (Appendix A), which is found to be critical in obtaining accurate forces[34,43]. Third, as discussed above, in the nonlocal component of the force, we have derivatives on the orbitals rather than the projectors, which provides substantially more accurate forces[34,43,80]. Fourth, as discussed previously, we do not assume that the nonlocal projectors are spherical in nature, therefore not placing any restrictions on the chemical elements that can be studied.

G. Symmetry-adapted axial stress

The symmetry-adapted Hellmann-Feynman stress along the axial direction (i.e., x_3-direction) can be defined as:

$$\sigma(\hat{\mathbf{R}},\mathcal{G}) = \frac{\mathfrak{N}}{H}\frac{\partial\hat{\mathcal{L}}^{\beta}(\hat{\Psi},\hat{\mathbf{g}},\phi,\hat{\mathbf{R}}^{\beta},\mathcal{G})}{\partial\beta}\Bigg|_{\beta=1,\mathbb{G}}\,, \tag{45}$$

where $\hat{\mathcal{L}}^{\beta}$ denotes the Lagrangian corresponding to an axial stretch by a factor β, with resultant atom positions denoted by $\hat{\mathbf{R}}^{\beta}$. The factor of $\mathfrak{N}$ in the above expression is needed to account for all the unit cells in the angular direction. Note that since the system is extended only along one direction, the stress has the units of force in the current context.

Proceeding along the lines of previous work[74], we arrive at the following expression for the symmetry-adapted axial stress:

$$\sigma(\hat{\mathbf{R}},\mathcal{G}) = \frac{\mathfrak{N}}{H}\Bigg[-\frac{2}{\mathfrak{N}}\sum_{\nu=0}^{\mathfrak{N}-1}\fint_{-\frac{\pi}{H}}^{\frac{\pi}{H}}\sum_{n=1}^{N_{\nu,\eta}} g_n(\nu,\eta)\int_{\hat{\Omega}}\left|\nabla_3\psi_n(\mathbf{x},\nu,\eta)\right|^2\mathrm{d}\mathbf{x}\,\mathrm{d}\eta + \hat{E}_{xc}(\rho,\nabla\rho) - \int_{\hat{\Omega}}V_{xc}(\rho(\mathbf{x}),\nabla\rho(\mathbf{x}))\rho(\mathbf{x})\,\mathrm{d}\mathbf{x}$$
$$- \int_{\hat{\Omega}}\frac{\rho(\mathbf{x})}{|\nabla\rho(\mathbf{x})|}\frac{\partial\varepsilon_{xc}(\rho(\mathbf{x}),|\nabla\rho(\mathbf{x})|)}{\partial\left(|\nabla\rho(\mathbf{x})|\right)}|\nabla_3\rho(\mathbf{x})|^2\,\mathrm{d}\mathbf{x} - \hat{E}_{nl}(\hat{\Psi},\hat{\mathbf{g}},\hat{\mathbf{R}},\mathcal{G})$$
$$- 4\Bigg(\frac{1}{\mathfrak{N}}\sum_{\nu=0}^{\mathfrak{N}-1}\fint_{-\frac{\pi}{H}}^{\frac{\pi}{H}}\sum_{n=1}^{N_{\nu,\eta}} g_n(\nu,\eta)\sum_{J=1}^{N}\sum_{p=1}^{\mathcal{P}_J}\gamma_{J;p}\mathrm{Re}\Bigg[\Bigg(\int_{\hat{\Omega}}\widetilde{\chi}_{J;p}(\mathbf{x},\hat{\mathbf{R}}_J,\mathcal{G},\nu,\eta)\psi_n^*(\mathbf{x},\nu,\eta)\,\mathrm{d}\mathbf{x}\Bigg)$$
$$\times\Bigg(\sum_{\Gamma_{\zeta,\mu}}\int_{\hat{\Omega}}\chi_{J;p}^*(\Gamma_{\zeta,\mu}\circ\mathbf{x},\hat{\mathbf{R}}_J)e^{i(\nu\zeta\tilde{\Theta}+\eta\mu H)}\left(x_3-z_{J'}\right)\nabla_3\psi_n(\mathbf{x},\nu,\eta)\,\mathrm{d}\mathbf{x}\Bigg)\Bigg]\mathrm{d}\eta\Bigg) + \frac{1}{4\pi}\int_{\hat{\Omega}}\left|\nabla_3\phi(\mathbf{x},\hat{\mathbf{R}},\mathcal{G})\right|^2\mathrm{d}\mathbf{x}$$
$$- \frac{1}{2}\sum_{J=1}^{N}\sum_{J'}\int_{\hat{\Omega}}\nabla_3 V_J(\mathbf{x},\hat{\mathbf{R}}_{J'})\left(x_3-z_{J'}\right)b_J(\mathbf{x},\hat{\mathbf{R}}_{J'})\,\mathrm{d}\mathbf{x} + \sum_{J=1}^{N}\sum_{J'}\int_{\hat{\Omega}}\nabla_3 b_J(\mathbf{x},\hat{\mathbf{R}}_{J'})(x_3-z_{J'})\Bigg(\phi(\mathbf{x},\hat{\mathbf{R}},\mathcal{G})$$
$$- \frac{1}{2}V_J(\mathbf{x},\hat{\mathbf{R}}_{J'})\Bigg)\mathrm{d}\mathbf{x} + \frac{1}{2}\int_{\hat{\Omega}}\Big(b(\mathbf{x},\hat{\mathbf{R}},\mathcal{G})-\rho(\mathbf{x})\Big)\phi(\mathbf{x},\hat{\mathbf{R}},\mathcal{G})\,\mathrm{d}\mathbf{x} - \frac{1}{2}\sum_{J=1}^{N}\sum_{J'}\int_{\hat{\Omega}}b_J(\mathbf{x},\hat{\mathbf{R}}_{J'})V_J(\mathbf{x},\hat{\mathbf{R}}_{J'})\,\mathrm{d}\mathbf{x} + \sigma^{\hat{E}_c}\Bigg], \tag{46}$$

where $\nabla_3 = \frac{\partial}{\partial x_3}$ denotes the partial derivative in the x_3 direction, J' index runs over the J^{th} atom and all its images in Ω, and $\sigma^{\hat{E}_c}$ is the stress contribution arising from the energy correction due to the overlapping pseudocharges[74]. Note that the current work is the first to derive the symmetry-adapted stress, the relaxation of which is important in physical applications, particularly in the context of large deformations.

H. Time-reversal symmetry

In the absence of magnetic fields, the cyclic+helical symmetry-adapted formulation presented above can be further reduced by employing time-reversal symmetry[7]. In particular, we have the following relations:

$$\lambda_n(\nu,\eta) = \lambda_n\left(\mathfrak{N}-\nu, \frac{2\pi s}{H}-\eta\right), \quad \psi_n(\mathbf{x},\nu,\eta) = \psi_n^*\left(\mathbf{x},\mathfrak{N}-\nu,\frac{2\pi s}{H}-\eta\right), \quad s\in\mathbb{Z}\,. \tag{47}$$

Consequently, the number of wavevectors (ν,η) in the first Brillouin zone that need to be considered for the Kohn-Sham equations as well as the calculation of the electron density, energy, atomic forces, and axial stress are reduced by a factor of two, approximately.

IV. REPRESENTATION OF TWISTED NANOTUBES IN CYCLIC+HELICAL DFT

In this section, we provide a representation for twisted nanotubes of arbitrary chirality—assumed to be constructed from 2D systems with honeycomb lattice structure—within the aforedescribed cyclic+helical DFT formalism. Specifically, adopting the helical-angular representation for the untwisted nanotube[83], we identify the fundamental domain parameters, location of the atoms within the fundamental domain, and the wavevectors (ν,η) in the first Brillouin zone. It is worth noting that the representation for such nanotubes in the cyclic+helical symmetry-adapted formalism is original to the current work. In addition to the above, we also find the connection between the Brillouin zone coordinates for the untwisted nanotube and corresponding 2D sheet, in the absence of curvature-induced effects. To the best of our knowledge, such a connection is also unique to the current work.

A. (n,m) nanotube

We first discuss the construction of a (n,m)-labeled untwisted nanotube from its flat sheet counterpart[84], as illustrated in Fig. 2. Consider a honeycomb lattice with lattice vectors chosen as:

$$\mathbf{a_1} = \frac{a}{2}\begin{bmatrix}\sqrt{3} & 1\end{bmatrix}^{\mathrm{T}}, \quad \mathbf{a_2} = \frac{a}{2}\begin{bmatrix}\sqrt{3} & -1\end{bmatrix}^{\mathrm{T}}, \tag{48}$$

where a is the length of these vectors. The (n,m) nanotube is constructed by rolling a strip of the infinite sheet into a seamless cylinder along the direction of the chiral vector:

$$\mathbf{C_h} = n\mathbf{a_1} + m\mathbf{a_2}\,, \quad |\mathbf{C_h}| = \pi d_t = a\sqrt{n^2+m^2+nm} \tag{49}$$

where $n,m\in\mathbb{Z}$ uniquely characterize the nanotube, whose diameter and circumference are denoted by d_t and $|\mathbf{C_h}|$, respectively. The chiral angle is then defined as:

$$\cos\omega = \frac{\mathbf{C_h}\cdot\mathbf{a_1}}{C_h\, a} = \frac{2n+m}{2\sqrt{n^2+m^2+nm}}\,, \quad 0\le\omega\le\frac{\pi}{6}\,, \tag{50}$$

where the bounds between $\omega=0$ (zigzag nanotube) and $\omega=\pi/6$ (armchair nanotube) account for the symmetry of the honeycomb lattice, i.e., any nanotube with chiral angle outside these bounds is equivalent to one within the bounds. In terms of the (n,m) notation, this translates to considering only nanotubes for which $n\ge m\ge 0$, with $(n,0)$ and (n,n) representing zigzag and armchair variants, respectively. Zigzag and armchair nanotubes are referred to as achiral nanotubes, whereas all others are collectively referred to as chiral nanotubes.

The periodicity of the nanotube is determined by a vector perpendicular to the chiral vector $\mathbf{C_h}$, referred to as the translation vector:

$$\mathbf{T} = t_1\mathbf{a_1} + t_2\mathbf{a_2}\,, \quad t_1,t_2\in\mathbb{Z}\,, \quad \gcd(t_1,t_2)=1\,, \tag{51}$$

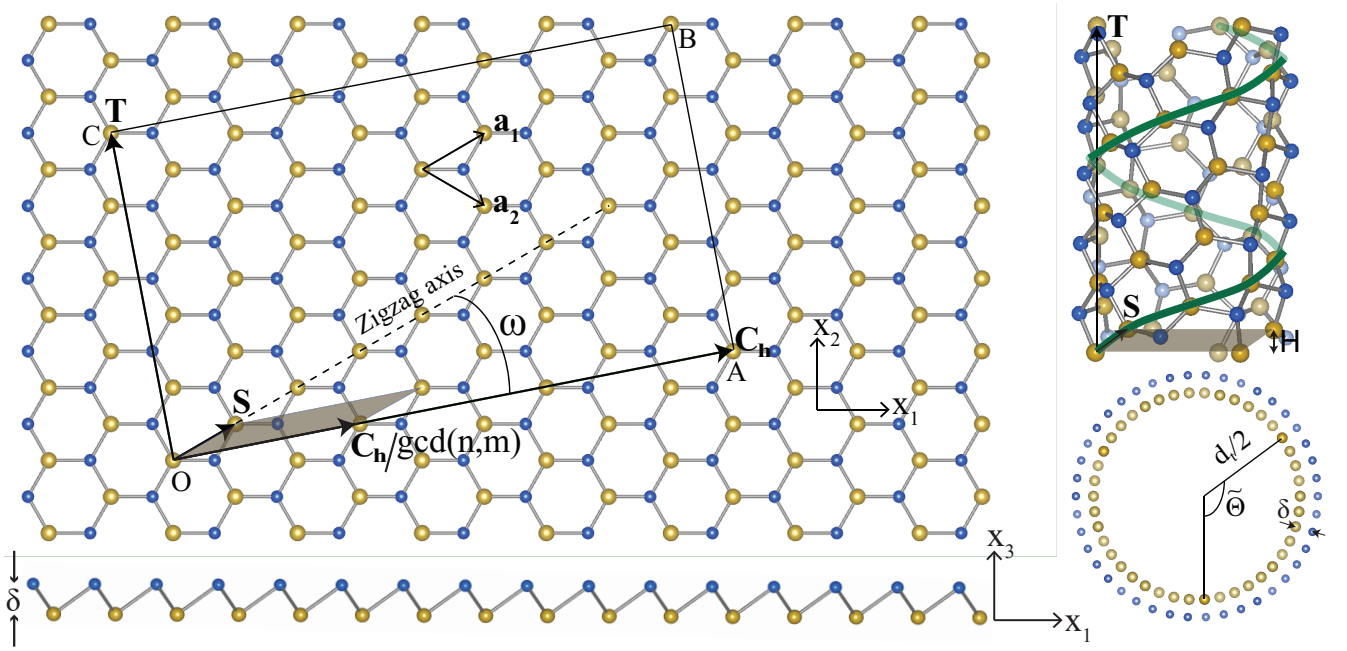

FIG. 2: Illustration depicting the construction of a (n, m) nanotube from a 2D honeycomb lattice, and identification of the nanotube's fundamental domain and atoms. The lattice vectors for the flat sheet are denoted by $\mathbf{a_1}$ and $\mathbf{a_2}$, with the out-of-plane displacement represented by δ. The chiral vector along which the sheet is rolled is denoted by $\mathbf{C_h}$, whose angle ω with the zigzag axis is referred to as the chiral angle. The nanotube's axially periodic unit cell that has been unrolled onto the plane is shown by the rectangle OABC, where $\mathbf{T}$ is the translational vector. The corresponding fundamental domain, which is described by the screw displacement vector $\mathbf{S}$ and the vector $\mathbf{C_h}/\gcd(n, m)$, is shaded grey. The front view and top view of the constructed nanotube of diameter d_t are also shown, where H is the height of the fundamental domain, $\tilde{\Theta}$ is the angle subtended by the fundamental domain at the nanotube center, and the green helix connects the helical images of an atom in the fundamental domain.

where gcd is used to denote the greatest common divisor, and the coefficients:

$$t_1 = (2m + n)/d_R\,, \quad t_2 = -(2n + m)/d_R\,, \quad \text{with} \quad d_R = \gcd(2m + n, 2n + m)\,. \tag{52}$$

The length of the translational vector is:

$$|\mathbf{T}| = \frac{\sqrt{3}|\mathbf{C_h}|}{d_R}\,. \tag{53}$$

B. Fundamental domain and atoms

We now identify the fundamental domain parameters and the location of the fundamental domain atoms for the twisted (n, m) nanotube within the cyclic+helical symmetry-adapted formalism, as illustrated in Fig. 2. Consider the untwisted nanotube's axially periodic unit cell that has been unrolled onto the plane, defined by the vectors $\mathbf{C_h}$ and $\mathbf{T}$. This unit cell has additional symmetry that can be exploited to define the (irreducible) fundamental domain. There are three such possibilities, among which we choose the one defined by the helical-angular construction[83], due to its compatibility with the cyclic+helical symmetry.

The fundamental domain based on the helical-angular construction of the nanotube is a parallelogram with one side as the vector $\frac{1}{\mathfrak{N}}\mathbf{C_h}$, where $\mathfrak{N} = \gcd(n, m)$ is the cyclic group order of the nanotube. The other side, denoted by $\mathbf{S}$—the flat sheet equivalent of the screw displacement vector describing the chirality of the nanotube, can be decomposed as:

$$\mathbf{S} = c_1\mathbf{C_h} + c_2\mathbf{T} = p\mathbf{a_1} + q\mathbf{a_2}\,, \quad c_1, c_2 \in (0, 1); \quad p, q \in \mathbb{Z}\,, \tag{54}$$

where the coefficients

$$c_1 = \frac{\mathbf{S}\cdot\mathbf{C_h}}{|\mathbf{C_h}|^2} = \frac{(p\mathbf{a_1} + q\mathbf{a_2})\cdot(n\mathbf{a_1} + m\mathbf{a_2})}{|\mathbf{C_h}|^2} = \frac{(2n + m)p + (2m + n)q}{N_c d_R}\,, \tag{55}$$

$$c_2 = \frac{\mathbf{S}\cdot\mathbf{T}}{|\mathbf{T}|^2} = \frac{(p\mathbf{a_1}+q\mathbf{a_2})\cdot(t_1\mathbf{a_1}+t_2\mathbf{a_2})}{|\mathbf{T}|^2} = \frac{pm-qn}{N_c}\,, \tag{56}$$

with $N_c = 2(n^2+m^2+nm)/d_R$ representing the number of hexagons in the periodic unit cell. Since the area per atom in the fundamental domain as well the periodic unit cell should be the same[84], we arrive at the relation:

$$\frac{|\mathbf{C_h}|}{\mathfrak{N}}c_2|\mathbf{T}| = \frac{\sqrt{3}a^2}{2} \implies c_2 = \frac{\sqrt{3}a^2\mathfrak{N}}{2|\mathbf{C_h}||\mathbf{T}|} = \frac{\mathfrak{N}}{N_c}\,. \tag{57}$$

Thereafter, it follows from Eqs. 56 and 57 that:

$$pm - qn = \mathfrak{N}\,, \tag{58}$$

using which the coefficient c_1 can be written as the following minimization problem:

$$c_1 = \min_{q\in\mathbb{Z}}\left(\frac{\frac{(2n+m)\mathfrak{N}}{md_R}+\frac{qN_c}{m}}{N_c}\right) \quad \text{s.t.} \quad \frac{\mathfrak{N}+qn}{m}\in\mathbb{Z}\,, 0<c_1<1\,. \tag{59}$$

Therefore, the parameters describing the untwisted nanotube's fundamental domain $\hat{\Omega}$ in the cyclic+helical symmetry-adapted formalism (Eq. 24) are obtained as:

$$\tilde{\Theta} = \frac{2}{d_t}\left(\frac{|\mathbf{C_h}|}{\mathfrak{N}}\right) = \frac{2\pi}{\mathfrak{N}}\,, \quad H = \mathbf{S}.\left(\frac{\mathbf{T}}{|\mathbf{T}|}\right) = \frac{\mathfrak{N}|\mathbf{T}|}{N_c}\,, \quad \alpha = \frac{1}{H}\left(\frac{2}{d_t}\right)\mathbf{S}.\left(\frac{\mathbf{C_h}}{|\mathbf{C_h}|}\right) = \frac{2\pi c_1}{H}\,, \tag{60}$$

where α represents the chirality of the tube. The values for the inner radius R_1 and the outer radius R_2 of $\hat{\Omega}$ are chosen so as to allow for sufficient decay of the orbitals. If an external twist of α_a is applied on the nanotube, the twist parameter takes the form:

$$\alpha = \frac{2\pi c_1}{H} + \alpha_a\,. \tag{61}$$

with all fundamental domain parameters remaining the same. Therefore, the cyclic+helical symmetry-adapted framework allows for the handling of both chirality and applied twist through the twist parameter. Indeed, the above strategy of adding the applied twist to the chirality is not restricted to nanotubes alone, but is generally applicable to 1D nanostructures subject to torsional deformations.

The locations of the atoms within the fundamental domain of the nanotube are identified as follows. Consider the J^{th} ($J\in\{1,2,\ldots,N\}$) atom in the fundamental domain of the honeycomb lattice located at $q_1^J\mathbf{a_1}+q_2^J\mathbf{a_2}+\delta_J\hat{\mathbf{e}}_\mathbf{3}$, where δ_J is the out-of-plane displacement of the atom. The corresponding atom's location within the fundamental domain of the unrolled nanotube configuration can be written as $p_1^J\mathbf{C_h}+p_2^J\mathbf{T}+\delta_J\hat{\mathbf{e}}_\mathbf{3}$, where p_1^J and p_2^J are uniquely determined by l_1, $l_2\in\mathbb{Z}$ that satisfy the relations:

$$0 \leq \left[p_1^J := \frac{\big((l_1+q_1^J)\mathbf{a_1}+(l_2+q_2^J)\mathbf{a_2}\big)\cdot\mathbf{C_h}}{|\mathbf{C_h}|^2}\right] < \frac{1}{\mathfrak{N}}\,, \tag{62}$$

$$0 \leq \left[p_2^J := \frac{\big((l_1+q_1^J)\mathbf{a_1}+(l_2+q_2^J)\mathbf{a_2}\big)\cdot\mathbf{T}}{|\mathbf{T}|^2}\right] < \frac{\mathfrak{N}}{N_c}\,. \tag{63}$$

It follows that the coordinates of the atom in helical coordinates within the fundamental domain of the nanotube are:

$$r_J = d_t/2+\delta_J\,, \quad \tilde{\theta}_J = 2\pi p_1^J - \alpha p_2^J|\mathbf{T}|, \quad z_J = p_2^J|\mathbf{T}|\,. \tag{64}$$

The above representation provides tremendous simplification in both the computational cost and interpretation of results, by significantly reducing the number of atoms in the fundamental domain, particularly in the case of torsional deformations and/or chiral tubes. Even for untwisted achiral tubes, the representation provides simplification with respect to the recent cyclic symmetry-adapted method[71], by reducing the number of atoms in the fundamental domain by a factor of two. It is also worth noting that the though the above framework is restricted to nanotubes generated from honeycomb lattices, which is the focus of this work, it can be easily extended to other 2D lattices with chiralities that permit the existence of translational symmetry in the direction perpendicular to the chiral vector.

C. Brillouin zone

In the cyclic+helical symmetry-adapted DFT formalism, the first Brillouin zone of the (n,m)-nanotube takes the form:

$$(\nu,\eta) : \nu \in \{0,\ldots,\mathfrak{N}-1\},\, \eta \in \left[-\frac{\pi}{H},\frac{\pi}{H}\right], \tag{65}$$

$$\mathfrak{N} = \gcd(n,m), H = \frac{\mathfrak{N}|\mathbf{T}|}{N_c}, \tag{66}$$

as illustrated in Fig. 3. In the absence of magnetic fields, time reversal symmetry can be used to reduce the Brillouin zone to approximately half its size, as described in Section III H. In certain circumstances, it is of interest to know the connection between the Brillouin zone coordinates for the nanotube and the corresponding 2D honeycomb lattice structure, since it has the potential to provide fundamental insight into the behavior of the nanotube. For example, identifying whether the location of the Dirac cones in graphene's Brillouin zone exist in the nanotube's Brillouin zone (discrete in the variable ν), can be used to argue whether the nanotube is expected to be metallic or an insulator[84]. In these cases, it also helps identify important wavevectors at which the band structure should be calculated.

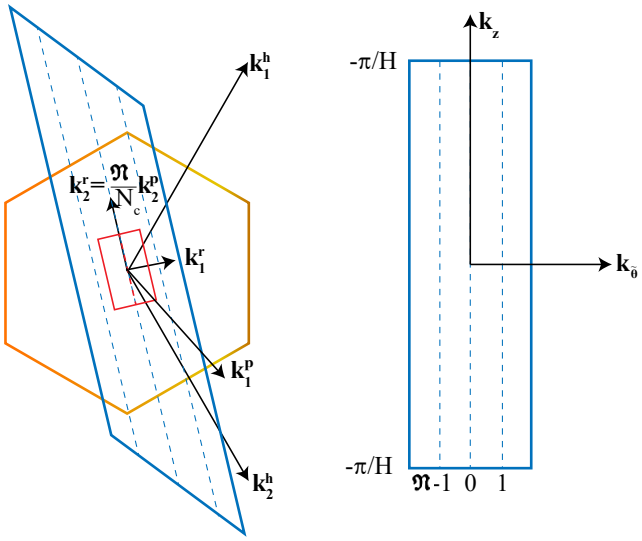

FIG. 3: The first Brillouin zones corresponding to the (i) honeycomb lattice (left, orange), with reciprocal lattice vectors $\mathbf{k_1^h}$ and $\mathbf{k_2^h}$; (ii) nanotube's axially periodic cell unrolled onto the plane (left, red), with reciprocal lattice vectors $\mathbf{k_1^r}$ and $\mathbf{k_2^r}$; (iii) fundamental domain of the nanotube's axially periodic cell unrolled onto the plane (left, blue), with reciprocal lattice vectors $\mathbf{k_1^p}$ and $\mathbf{k_2^p}$; and (iv) the nanotube in the helical coordinate system (right), with reciprocal lattice vectors $\mathbf{k_z}$ and $\mathbf{k_{\tilde{\theta}}}$. The dashed lines are used to indicate the discrete nature of the Brillouin zone, with the space between any two such lines indicating non-existent parts of the Brillouin zone.

In view of the above, we now identify the connection between the untwisted Brillouin zone coordinates of the (n,m) nanotube and the corresponding honeycomb lattice. Let $[c_1^h\ c_2^h]^{\mathrm{T}}$ denote the fractional coordinates of the point of interest in the Brillouin zone of the flat sheet with basis vectors $\mathbf{a_1}$ and $\mathbf{a}_2$. It follows that

$$\begin{bmatrix}\nu\\ \eta\end{bmatrix} = \left(\mathbf{M_s}\mathbf{M_r}^{-1}\mathbf{M_h}\right)\begin{bmatrix}c_1^h\\ c_2^h\end{bmatrix} \tag{67}$$

where the transformation matrices:

$$\mathbf{M_s} = \begin{pmatrix}\frac{|\mathbf{C_h}|}{2\pi} & 0\\ \frac{c_1 N_c|\mathbf{C_h}|}{\mathfrak{N}|\mathbf{T}|} & 1\end{pmatrix}, \mathbf{M_r} = \frac{a}{2|\mathbf{C_h}|}\begin{pmatrix}\sqrt{3}(n+m) & m-n\\ n-m & \sqrt{3}(n+m)\end{pmatrix}, \mathbf{M_h} = \frac{2\pi}{a}\begin{pmatrix}\frac{1}{\sqrt{3}} & \frac{1}{\sqrt{3}}\\ 1 & -1\end{pmatrix}. \tag{68}$$

Note that in cases when $\begin{bmatrix}\nu\\ \eta\end{bmatrix}$ is obtained outside the first Brillouin zone, it needs to be mapped back to within it. In obtaining the above, we have used the fact that $\mathbf{M_h}\begin{bmatrix}c_1^h\\ c_2^h\end{bmatrix}$ transforms $\begin{bmatrix}c_1^h\\ c_2^h\end{bmatrix}$ to absolute coordinates in the

standard Cartesian coordinate system, then the application of $\mathbf{M_r}^{-1}$ transforms the result to a rotated Cartesian coordinate system that is aligned with the Brillouin zone of the unrolled nanotube's axially periodic unit cell, and then the application of $\mathbf{M_s}$ transforms the result to the wavevector $\begin{bmatrix}\nu\\ \eta\end{bmatrix}$ in the Brillouin zone of the nanotube. In certain circumstances, it might be advantageous to know the corresponding coordinates in the Brillouin zone of the fundamental domain of the flat sheet:

$$\begin{bmatrix}c_1^p\\ c_2^p\end{bmatrix} = \left(\mathbf{M_p}^{-1}\mathbf{M_h}\right)\begin{bmatrix}c_1^h\\ c_2^h\end{bmatrix}, \tag{69}$$

where the transformation matrix

$$\mathbf{M_p} = \frac{a}{2|\mathbf{C_h}|}\begin{pmatrix} \frac{\sqrt{3}(n+m)\mathfrak{N} - \frac{c_1 N_c d_R (m-n)}{\sqrt{3}}}{\sqrt{\mathfrak{N}^2 + \frac{c_1^2 N_c^2 {d_R}^2}{3}}} & m-n \\ \frac{\mathfrak{N}(n-m) - c_1 N_c d_R (n+m)}{\sqrt{\mathfrak{N}^2 + \frac{c_1^2 N_c^2 {d_R}^2}{3}}} & \sqrt{3}(n+m) \end{pmatrix}. \tag{70}$$

Note that the columns of the matrices $\mathbf{M_r}$ and $\mathbf{M_p}$ are nothing but the corresponding reciprocal space unit vectors, and the columns of $\mathbf{M_h}$ are the corresponding reciprocal lattice vectors, all of which are illustrated in Fig. 3.

In going from the honeycomb lattice to the lattice generated by the unrolled cylinder, one of the directions with infinite translational periodicity becomes finite, resulting in the Brillouin zone of the nanotube corresponding to the cyclic symmetry (i.e., ν component of the wavevector) being discrete. Therefore, not all $\begin{bmatrix}c_1^h\\ c_2^h\end{bmatrix}$ have a corresponding $\begin{bmatrix}\nu\\ \eta\end{bmatrix}$, with the condition for existence of the mapping being:

$$nc_1^h + mc_2^h \in \mathbb{Z}\,. \tag{71}$$

Such a condition has practical utility in predicting the physical behavior of the nanotubes, e.g., the Dirac point in graphene at $\begin{bmatrix}c_1^h\\ c_2^h\end{bmatrix} = \begin{bmatrix}2/3\\ 1/3\end{bmatrix}$ only gets mapped to the Brillouin zone of the nanotube for $\frac{2n+m}{3} \in \mathbb{Z}$, which is the generally accepted condition for carbon nanotubes to be metallic[84]. Note that the above analysis neglects curvature-induced effects, which in some cases does shift the location of the point within the nanotube's Brillouin zone.

V. NUMERICAL IMPLEMENTATION

In this section, we describe the implementation of the aforedescribed cyclic+helical symmetry-adapted formulation within the massively parallel real-space DFT code SPARC[8]. The developed implementation, which will be henceforth referred to as Cyclix-DFT, is capable of performing spin-polarized and unpolarized calculations, in both the static and dynamic setting, for both local and semilocal exchange-correlation functionals.

A. Helical coordinate system

We work in the $(r,\, \tilde{\theta},\, z)$ helical coordinate system (Eq. 23), in which the fundamental domain $\hat{\Omega}$ takes a cuboidal form (Eq. 24). The Laplacian operator in these coordinates can easily be derived from the Laplacian in cylindrical polar coordinates as:

$$\nabla^2 \equiv \frac{\partial^2}{\partial r^2} + \frac{1}{r}\frac{\partial}{\partial r} + \left(\frac{1}{r^2} + \alpha^2\right)\frac{\partial^2}{\partial \tilde{\theta}^2} + \frac{\partial^2}{\partial z^2} - 2\alpha\frac{\partial^2}{\partial \tilde{\theta}\partial z}\,, \tag{72}$$

and the Cartesian gradient operator, when expressed in terms of derivatives with respect to helical coordinate variables, takes the form:

$$\nabla \equiv \left(\cos(\tilde{\theta}+\alpha z)\frac{\partial}{\partial r} - \frac{\sin(\tilde{\theta}+\alpha z)}{r}\frac{\partial}{\partial \tilde{\theta}}\right)\hat{\mathbf{e}}_{x_1} + \left(\sin(\tilde{\theta}+\alpha z)\frac{\partial}{\partial r} + \frac{\cos(\tilde{\theta}+\alpha z)}{r}\frac{\partial}{\partial \tilde{\theta}}\right)\hat{\mathbf{e}}_{x_2} + \left(-\alpha\frac{\partial}{\partial \tilde{\theta}} + \frac{\partial}{\partial z}\right)\hat{\mathbf{e}}_{x_3}\,, \tag{73}$$

where $\hat{\mathbf{e}}_{x_1}$, $\hat{\mathbf{e}}_{x_2}$, and $\hat{\mathbf{e}}_{x_3}$ are the Cartesian unit vectors.

B. Real-space discretization

A uniform real-space grid in helical coordinates is used to discretize the fundamental domain $\hat{\Omega}$, which translates to a non-uniform curvilinear grid in Cartesian coordinates that is compatible with the symmetry of the system. Each grid point is indexed using the triplet (i,j,k), where $i = 0,1,\ldots,n_r$, $j = 0,1,\ldots,n_{\tilde{\theta}}-1$, and $k = 0,1,\ldots,n_z-1$, with n_r+1, $n_{\tilde{\theta}}$, and n_z representing the number of nodes in the r, $\tilde{\theta}$, and z directions, respectively. The coordinates of any arbitrary node (i,j,k) are therefore given by $(R_1+ih_r, jh_{\tilde{\theta}}, kh_z)$, where $h_r = \left(\frac{R_2-R_1}{n_r}\right)$, $h_{\tilde{\theta}} = \frac{\tilde{\Theta}}{n_{\tilde{\theta}}}$, and $h_z = \frac{H}{n_z}$ are the spacing in the r, $\tilde{\theta}$, and z directions, respectively. Though there is no restriction on the choice of spacing, it is generally appropriate to employ similar distances between grid points in the different coordinate directions, i.e., $h := h_r \sim \frac{R_2+R_1}{2}h_{\tilde{\theta}} \sim \sqrt{1+\frac{(R_1+R_2)^2}{4}\alpha^2}h_z$, where h will henceforth be referred to as the mesh size.

We use centered finite-differences to approximate derivatives arising in the Laplacian and gradient operators:

$$\begin{aligned}
\nabla^2 f\big|^{(i,j,k)} \approx & \sum_{p=0}^{n_o} w_{p,r}\left(f^{(i+p,j,k)} + f^{(i-p,j,k)}\right) + \frac{1}{r^{(i,j,k)}}\sum_{p=1}^{n_o}\tilde{w}_{p,r}\left(f^{(i+p,j,k)} - f^{(i-p,j,k)}\right) + \sum_{p=0}^{n_o} w_{p,\tilde{\theta}}\left(f^{(i,j+p,k)} + f^{(i,j-p,k)}\right) \\
& + \sum_{p=0}^{n_o} w_{p,z}\left(f^{(i,j,k+p)} + f^{(i,j,k-p)}\right) - 2\alpha\sum_{p=1}^{n_o}\tilde{w}_{p,\tilde{\theta}}\left(\frac{\partial f}{\partial z}\Big|^{(i,j+p,k)} - \frac{\partial f}{\partial z}\Big|^{(i,j-p,k)}\right) \qquad (74) \\
\nabla f\big|^{(i,j,k)} \approx & \Bigg(\cos(\tilde{\theta}^{(i,j,k)}+\alpha z^{(i,j,k)})\sum_{p=1}^{n_o}\tilde{w}_{p,r}\left(f^{(i+p,j,k)} - f^{(i-p,j,k)}\right) \\
& - \frac{\sin(\tilde{\theta}^{(i,j,k)}+\alpha z^{(i,j,k)})}{r^{(i,j,k)}}\sum_{p=1}^{n_o}\tilde{w}_{p,\tilde{\theta}}\left(f^{(i,j+p,k)} - f^{(i,j-p,k)}\right)\Bigg)\hat{\mathbf{e}}_{x_1} \\
& + \Bigg(\sin(\tilde{\theta}^{(i,j,k)}+\alpha z^{(i,j,k)})\sum_{p=1}^{n_o}\tilde{w}_{p,r}\left(f^{(i+p,j,k)} - f^{(i-p,j,k)}\right) \\
& + \frac{\cos(\tilde{\theta}^{(i,j,k)}+\alpha z^{(i,j,k)})}{r^{(i,j,k)}}\sum_{p=1}^{n_o}\tilde{w}_{p,\tilde{\theta}}\left(f^{(i,j+p,k)} - f^{(i,j-p,k)}\right)\Bigg)\hat{\mathbf{e}}_{x_2} \\
& + \Bigg(-\alpha\sum_{p=1}^{n_o}\tilde{w}_{p,\tilde{\theta}}\left(f^{(i,j+p,k)} - f^{(i,j-p,k)}\right) + \sum_{p=1}^{n_o}\tilde{w}_{p,z}\left(f^{(i,j,k+p)} - f^{(i,j,k-p)}\right)\Bigg)\hat{\mathbf{e}}_{x_3}\,, \qquad (75)
\end{aligned}$$

where the superscript $(.)^{(i,j,k)}$ denotes the value of the quantity at the node (i,j,k), f is any arbitrary function, n_o is half the order of the finite-difference, and the weights for $s \in \{r,\tilde{\theta},z\}$ can be written as[85,86]:

$$\begin{aligned}
\tilde{w}_{p,s} &= \frac{(-1)^{p+1}}{h_s p}\frac{(n_o!)^2}{(n_o-p)!(n_o+p)!}\,,\ p = 1,2,\ldots,n_o\,, \\
w_{0,s} &= -\frac{1}{h_s^2}\sum_{q=1}^{n_o}\frac{1}{q^2}\,, \qquad (76) \\
w_{p,s} &= \frac{2\tilde{w}_{p,s}}{h_s p}\,,\ p = 1,2,\ldots,n_o\,.
\end{aligned}$$

Note that as written in Eq. 74, the mixed derivative term in the Laplacian is evaluated in $\mathcal{O}(n_o)$ fashion by the sequential application of the associated first-order derivatives[87]. Also note that the discrete Laplacian and therefore the Hamiltonian are non-Hermitian in the current setting, even though the continuous operators from which they arise are Hermitian. We have found that this artifact of the finite-difference discretization does not impact the results, in agreement with previous work that also employ curvilinear coordinates within the real-space method[71,88].

We approximate integrals over the fundamental domain $\hat{\Omega}$ using the following quadrature rule:

$$\begin{aligned}
\int_{\hat{\Omega}} f(\mathbf{x})\,\mathrm{d}\mathbf{x} &\approx \sum_{i=0}^{n_r}\sum_{j=0}^{n_{\tilde{\theta}}-1}\sum_{k=0}^{n_z-1} f^{(i,j,k)}\left|\frac{\partial(x_1,x_2,x_3)}{\partial(r,\tilde{\theta},z)}\right| h_r h_{\tilde{\theta}} h_z \\
&= h_r h_{\tilde{\theta}} h_z \sum_{i=0}^{n_r}\sum_{j=0}^{n_{\tilde{\theta}}-1}\sum_{k=0}^{n_z-1}(R_1+ih_r) f^{(i,j,k)}\,, \qquad (77)
\end{aligned}$$

where $\left|\frac{\partial(x_1,x_2,x_3)}{\partial(r,\tilde{\theta},z)}\right|$ denotes the Jacobian of the transformation between Cartesian and helical coordinates.

C. Brillouin zone sampling

The Brillouin zone variables η and ν correspond to the helical and cyclic symmetry, respectively. Integrals over η are approximated using a Monkhorst-Pack[89] type trapezoidal quadrature rule:

$$\fint_{-\frac{\pi}{H}}^{\frac{\pi}{H}} f(\eta)\,\mathrm{d}\eta \approx \sum_{b=1}^{N_\eta} w_{\eta_b} f(\eta_b)\,, \tag{78}$$

where N_η denotes the number of nodes in the grid (i.e., number of η-points), with η_b and w_{η_b} denoting their locations and weights, respectively. Though the Brilluoin zone corresponding to the cyclic group symmetry is inherently discrete, it can become very dense for the systems with large cyclic group order. In such cases, given the expected smoothness of the quantities over the variable ν, the following approximation can be employed:

$$\frac{1}{\mathfrak{N}}\sum_{\nu=0}^{\mathfrak{N}-1} f(\nu) \approx \sum_{b=1}^{N_\nu} w_{\nu_b} f(\nu_b)\,, \tag{79}$$

where $\nu_b \in \mathcal{V} \subset \{0,1,\cdots,\mathfrak{N}-1\}$ are the nodes, w_{ν_b} are the quadrature weights, and N_ν is the cardinality of the set $\mathcal{V}$, i.e., number of ν-points. Note that though this approximation has not been employed in the current work since the nanotubes studied here have relatively small cyclic group order, its efficacy has been verified for nanotubes with large cyclic group order. Also note that time reversal symmetry is used to reduce the total number of Brillouin zone sampling points by a factor of ~ 2, as discussed in Section III H.

D. Electronic ground state

The electronic ground state is calculated using a fixed-point iteration with respect to the density/potential, referred to as the self-consistent field (SCF) method.[7] The superposition of the isolated-atom electron densities is used as an initial guess for the SCF iteration, which is accelerated using the restarted variant[90] of the Periodic Pulay mixing scheme[91] in conjunction with a real-space preconditioner[92]. The pseudocharges are placed on the grid by applying the discrete Laplacian on the local part of the pseudopotential[86]. In each SCF iteration, a partial diagonalization of the linear eigenproblem is performed using the CheFSI method[93,94], with multiple Chebyshev filtering steps performed in the first iteration of the simulation[95]; and the linear system corresponding to the Poisson problem solved using the Alternating Anderson-Richardson (AAR) iterative method[96,97], with Laplacian-vector products performed in matrix-free fashion and the Dirichlet boundary conditions imposed by introducing a compensating charge density[43]. Within the CheFSI method, we employ the Lanczos method for determining the Chebyshev bounds, Brent's method[98] for calculation of the Fermi level, and LAPACK[99] routines for solving the subspace eigenproblem. The Hamiltonian-vector products are performed in a matrix-free fashion, using the finite-difference stencil for the Laplacian and the outer product nature of the nonlocal pseudopotential operator. Again, boundary conditions on the orbitals are imposed for the Laplacian during application of the stencil. The ground-state energy is calculated using the symmetry-adapted energy functional in Eq. 26, which is efficiently implemented via a correction[9] to the Harris-Foulkes functional[100,101].

The Generalized Gradient Approximation (GGA) exchange-correlation has a dependence on $\nabla\rho(\mathbf{x})$, which is not commensurate with the underlying symmetry. In particular, it satisfies the relation: $\Gamma_{\zeta,\mu} \circ (\nabla\rho(\mathbf{x})) = \mathfrak{R}^{\zeta}_{\tilde{\Theta}} \mathfrak{R}^{\mu}_{\varphi}(\nabla\rho(\mathbf{x}))$, which is employed during implementation. If instead, the standard definition of the gradient is employed, highly inaccurate results can be obtained, particularly for the force, which can then manifest itself in all ground state quantities/properties. For example, consider GeS and GeSe nanotubes of diameters $d_t = 7.28$ and 7.22 nm, respectively, obtained by rolling the corresponding atomic monolayers[102,103]. Upon rolling, on using the standard and symmetry-adapted transformations for the real-space gradient, the error in the force with respect to well-converged SPARC calculations is $\sim 1\times10^{-2}$ and $\sim 5\times10^{-5}$ Ha/Bohr, respectively. This shows that more than two orders of magnitude inaccuracy in the force can result from the use of the incorrect transformation for the gradient. In terms of the bending modulus for 2D materials — computed from the ground state energy of nanotubes with different radii[102] — the values for GeS and GeSe obtained using the standard definition of the gradient are 4.37 and 4.45 eV, respectively, which are more then three times the values reported[102] when the correct transformation for the gradient is used.

E. Structural relaxation and QMD

Cyclix-DFT can perform simultaneous atom and cell relaxation to determine the structural ground state. The code is equipped with a variety of atomic relaxation algorithms, including non-linear conjugate gradient[104], LBFGS[105], and FIRE[106], with charge density extrapolated from previous atomic configurations to accelerate SCF convergence[107]. While performing atomic relaxation, to avoid inconsistencies with the search directions, positions and forces on the atoms that were originally in the fundamental domain are used in the relaxation algorithms, with Eq. 44 used to calculate the forces on atoms that may have moved out during the simulation. For cell relaxation, we use Brent's method to calculate the equilibrium length of the unit cell in the axial direction.

Cyclix DFT can also perform symmetry-adapted quantum molecular dynamics (QMD) simulations to study the dynamics of systems with cyclic+helical symmetry. Similar to structural relaxation, charge extrapolation is used to accelerate the SCF convergence in future QMD steps, and forces on the atoms that were originally in the fundamental domain are used for the dynamical evolution, with Eq. 44 again used to calculate the forces on atoms that may have moved out during the simulation. Note that in both structural relaxation and QMD, the symmetry of the system with respect to the unit cell is maintained throughout the simulation. Also note that, though not demonstrated in this work, Cyclix-DFT is capable of performing non-equilibrium molecular dynamics, wherein the applied twist is varied during the QMD simulation[108].

F. Parallelization

Cyclix-DFT employs multiple levels of parallelization that varies between different parts of the code to maximize parallel scalability. Specifically, the charge densities and effective potential—sum of the exchange-correlation potential and the electrostatic potential obtained via the solution of the Poisson equation—are computed using a Cartesian topology of processors that is formed by embedding a three-dimensional processor grid into the MPI COMM WORLD communicator. The CheFSI algorithm employs a DFT-specific eigensolver topology that is created by first splitting the MPI COMM WORLD communicator into multiple spin groups, then splitting each spin group into multiple Brillouin zone sampling groups, then splitting each Brillouin zone sampling group into multiple band groups, and finally, embedding each band group with a Cartesian topology. Therefore, the total number of processors employed in the eigensolver topology are split as:

$$N_p = N_p^{\texttt{Spin}} \times N_p^{\texttt{BZ}} \times N_p^{\texttt{Band}} \times N_p^{\texttt{Domain}} \tag{80}$$

where $N_p^{\texttt{Spin}}$, $N_p^{\texttt{BZ}}$, $N_p^{\texttt{Band}}$, and $N_p^{\texttt{Domain}}$ are the number of spin, Brillouin zone integration, band, and domain communicators (groups), respectively.

VI. ACCURACY AND PERFORMANCE

In this section, we study the accuracy and performance of the Cyclix-DFT code using the chiral $(18, 9)$ single-walled carbon nanotube (CNT) as the representative example. In all calculations, we choose a two-atom unit cell, twelfth-order accurate finite-difference discretization, Local Density Approximation (LDA)[2] of the exchange-correlation functional with the Perdew-Wang parametrization[109] of the correlation energy as calculated by Ceperley and Alder[110], Fermi-Dirac smearing of $k_BT = 0.001$ Ha, and the Optimized Norm Conserving Vanderbilt (ONCV) pseudopotential[81].

A. Accuracy and convergence

We start by verifying the convergence of the computed energy, atomic forces, and axial stress with respect to Brillouin zone integration, vacuum in the radial direction, and spatial discretization. In order to have numerically significant values for the forces and stress, the unit cell is perturbed from its equilibrium configuration along the axial direction. First, we verify convergence with respect to Brillouin zone integration, i.e., value of N_η, while choosing the mesh size and vacuum to be $h = 0.2$ Bohr and 10 Bohr, respectively. It is clear from the results in Fig. 4a that there is a systematic convergence in all quantities to reference values obtained at $N_\eta = 300$. Next, we verify convergence with vacuum, while choosing $h = 0.2$ Bohr and $N_\eta = 30$. We observe from the results presented in Fig. 4b that there is exponential convergence in all quantities to reference values obtained at a vacuum of 12 Bohr. Finally, we verify convergence with respect to mesh size, while employing $N_\eta = 30$ and a vacuum of 10 Bohr. It is clear from the results

in Fig. 4c that there is a systematic convergence in all quantities to reference values obtained at $h = 0.1$ Bohr. On performing a linear fit to this data, we find convergence rates of approximately $\mathcal{O}(9)$, $\mathcal{O}(11)$, and $\mathcal{O}(9)$ in the energy, forces, and stress, respectively, similar to those obtained by SPARC for affine coordinate systems[34,74,87]. These results verify the effectiveness of the real-space formulation for non-uniform curvilinear grids arising in the helical coordinate system, with previous such studies generally restricted to uniform Cartesian grids[34,74,87].

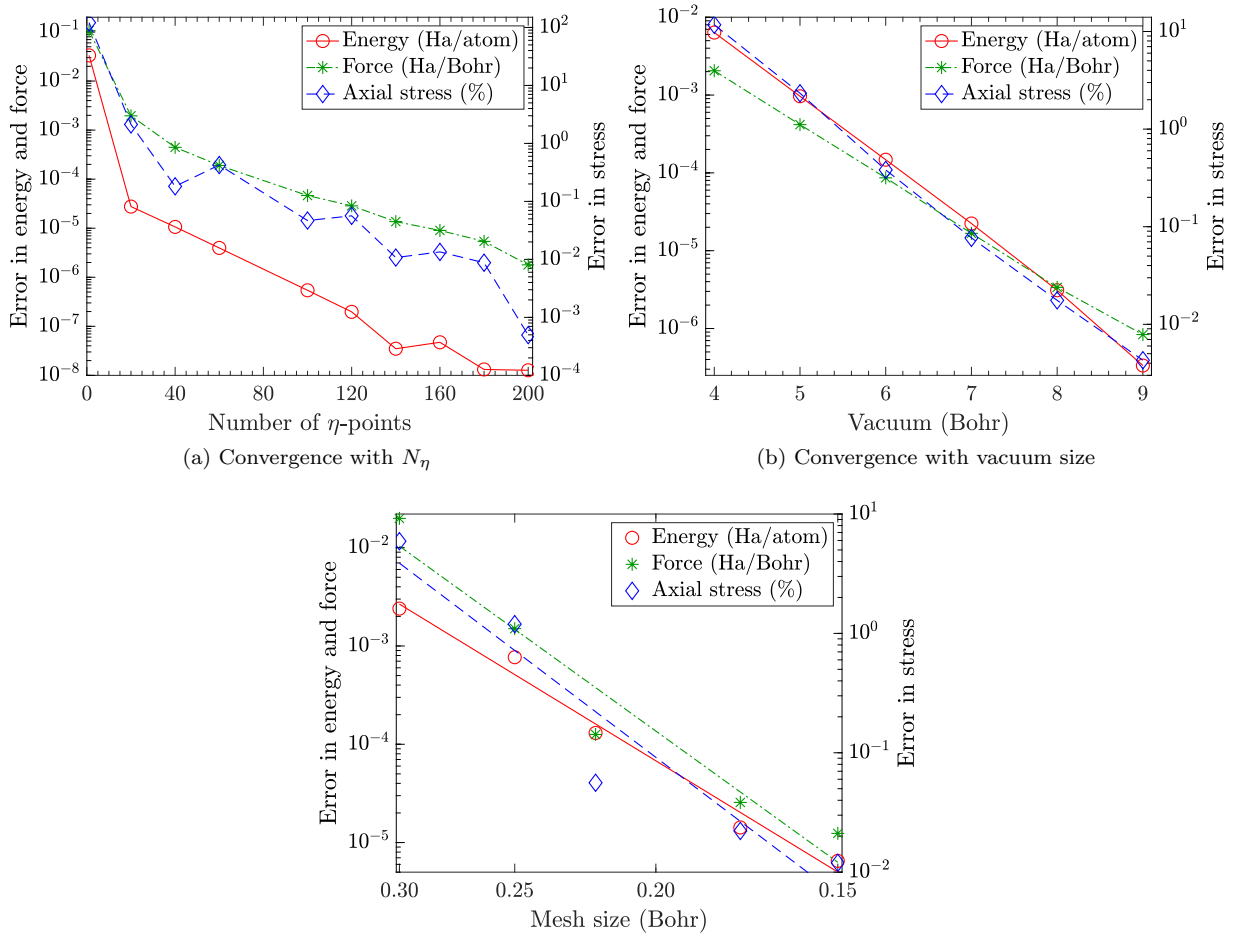

(a) Convergence with N_η

(b) Convergence with vacuum size

(c) Convergence with spatial discretization

FIG. 4: Convergence of energy, atomic forces, and axial stress with respect to number of η-points, vacuum size in the radial direction, and mesh size for the $(18, 9)$ CNT. The error in the energy, forces, and stress are defined to be the magnitude of the difference, maximum difference in any component, and percentage difference, respectively.

The energy, atomic forces, and axial stress computed by Cyclix-DFT are in very good agreement with those computed by the real-space DFT code SPARC[8,34,43] and the planewave code ABINIT[111]. For instance, on choosing $h = 0.2$ Bohr, $N_\eta = 49$, and a vacuum of 10 Bohr in Cyclix-DFT, the agreement with well-converged SPARC results is 4×10^{-5} Ha/atom, 4×10^{-4} Ha/Bohr, and 0.3% in the energy, forces, and stress, respectively. The corresponding agreement with well-converged ABINIT results is 3×10^{-5} Ha/atom, 4×10^{-4} Ha/Bohr, and 0.3%, respectively. The agreement is equally good for the choice of the semilocal PBE[112] GGA exchange-correlation functional, e.g. on choosing $h = 0.175$ Bohr, $N_\eta = 49$, and a vacuum of 10 Bohr in Cyclix-DFT, the agreement with well-converged SPARC results is 3×10^{-6} Ha/atom, 5×10^{-4} Ha/Bohr, and 0.5% in the energy, forces and stress, respectively. The corresponding agreement with well-converged ABINIT results is 5×10^{-5} Ha/atom, 4×10^{-4} Ha/Bohr, and 0.5%, respectively. The agreement between Cyclix-DFT and SPARC/ABINIT gets even better on further increasing the accuracy of computations in each code. Note that the accuracy of Cyclix-DFT has been verified against SPARC/ABINIT for many other nanotubes (e.g. transition metal dichalcogenides), details of which have been omitted here for the sake of brevity. To verify the applicability and accuracy of Cyclix-DFT for other types of systems, we perform a similar test for a carbon nanocoil in Appendix E.

B. Structural relaxation

Next, we study the capability of Cyclix-DFT in performing symmetry-adapted structural relaxations by verifying the consistency of the computed energy, atomic forces, and axial stress. Specifically, we evaluate the numerical derivative of the energy with respect to the atomic perturbations and compare it with the computed forces, and also evaluate the numerical derivative of the energy with respect to the perturbations in unit cell length along the axial direction and compare it with the computed stress. The results so obtained are presented in Fig. 5, from which it is clear that there is very good agreement between the numerical derivatives of the energy and the computed forces/stress, with negligible eggbox effect[113] — phenomenon arising due to the spatial discretization breaking the underlying symmetry of the system. In particular, the energy minima with respect to atomic positions and unit cell length are in good agreement with the zero force and stress configurations, respectively, verifying the capability of Cyclix-DFT to perform symmetry-adapted structural relaxations. Note that though this work focuses on static calculations, Cyclix-DFT is also capable of performing quantum molecular dynamics (QMD) simulations, as demonstrated in Appendix D. Also note that the current work is the first to perform such consistency studies when working in curvilinear coordinates.

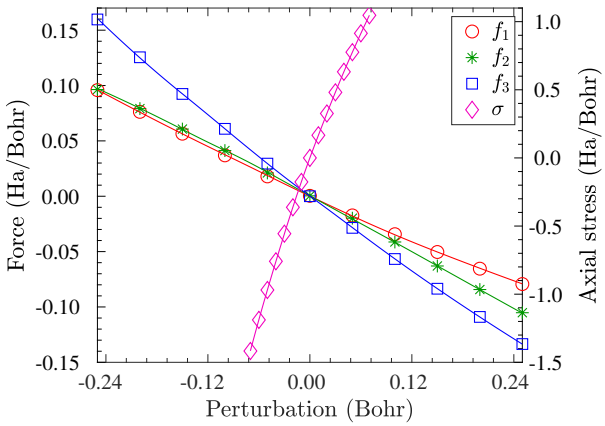

FIG. 5: Consistency of the computed energy, atomic forces, and axial stress in Cyclix-DFT for the $(18, 9)$ CNT. The markers represent the computed forces (f_1, f_2, and f_3) and stress (σ), whereas the corresponding curves represent the derivatives of the cublic spline fit to the energy with respect to the atomic position and perturbations in the axial unit cell length, respectively .

C. Scaling and performance

We finally study the parallel scaling and performance of Cyclix-DFT to demonstrate the range and type of systems/simulations that are accessible to Cyclix-DFT, as well as the gains relative to state-of-the-art DFT codes. Rather than perform a weak scaling test with respect to the number of atoms, as is typically the norm, we perform it with respect to the number of points sampled in the Brillouin zone. This is because the scaling with the number of fundamental domain atoms—quadratic for small to moderate-sized systems, while approaching cubic for larger system sizes[34,43]—is expected to be very similar to the underlying SPARC code, and is therefore not repeated here for the sake of brevity. Additionally, the number of Brillouin zone points sampled in the cyclic+helical symmetry-adapted DFT formalism is generally indicative of the size and complexity of the system being studied.

The scaling tests are performed using a mesh size of $h = 0.2$ Bohr, $N_\nu = 9$, and a vacuum of 7 Bohr, values that are representative of practical simulations. For the strong scaling test, we choose $N_\eta = 60$, while increasing the number of processors from 1 to 1080, whereas for the weak scaling test, we increase the value of N_η from 2 to 2500, while proportionally increasing the number of processors between 3 and 3750. In Fig. 6, we present the wall time per SCF iteration so obtained, with $\mathcal{O}(6-8)$ iterations required to determine the electronic ground state, the exact number determined by the SCF tolerance. It is clear from Fig. 6 that Cyclix-DFT demonstrates excellent strong scaling, with 50% efficiency even on increasing the number of processors by three orders of magnitude. In addition, Cyclix-DFT demonstrates excellent weak scaling, with 80% efficiency even on increasing the number of Brillouin zone points by three orders of magnitude. The deviation from the ideal scaling, which increases with the number of processors, can be attributed to the time associated with global parallel communications.

The theoretical estimate for increase in efficiency within Cyclix-DFT after cyclic+helical symmetry-adaption is at least a factor of $\mathcal{O}\left(\frac{|\Omega|}{|\hat{\Omega}|}\right)$, with larger factors appearing as the system size increases, a consequence of different parts of

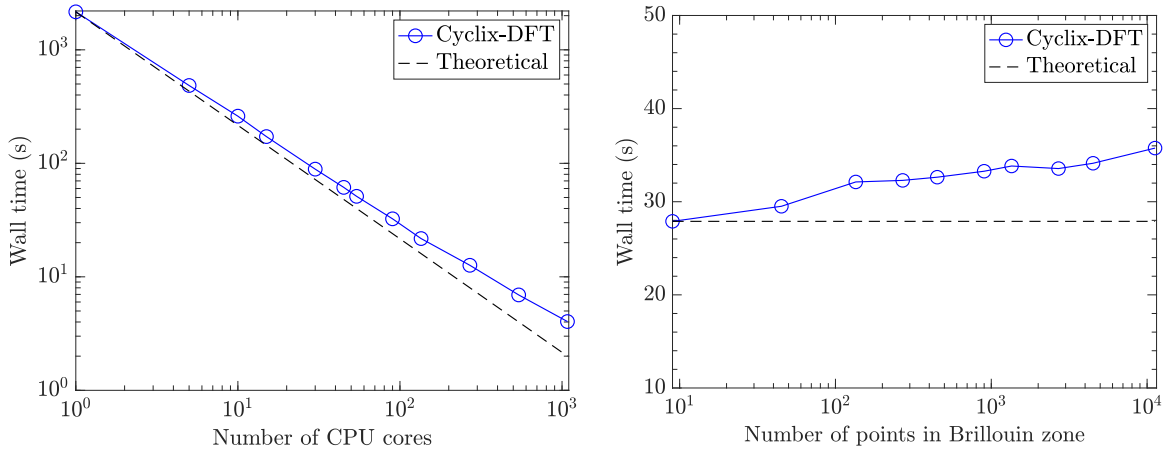

(a) Strong scaling (b) Weak scaling

FIG. 6: Parallel scaling of a single SCF iteration in Cyclix-DFT for the $(18, 9)$ CNT, with the dashed line representing the ideal scaling. The number of points in Brillouin zone correspond to those obtained after time-reversal symmetry.

the DFT implementation having different scaling with system size and that too with significantly different prefactors. Here, $|\Omega|$ and $|\hat{\Omega}|$ denote the volume of the original and fundamental domains, respectively. For the $(18, 9)$ nanotube studied here, this translates to a $\mathcal{O}(126)$ speedup within Cyclix-DFT, which is actually manifested in computations. In terms of its comparison with SPARC, which itself outperforms established state-of-the-art DFT codes by more than an order of magnitude, Cyclix-DFT is faster by factor of $\mathcal{O}(13)$ in terms of CPU time. The aforementioned theoretical estimate does not directly translate between the two codes, a consequence of a number of factors, including the following: the lesser vacuum in Cyclix-DFT due to the domain being an annular region; the larger number of states employed in Cyclix-DFT, since precise values for the number of occupied states at each wavevector $N_{\nu,\eta}$ are not known apriori; the fewer number of SCF iterations required in Cyclix-DFT, since charge sloshing effects are reduced; the larger number of operations involved in the Laplacian-vector/matrix products for Cyclix-DFT, a consequence of the cylindrical nature of the coordinate system; and the finer mesh in the z-direction required by Cyclix-DFT as the twist parameter α increases, which in combination with the cylindrical nature of the coordinate system, results in the requirement of a larger degree for the Chebyshev polynomial within the CheFSI eigensolver. Indeed, as the inner radius of the annular region increases, the theoretical estimate is readily achieved, with an additional $\mathcal{O}\left(\frac{\mathfrak{N}}{N_\nu}\right)$ speedup possible by using Brillouin zone sampling for ν (Eq. 79), making Cyclix-DFT ideally suited for the study of large-diameter 1D hollow nanostructures. It is worth noting that in the presence of practically relevant applied twists, the speedups achieved by Cyclix-DFT relative to standard codes are expected to be many orders of magnitude and more, given the tremendously large unit cells required for prescribing translational symmetry.

As suggested by the results in Fig. 6, Cyclix-DFT can solve the symmetry-adapted Kohn-Sham problem in $\mathcal{O}(1)$ minute on $\mathcal{O}(100 - 1000)$ processors, resources that are commonly available to researchers. In terms of time to solution, this represents a $\mathcal{O}(100 - 1000)$ factor speedup over the recently developed symmetry-adapted Matlab implementation[72]. In particular, employing the same numerical parameters as in previous work[72], i.e., mesh size $h = 0.4$ Bohr, $N_\eta = 11$, and $\alpha = 0.001$ rad/Bohr, Cyclix-DFT performs force relaxation for a phosphorene nanotube of diameter $d_t = 1.7$ nm in 62 seconds on 360 processors, while the Matlab implementation takes a few hours[72], indicating a $\mathcal{O}(100 - 1000)$ speedup. Indeed, the exact speedup is dependent on the system of interest and number of processors available.

VII. TORSIONAL DEFORMATION OF CARBON NANOTUBES

In this section, we use Cyclix-DFT to study the mechanical and electronic response of carbon nanotubes (CNTs) to torsional deformations. Specifically, we perform twist-controlled numerical experiments for the following representative set of CNTs: $(16, 0)$, $(20, 0)$, and $(27, 0)$ zigzag nanotubes of type I, type II, and type III, respectively,[71] with diameters $d_t = 1.25$, 1.56, and 2.10 nm, respectively; $(18, 9)$ and $(22, 11)$ chiral nanotubes with $d_t = 1.85$ and 2.26 nm, respectively; and $(13, 13)$ armchair nanotube with $d_t = 1.75$ nm. In particular, we choose 2-atom unit cells described by the formalism presented in Section IV, and determine the ground state for the applied twist, while maintaining the

total twist per unit cell (i.e., αH) constant during cell relaxation. We initially restrict the values of the applied twist to the small deformation regime where CNTs are expected to be stable[54,62,114] (Sections VII A and VII B), before studying their response in the large deformation regime (Section VII C). Note that such calculations are beyond the reach of standard DFT methods. Therefore, to the best of our knowledge, the results presented here are the first to be obtained via ab initio methods, and are therefore likely to be quantitatively more accurate than previous efforts that employ lower levels of theory.

In all calculations, we employ the LDA exchange-correlation functional,[2,109,110] which provides an accurate representation of the mechanical and electronic response for CNTs[115]. In addition, we employ the ONCV pseudopotential[81], whose transferability in the current context has been verified through comparisons[11] with all-electron calculations[116] for the equilibrium structure of graphene, the flat sheet analogue of CNTs. Also, we perform spin-unpolarized calculations, having verified that spin does not have any impact on the results. For the numerical parameters, we choose mesh size of $h = 0.2$ Bohr, vacuum size of 10 Bohr in the radial direction, the number of η-points for Brillouin zone integration $N_\eta = 70$, Fermi-Dirac smearing of $k_B T = 0.001$ Ha, atomic relaxation tolerance on the force of 5×10^{-4} Ha/Bohr, and cell relaxation tolerance on the stress of 1×10^{-5} Ha/Bohr. Given the availability of resources and the relatively large number of wavevectors that need to be considered, the simulations are mainly parallelized over Brillouin zone sampling, i.e., $N_p = N_p^{\mathtt{BZ}}$.

A. Strain energy: Torsional modulus

The strain energy density $\mathcal{E}_{twist}$ associated with torsional deformations can be defined as the increase in the ground state energy of the system upon applying the external twist α_a, divided by the length of the unit cell in the axial direction, i.e., H. The corresponding torsional modulus K_{twist} can then be defined as:

$$K_{\text{twist}}(\alpha_a) = \frac{\partial^2 \mathcal{E}_{twist}}{\partial \alpha_a^2}\,, \tag{81}$$

where the dependence on α_a is used to signify that the behavior might be nonlinear. We study the mechanical response of the chosen CNTs by considering twists in the regime $0 \leq \alpha_a \leq 0.04$ rad/nm, commensurate with those found in experiments[114]. We find that the nanotubes demonstrate linear response, i.e., strain energy has a quadratic dependence on the external twist, as shown by results in the inset of Fig. 7. Therefore, the torsional modulus for each nanotube is constant for the twists considered, whereby its value can be interpreted as that corresponding to the asymptotic zero-twist limit. We evaluate this value of K_{twist} for each of the CNTs using a curve fit to the data, the variation of which with respect to their diameter d_t is presented in Fig. 7. In particular, we find that:

$$K_{\text{twist}} \sim C d_t^3\,, \quad C = 0.733156 \ \text{keV/nm}^2 \tag{82}$$

indicating that the torsional moduli vary cubically with the diameter of the nanotubes, as predicted by continuum mechanics. This suggests that the moduli of CNTs are independent of their chirality, a result in agreement with previous atomistic calculations[54]. Indeed, the above equation can be used to estimate the torsional modulus of any CNT from first principles, making it valuable in this regard. It can also be used to predict the shear modulus, a quantity of interest for higher scale theories such as continuum mechanics. In particular, we obtain a value of 0.44 TPa, which is in good agreement with experimental measurements (0.41 TPa[117]) as well as tight binding calculations (0.46[61]). The significant difference from atomistic calculations[54] of 0.25 TPa is likely due to the inaccuracy of the chosen empirical potential. Note that in calculating the shear modulus, the thickness of CNTs needs to be assumed, which has been chosen to be the same[117] for all shear moduli values discussed here.

B. Bandgap and effective mass

We now study the electronic response of the CNTs to torsional deformations. Specifically, we determine the variation in bandgap and effective mass of the charge carriers, i.e., electrons and holes, for external twists in the regime $0 \leq \alpha_a \leq 0.04$ rad/nm. In the current context, the bandgap E_g is defined to be the difference between the lowest unoccupied and highest occupied orbitals, when all wavevectors (ν, η) in the Brillouin zone are considered. In practice, this is achieved by computing the band structure at the ground state on a dense set of η-points, chosen in the vicinity of the η-point that correlates with the Dirac cone in graphene's Brillouin zone, determined using the procedure outlined in Section IV C. The effective mass of charge carriers in the cyclic+helical symmetry-adapted

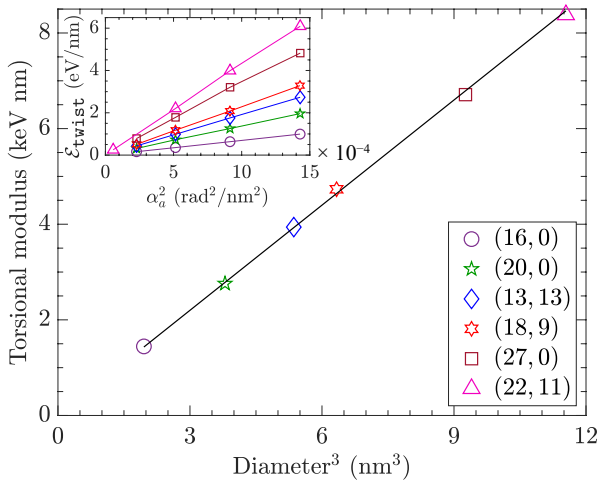

FIG. 7: Variation of torsional modulus K_{twist} with the cube of the diameter d_t^3 for the CNTs. The straight line represents the linear fit to the data. The inset shows the variation of strain energy $\mathcal{E}_{twist}$ with respect to square of the applied twist α_a^2.

formulation takes the form:

$$m^* = \hbar^2 \left(\frac{\partial^2 \lambda_n(\nu,\eta)}{\partial \eta^2} \right)^{-1} \Bigg|_{(\nu,\eta)=(\nu^*,\eta^*)} , \tag{83}$$

where $\hbar$ is the reduced Planck's constant, n is an index that corresponds to the highest occupied orbital for holes and lowest unoccupied orbital for electrons, $\lambda_n(\nu,\eta)$ is the eigenvalue of the symmetry-adapted Hamiltonian $\mathcal{H}^{(\nu,\eta)}$, and (ν^*,η^*) corresponds to the location of the bandgap. The effective mass relates to the electrical transport properties of semiconducting materials, as it is inversely proportional to the mobility of the charge carriers, which in turn influences the diffusivity of the charge carriers and the electrical conductivity of the material.

In Fig. 8a, we plot the variation in bandgap E_g with shear strain:

$$\gamma = \frac{1}{2}\alpha d_t \,, \tag{84}$$

from which the following observations can be made. First, in the absence of torsional deformations, the $(13,13)$, $(27,0)$, and $(18,9)$ nanotubes are metallic, whereas the $(16,0)$, $(20,0)$, and $(22,11)$ nanotubes are insulating, which is in agreement with the well established criterion for predicting whether a nanotube is metallic or an insulator, i.e., a (n,m) CNT is metallic if $n-m$ is a multiple of 3, else it is an insulator.[84] Second, all bandgaps are direct, while following the following law for the difference in bandgap from the untwisted configuration:

$$\Delta E_g \sim 3t_0\gamma \sin(3\omega) \,, \quad t_0 = 3.14 \text{ eV} \,, \tag{85}$$

where t_0 can be interpreted as the hopping parameter, and ω is the chiral angle of the nanotube. This relationship is in good agreement with that predicted using the Hückel tight-binding model[118] as well as experimental measurements[114], where the hopping parameters are determined to be 2.66 and 2.70 eV, respectively. Third and finally, we notice that zigzag CNTs are inert to small torsional deformations, which is also in agreement with literature[118].

In Fig. 8b, we plot the variation in effective mass m^* of charge carriers with shear strain γ. Note that a common plot is used for both charge carriers, since we have found that the effective mass of electrons and holes is nearly identical. It is clear from the results that the variation in the effective mass with twist for the chosen CNTs follows a similar trend as the corresponding bandgap. Therefore, we can arrive at the following law for the difference in the effective mass from the untwisted configuration:

$$\Delta m^* = \pm \tilde{C}\gamma \sin(3\omega) \,, \quad \tilde{C} = 1.28 \; m_e \,, \tag{86}$$

where m_e is the electron's mass and $\pm$ signs correspond to electrons and holes, respectively. Though the variation of effective mass with uniaxial deformations of CNTs has been studied before[119], to the best of our knowledge, the corresponding study for torsional deformations has not been performed heretofore. Note that the effective mass of the charge carriers for untwisted zigzag type I and II nanotubes are in good agreement with previous work[120]. Also note

that the effective mass is not well defined for the metallic CNTs due to the linear nature of the dispersion relationship. However, the first derivative can be used to calculate the Fermi velocity, for which we obtain $\sim 8.3 \times 10^5$ m/s, a result that is in good agreement with the experimental value of 8.1×10^5 m/s[121].

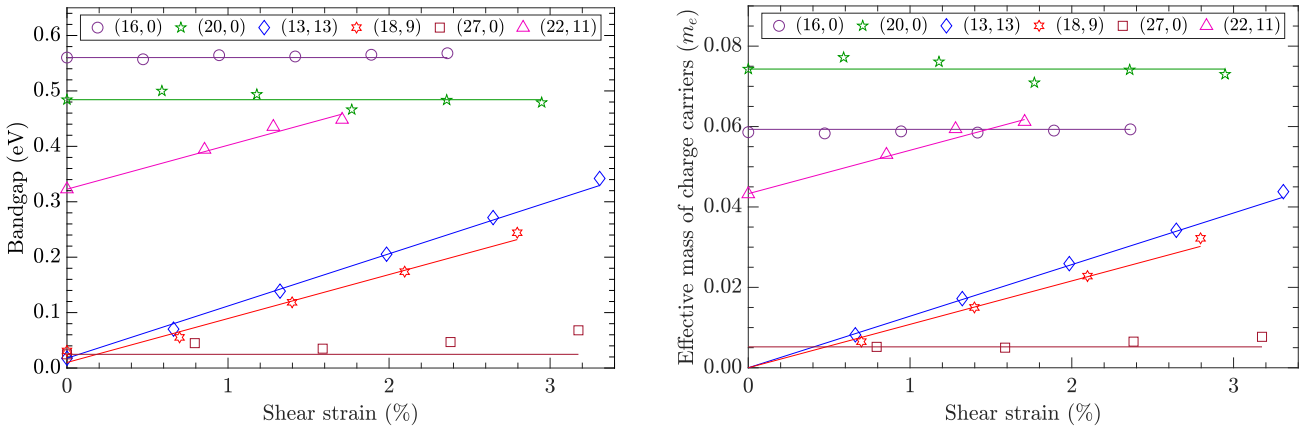

(a) Variation of bandgap with shear strain

(b) Variation of effective mass with shear strain

FIG. 8: Variation of bandgap E_g and effective mass of charge carriers m^* with torsional deformation. The solid lines in (a) and (b) correspond to the laws for bandgap and effective mass that have been presented in Eqs. 85 and 86, respectively.

It is clear from the results above that the $(13, 13)$ and $(18, 9)$ CNTs display a metal to insulator transition on application of torsional deformations. In Fig. 9, choosing the $(18, 9)$ nanotube as a representative example, while considering the untwisted ($\gamma = 0\%$) and highest twisted ($\gamma = 2.8\%$) configurations, we plot at $\nu = 3$ the band structure diagram and density of states (DOS) corresponding to the highest occupied and lowest unoccupied orbitals. For calculating the DOS, we use the relation:

$$D(\lambda) = \frac{1}{N_\eta} \sum_{N_\eta} \sum_{n} \frac{1}{\Delta\sqrt{\pi}} \exp\left[-\left(\frac{\lambda - \lambda_n(\nu, \eta)}{\Delta} \right)^2 \right], \tag{87}$$

where N_η is the number of η-points, the index n runs over the orbitals for which the density of states is being plotted, and Δ is the width of the Gaussian used to smear the Dirac delta function, for which a value of 0.027 eV is employed here. It is clear from the figure that the application of the torsional deformation opens a bandgap of 0.24 eV. The peaks in the DOS correspond to Van Hove singularities, which occur at the extrema points of the band structure diagram. In particular, the similar magnitudes of the two peaks at the bandgap location provides further evidence that the effective mass of electrons and holes is similar. Therefore, it can be concluded that torsional deformations can cause metal to insulator transition in CNTs without changing the relative effective mass of the charge carriers, a result that has implications for nanoelectromechanical devices[122].

C. Large deformation behavior

We now study the mechanical and electronic response of the chosen CNTs to large torsional deformations. In this regime, atomistic calculations suggest that instabilities can develop, accompanied with the breaking of the underlying symmetry.[54,62] However, we still employ the 2-atom unit cell, thereby maintaining the original cyclic+helical symmetry throughout each simulation. This is motivated by the desire to develop a fundamental understanding of the ideal behavior of CNTs when subject to large twists, knowledge of which is also likely important in experiments/applications where these instabilities can be suppressed. Indeed, the ability to perform linear response calculations within the current first principles symmetry-adapted formalism will provide an avenue for identifying the onset and nature of the instabilities from first principles, making it a worthy subject for future research.

1. *Mechanical response*

First, we discuss the mechanical response of the CNTs when subject to large torsional deformations, the results for which are summarized in Fig. 10. The strain energy density increases monotonically until it reaches a maximum value

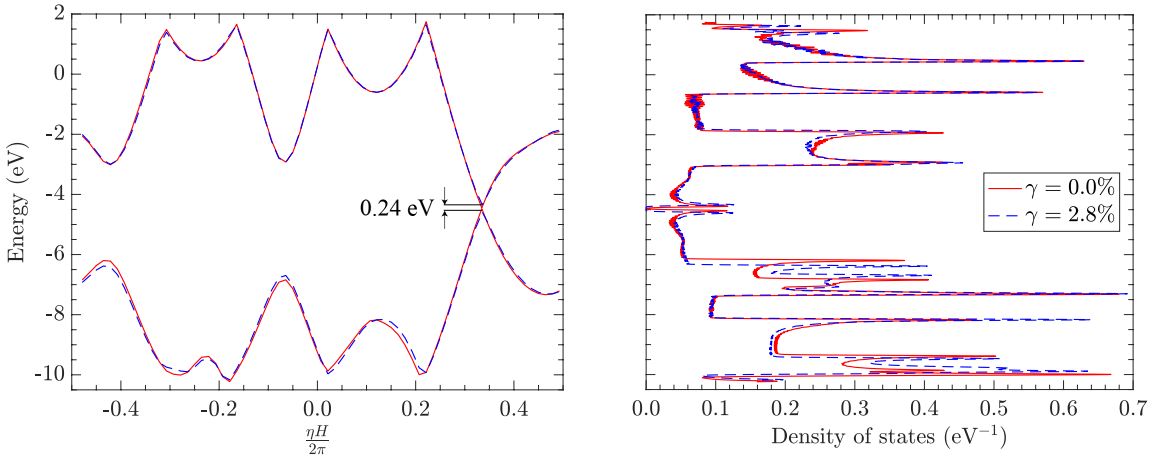

FIG. 9: Band structure diagram (left) and density of states (right) corresponding to the highest occupied and lowest unoccupied orbitals at $\nu = 3$ for the $(18, 9)$ CNT, at both the untwisted ($\gamma = 0\%$) and highest twisted ($\gamma = 2.8\%$) configurations.

— the corresponding twist is referred to as the *ultimate twist* — with the rate of increase being higher for nanotubes with larger diameter, suggesting that the torsional modulus also increases with diameter in the nonlinear regime. The drop in strain energy density beyond the ultimate twist can be attributed to the use of the undeformed axial length (i.e., H) in the engineering definition of the energy density, which does not account for the significant change in length that occurs during large torsional deformations, particularly at the ultimate twist.

The appearance of axial strains during torsional deformations is a consequence of the Poynting effect[54]. This effect, while negligible at small twists, continuously increases with the applied twist, and has a sudden jump at the ultimate twist, where a necking-type phenomenon is observed. The results suggest that the amount of axial strain at the ultimate twist is dependent on the chiral angle, as evidenced by the three zigzag CNTs all having similar axial strain, and the two chiral CNTs both having similar axial strain at the ultimate twist. We also find that the *ultimate strain*, which is the shear strain at the ultimate twist, decreases as the chiral angle increases, with the ultimate twist being inversely proportional to the diameter for zigzag nanotubes.

The drop in strain energy density and corresponding increase in axial strain at the ultimate twist is noticeably larger for the $(13, 13)$ nanotube relative to the other CNTs. This is a consequence of the phase transformation of the $(13, 13)$ armchair nanotube into the $(13, 0)$ zigzag nanotube, which is irreversible from a geometric viewpoint in the context of twist-controlled numerical experiments. We have verified that such an irreversible phase transformation is not just restricted to the $(13, 13)$ nanotube, but is also applicable to other armchair nanotubes, namely the $(16, 16)$ and $(17, 17)$ nanotubes. This is in agreement with past studies that suggest CNTs are susceptible to irreversible phase transformations[123], with the plastic dilation arising from dislocations suggested as a possible avenue[84]. It can therefore be concluded that torsional deformations provide a possible mechanism for the irreversible phase transformation from armchair to zigzag nanotubes.

It is worth noting that to the best of our knowledge, irrespective of the level of theory, the current work is the first to (i) quantify the Poynting effect at large torsional deformations, particularly at the ultimate strain, and (ii) discover that irreversible phase transformation from armchair to zigzag nanotubes can be achieved via torsional deformations.

2. *Electronic response*

Finally, we discuss the electronic response of the chosen CNTs when subject to large torsional deformations, the results for which are presented in Fig. 11. Since the effective mass of the charge carriers follows the same trend as the bandgap, it has been omitted from the figure for the sake of clarity. It is clear that the bandgap shows an oscillatory behavior, in agreement with experiments[124]. In particular, the period for the metal-insulator transition of the armchair and chiral nanotubes follows the law:

$$\Delta\alpha \approx \frac{4a}{d_t^2 \sin(3\omega)}\,, \tag{88}$$

which is also in good agreement with experimental measurements.[124] Recall that a is the nearest neighbor bond length in the CNT. In addition to the above, it is worth noting that among zigzag nanotubes, while type I (i.e., $(16, 0)$)

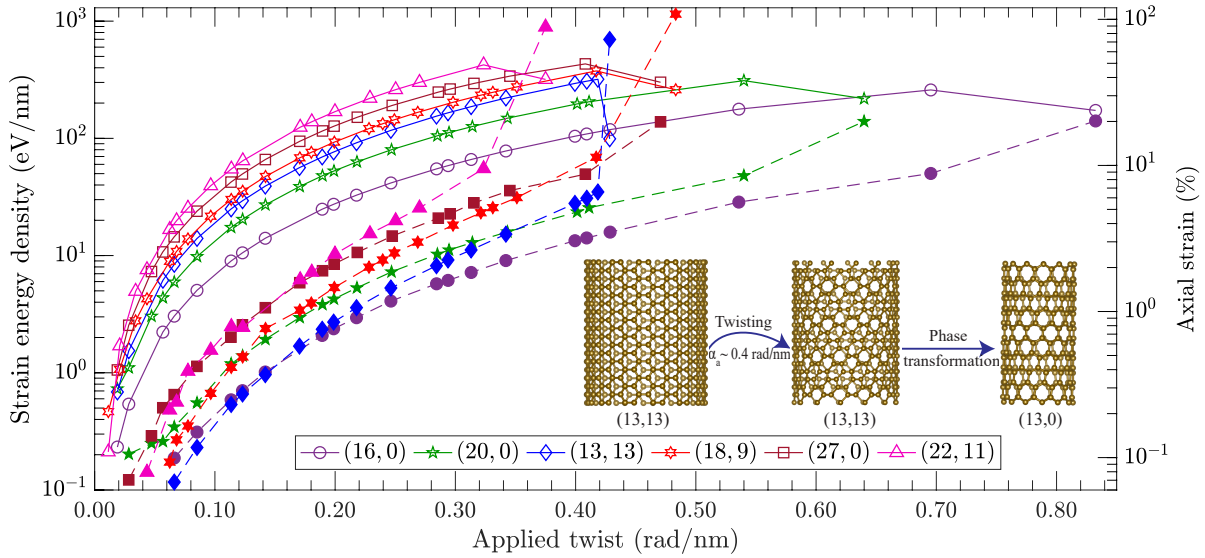

FIG. 10: Variation of strain energy density (hollow markers) and axial strain (filled markers) with respect to applied twist for the CNTs. The phase transformation from the armchair to zigzag nanotube is illustrated at the bottom right of the figure.

and type III (i.e., $(27, 0)$) display an increase followed by decrease of bandgap with twist, the type II (i.e., $(20, 0)$) nanotube exhibits the opposite behavior.

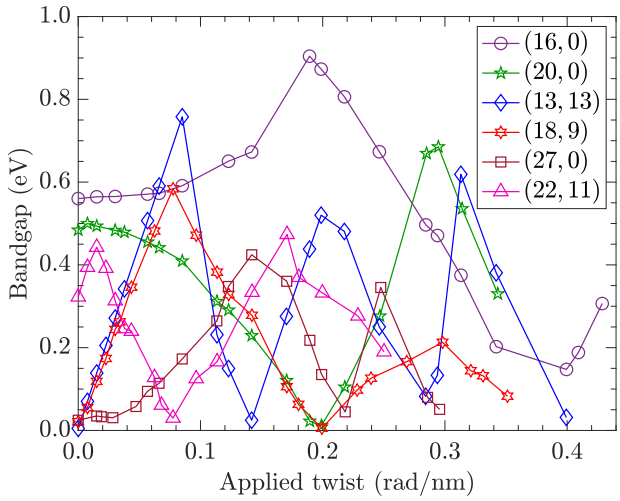

FIG. 11: Variation of bandgap with respect to applied twist for the CNTs.

VIII. CONCLUDING REMARKS

In this work, we have developed a cyclic+helical symmetry-adapted formulation and large-scale parallel implementation of real-space Kohn-Sham DFT for 1D nanostructures, and applied it to study the mechanical and electronic response of CNTs subject to torsional deformations. Specifically, utilizing a local electrostatic formulation and a semilocal exchange-correlation, we have derived symmetry-adapted versions for the energy functional, variational problem governing the electronic ground state, Kohn-Sham equations, Hellmann-Feynman atomic forces, and Hellmann-Feynman axial stress, all written in terms of quantities restricted to the fundamental domain. We have also developed a representation for twisted nanotubes of arbitrary chirality within this framework. In addition, we have developed a high-order finite-difference parallel implementation capable of performing accurate cyclic+helical symmetry-adapted Kohn-Sham calculations in both the static and dynamic setting, which we have verified through

numerical tests and comparisons with traditional DFT codes. Using this implementation, we have performed twist-controlled numerical experiments for a representative set of chiral and achiral carbon nanotubes, in both the small and large deformation regimes. In the linear regime, we have found that the torsional moduli are proportional to the cube of the diameter; metallic nanotubes undergo metal-insulator transitions; and both the effective mass as well as bandgap are proportional to the shear strain and sine of thrice the chiral angle. In the nonlinear regime, we have found that there is significant Poynting effect, particularly at the chiral angle dependent ultimate strain; torsional deformations provide a possible mechanism for the irreversible phase transformation from armchair to zigzag nanotubes; and both the effective mass as well as bandgap have an oscillatory behavior, with the period for metal-insulator transitions being inversely proportional to the square of the diameter and sine of thrice the chiral angle. Wherever available, we have found that all the results are in good agreement with literature, including theoretical and experimental studies. We note that these results are the first to be obtained from DFT, with the current work being the first to make predictions on the effective mass variations, Poynting effect at large strains, and phase transformations through torsional deformations, at any level of theory.

The current work opens an avenue for the accurate and highly efficient first principles study of 1D nanostructures that have cyclic and/or helical symmetry. Applications of this framework are not just limited to systems that inherently have these symmetries[51,125], e.g., nanotubes, nanowires, nanosprings, nanohelices, nanorings, nanocoils, spirals, nanovines, DNA, proteins, and viruses, but also those that result from the application of bending and torsional deformations. In particular, the application of torsional deformations for 1D nanostructures and the application of bending deformations for 2D nanostructures results in systems with these symmetries[51,70,71,102]. Given the large number of such systems and their exotic properties, the current work also provides an avenue for the study of many interesting electromechanical couplings, e.g., the flexoelectric effect arising due to the bending of 2D materials[103,126,127]. To this end, a cyclic+helical symmetry-adapted linear response formalism is likely to serve as an important tool, making it worthy topic for future work.

Acknowledgments

The authors gratefully acknowledge the support of the U.S. National Science Foundation (CAREER1553212). P.S. acknowledges preliminary discussions with Amartya S. Banerjee. The authors acknowledge the valuable comments of the editors and the anonymous referees.

Appendix A: Electrostatic self-interaction and overlap correction

The electrostatic energy term that corrects for the self-interaction and overlap of the individual pseudocharge densities can be written as[86,128]:

$$E_{sc}(\mathbf{R}) = \frac{1}{2}\int_{\Omega}\Big(b(\mathbf{x},\mathbf{R}) + \tilde{b}(\mathbf{x},\mathbf{R})\Big)\,V_c(\mathbf{x},\mathbf{R})\,\mathrm{d}\mathbf{x} - \frac{1}{2}\sum_{J}\int_{\Omega}\tilde{b}_J(\mathbf{x},\mathbf{R}_J)\tilde{V}_J(\mathbf{x},\mathbf{R}_J)\,\mathrm{d}\mathbf{x}\,, \tag{A1}$$

where $\tilde{b} = \sum_J \tilde{b}_J$ is the total reference pseudocharge density due to all nuclei, with $\tilde{b}_J = -\frac{1}{4\pi}\nabla^2\tilde{V}_J$ being the reference pseudocharge density of the $J^{\mathtt{th}}$ nucleus corresponding to the potential $\tilde{V}_J$, and $V_c = \sum_J(\tilde{V}_J - V_J)$. Recall that $b = \sum_J b_J$ is the total pseudocharge density, where $b_J = -\frac{1}{4\pi}\nabla^2 V_J$ is the pseudocharge density of the $J^{\mathtt{th}}$ nucleus with pseudopotential V_J.

The symmetry-adapted expression for the energy can be derived as follows:

$$\begin{aligned}
\hat{E}_{sc}(\hat{\mathbf{R}},\mathcal{G}) &= \frac{1}{|\mathcal{G}|}E_{sc}(\mathbf{R})\\
&= \frac{1}{|\mathcal{G}|}\Bigg(\frac{1}{2}\sum_{\Gamma_{\zeta,\mu}}\int_{\Gamma_{\zeta,\mu}\circ\hat{\Omega}}\Big(b(\mathbf{x},\hat{\mathbf{R}},\mathcal{G}) + \tilde{b}(\mathbf{x},\hat{\mathbf{R}},\mathcal{G})\Big)\,V_c(\mathbf{x},\hat{\mathbf{R}},\mathcal{G})\,\mathrm{d}\mathbf{x} - \frac{1}{2}\sum_{J=1}^{N}\sum_{\Gamma_{\zeta',\mu'}}\sum_{\Gamma_{\zeta,\mu}}\int_{\Gamma_{\zeta,\mu}\circ\hat{\Omega}}\tilde{b}_J(\mathbf{x},\Gamma^{-1}_{\zeta',\mu'}\circ\hat{\mathbf{R}}_J)\\
&\quad\times\tilde{V}_J(\mathbf{x},\Gamma^{-1}_{\zeta',\mu'}\circ\hat{\mathbf{R}}_J)\,\mathrm{d}\mathbf{x}\Bigg)\\
&= \frac{1}{|\mathcal{G}|}\Bigg(\frac{1}{2}\sum_{\Gamma_{\zeta,\mu}}\int_{\hat{\Omega}}\Big(b(\Gamma_{\zeta,\mu}\circ\mathbf{x},\hat{\mathbf{R}},\mathcal{G}) + \tilde{b}(\Gamma_{\zeta,\mu}\circ\mathbf{x},\hat{\mathbf{R}},\mathcal{G})\Big)\,V_c(\Gamma_{\zeta,\mu}\circ\mathbf{x},\hat{\mathbf{R}},\mathcal{G})\,\mathrm{d}\mathbf{x} - \frac{1}{2}\sum_{J=1}^{N}\sum_{\Gamma_{\zeta',\mu'}}\sum_{\Gamma_{\zeta,\mu}}
\end{aligned}$$

$$\int_{\hat{\Omega}} \tilde{b}_J(\Gamma_{\zeta,\mu}\circ\mathbf{x},\Gamma^{-1}_{\zeta',\mu'}\circ\hat{\mathbf{R}}_J)\tilde{V}_J(\Gamma_{\zeta,\mu}\circ\mathbf{x},\Gamma^{-1}_{\zeta',\mu'}\circ\hat{\mathbf{R}}_J)\,\mathrm{d}\mathbf{x}\Bigg)$$

$$= \frac{1}{2}\int_{\hat{\Omega}} \Big(b(\mathbf{x},\hat{\mathbf{R}},\mathcal{G})+\tilde{b}(\mathbf{x},\hat{\mathbf{R}},\mathcal{G})\Big)\,V_c(\mathbf{x},\hat{\mathbf{R}},\mathcal{G})\,\mathrm{d}\mathbf{x} - \frac{1}{2|\mathcal{G}|}\sum_{J=1}^{N}\sum_{\Gamma_{\zeta',\mu'}}\sum_{\Gamma_{\zeta,\mu}}\int_{\hat{\Omega}}\tilde{b}_J(\mathbf{x},\Gamma^{-1}_{\zeta+\zeta',\mu+\mu'}\circ\hat{\mathbf{R}}_J)$$

$$\times\,\tilde{V}_J(\mathbf{x},\Gamma^{-1}_{\zeta+\zeta',\mu+\mu'}\circ\hat{\mathbf{R}}_J)\,\mathrm{d}\mathbf{x}$$

$$= \frac{1}{2}\int_{\hat{\Omega}} \Big(b(\mathbf{x},\hat{\mathbf{R}},\mathcal{G})+\tilde{b}(\mathbf{x},\hat{\mathbf{R}},\mathcal{G})\Big)\,V_c(\mathbf{x},\hat{\mathbf{R}},\mathcal{G})\,\mathrm{d}\mathbf{x} - \frac{1}{2}\sum_{J=1}^{N}\sum_{\Gamma_{\zeta,\mu}}\int_{\hat{\Omega}}\tilde{b}_J(\mathbf{x},\Gamma^{-1}_{\zeta,\mu}\circ\hat{\mathbf{R}}_J)\tilde{V}_J(\mathbf{x},\Gamma^{-1}_{\zeta,\mu}\circ\hat{\mathbf{R}}_J)\,\mathrm{d}\mathbf{x}\,, \quad \text{(A2)}$$

where we have used the fact that b, $\tilde{b}$, and V_c inherit the symmetry of the structure, and that $\tilde{b}_J$ and $\tilde{V}_J$ are spherically symmetric.

The symmetry-adapted expression for the corresponding atomic force can be derived as follows:

$$\mathbf{f}^{sc}_J(\hat{\mathbf{R}},\mathcal{G}) = -\frac{\partial\hat{E}_{sc}(\hat{\mathbf{R}},\mathcal{G})}{\partial\hat{\mathbf{R}}_J}$$

$$= -\frac{1}{2}\int_{\hat{\Omega}}\left(\left(\frac{\partial b(\mathbf{x},\hat{\mathbf{R}},\mathcal{G})}{\partial\hat{\mathbf{R}}_J}+\frac{\partial\tilde{b}(\mathbf{x},\hat{\mathbf{R}},\mathcal{G})}{\partial\hat{\mathbf{R}}_J}\right)V_c(\mathbf{x},\hat{\mathbf{R}},\mathcal{G})+\Big(b(\mathbf{x},\hat{\mathbf{R}},\mathcal{G})+\tilde{b}(\mathbf{x},\hat{\mathbf{R}},\mathcal{G})\Big)\frac{\partial V_c(\mathbf{x},\hat{\mathbf{R}},\mathcal{G})}{\partial\hat{\mathbf{R}}_J}\right)\mathrm{d}\mathbf{x}$$

$$+\frac{1}{2}\sum_{\Gamma_{\zeta,\mu}}\int_{\hat{\Omega}}\left(\frac{\partial\tilde{b}_J(\mathbf{x},\Gamma^{-1}_{\zeta,\mu}\circ\hat{\mathbf{R}}_J)}{\partial\hat{\mathbf{R}}_J}\tilde{V}_J(\mathbf{x},\Gamma^{-1}_{\zeta,\mu}\circ\hat{\mathbf{R}}_J)+\tilde{b}_J(\mathbf{x},\Gamma^{-1}_{\zeta,\mu}\circ\hat{\mathbf{R}}_J)\frac{\partial\tilde{V}_J(\mathbf{x},\Gamma^{-1}_{\zeta,\mu}\circ\hat{\mathbf{R}}_J)}{\partial\hat{\mathbf{R}}_J}\right)\mathrm{d}\mathbf{x}$$

$$= -\frac{1}{2}\sum_{\Gamma_{\zeta,\mu}}\int_{\hat{\Omega}}\left(\left(\frac{\partial b_J(\mathbf{x},\Gamma^{-1}_{\zeta,\mu}\circ\hat{\mathbf{R}}_J)}{\partial\hat{\mathbf{R}}_J}+\frac{\partial\tilde{b}_J(\mathbf{x},\Gamma^{-1}_{\zeta,\mu}\circ\hat{\mathbf{R}}_J)}{\partial\hat{\mathbf{R}}_J}\right)V_c(\mathbf{x},\hat{\mathbf{R}},\mathcal{G})+\Big(b(\mathbf{x},\hat{\mathbf{R}},\mathcal{G})+\tilde{b}(\mathbf{x},\hat{\mathbf{R}},\mathcal{G})\Big)\right.$$

$$\left.\times\,\frac{\partial V_{c,J}(\mathbf{x},\Gamma^{-1}_{\zeta,\mu}\circ\hat{\mathbf{R}}_J)}{\partial\hat{\mathbf{R}}_J}\right)\mathrm{d}\mathbf{x}+\frac{1}{2}\sum_{\Gamma_{\zeta,\mu}}\int_{\hat{\Omega}}\left(\frac{\partial\tilde{b}_J(\mathbf{x},\Gamma^{-1}_{\zeta,\mu}\circ\hat{\mathbf{R}}_J)}{\partial\hat{\mathbf{R}}_J}\tilde{V}_J(\mathbf{x},\Gamma^{-1}_{\zeta,\mu}\circ\hat{\mathbf{R}}_J)+\tilde{b}_J(\mathbf{x},\Gamma^{-1}_{\zeta,\mu}\circ\hat{\mathbf{R}}_J)\frac{\partial\tilde{V}_J(\mathbf{x},\Gamma^{-1}_{\zeta,\mu}\circ\hat{\mathbf{R}}_J)}{\partial\hat{\mathbf{R}}_J}\right)\mathrm{d}\mathbf{x}$$

$$= \frac{1}{2}\sum_{\Gamma_{\zeta,\mu}}\mathfrak{R}^{\mu}_{\varphi}\mathfrak{R}^{\zeta}_{\tilde{\Theta}}\Bigg(\int_{\hat{\Omega}}\Bigg(\Big(\nabla b_J(\mathbf{x},\Gamma^{-1}_{\zeta,\mu}\circ\hat{\mathbf{R}}_J)+\nabla\tilde{b}_J(\mathbf{x},\Gamma^{-1}_{\zeta,\mu}\circ\hat{\mathbf{R}}_J)\Big)V_c(\mathbf{x},\hat{\mathbf{R}},\mathcal{G})+\Big(b(\mathbf{x},\hat{\mathbf{R}},\mathcal{G})+\tilde{b}(\mathbf{x},\hat{\mathbf{R}},\mathcal{G})\Big)$$

$$\times\,\nabla V_{c,J}(\mathbf{x},\Gamma^{-1}_{\zeta,\mu}\circ\hat{\mathbf{R}}_J)\Bigg)\mathrm{d}\mathbf{x}-\int_{\hat{\Omega}}\Big(\nabla\tilde{b}_J(\mathbf{x},\Gamma^{-1}_{\zeta,\mu}\circ\hat{\mathbf{R}}_J)\tilde{V}_J(\mathbf{x},\Gamma^{-1}_{\zeta,\mu}\circ\hat{\mathbf{R}}_J)+\tilde{b}_J(\mathbf{x},\Gamma^{-1}_{\zeta,\mu}\circ\hat{\mathbf{R}}_J)\nabla\tilde{V}_J(\mathbf{x},\Gamma^{-1}_{\zeta,\mu}\circ\hat{\mathbf{R}}_J)\Big)\,\mathrm{d}\mathbf{x}\Bigg)$$

$$= -\frac{1}{2}\sum_{\Gamma_{\zeta,\mu}}\mathfrak{R}^{\mu}_{\varphi}\mathfrak{R}^{\zeta}_{\tilde{\Theta}}\int_{\hat{\Omega}}\Big(b_J(\mathbf{x},\Gamma^{-1}_{\zeta,\mu}\circ\hat{\mathbf{R}}_J)+\tilde{b}_J(\mathbf{x},\Gamma^{-1}_{\zeta,\mu}\circ\hat{\mathbf{R}}_J)\Big)\nabla V_c(\mathbf{x},\hat{\mathbf{R}},\mathcal{G})\,\mathrm{d}\mathbf{x}+\frac{1}{2}\sum_{\Gamma_{\zeta,\mu}}\mathfrak{R}^{\mu}_{\varphi}\mathfrak{R}^{\zeta}_{\tilde{\Theta}}\int_{\hat{\Omega}}\Big(b(\mathbf{x},\hat{\mathbf{R}},\mathcal{G})+\tilde{b}(\mathbf{x},\hat{\mathbf{R}},\mathcal{G})\Big)$$

$$\times\,\nabla V_{c,J}(\mathbf{x},\Gamma^{-1}_{\zeta,\mu}\circ\hat{\mathbf{R}}_J)\,\mathrm{d}\mathbf{x}\,, \quad \text{(A3)}$$

where we have used the fact that b_J and V_J are spherically symmetric. In addition, we have used integration by parts and the divergence theorem.

It is worth noting that the current work is the first to derive the cyclic+helical symmetry-adapted variants of the electrostatic overlap and self-interaction correction energy, and the associated atomic force. In particular, symmetry-adaption of this term is missing from previous works based on cyclic[71] and helical symmetry[72]. As demonstrated previously[34,43], these terms are particularly important in obtaining accurate results while employing the real-space local electrostatic formulation[86,128], a feature common to all these works.

Appendix B: Commutation of Hamiltonian and cyclic+helical symmetry operator

We now show that the Hamiltonian

$$\mathcal{H} = -\frac{1}{2}\nabla^2 + V_{xc} + \phi + V_{nl}\,, \quad \text{(B1)}$$

commutes with the cyclic+helical symmetry operator $\Gamma_{\zeta,\mu}\in\mathcal{G}$. To do so, we need to show that the commutator of $\mathcal{H}$ and $\Gamma_{\zeta,\mu}$:

$$[\mathcal{H}\,,\Gamma_{\zeta,\mu}] = \mathcal{H}\Gamma_{\zeta,\mu} - \Gamma_{\zeta,\mu}\mathcal{H}$$

$$
\begin{aligned}
&= \left(-\frac{1}{2}\nabla^2 + V_{xc} + \phi + V_{nl}\right)\Gamma_{\zeta,\mu} - \Gamma_{\zeta,\mu}\left(-\frac{1}{2}\nabla^2 + V_{xc} + \phi + V_{nl}\right) \\
&= -\frac{1}{2}\left[\nabla^2\,, \Gamma_{\zeta,\mu}\right] + \left[V_{xc}\,, \Gamma_{\zeta,\mu}\right] + \left[\phi\,, \Gamma_{\zeta,\mu}\right] + \left[V_{nl}\,, \Gamma_{\zeta,\mu}\right], \qquad \text{(B2)}
\end{aligned}
$$

is equal to zero. In proving this identity below, we use $\mathbf{x}$ to represent the position vector and f to denote any arbitrary function on which the Hamiltonian and symmetry operators act.

The commutation relationship for the first term in Eq. B2 can be derived as follows:

$$
\begin{aligned}
\langle \mathbf{x}|[\nabla^2\,, \Gamma_{\zeta,\mu}]|f\rangle &= \langle \mathbf{x}|\nabla^2\Gamma_{\zeta,\mu}|f\rangle - \langle \mathbf{x}|\Gamma_{\zeta,\mu}\nabla^2|f\rangle \\
&= \int_\Omega \langle \mathbf{x}|\nabla^2|\mathbf{x}'\rangle\langle \mathbf{x}'|\Gamma_{\zeta,\mu}|f\rangle\,\mathrm{d}\mathbf{x}' - \langle \mathbf{x}|\Gamma_{\zeta,\mu}|g\rangle \qquad \left[\int_\Omega |\mathbf{x}'\rangle\langle \mathbf{x}'|\,\mathrm{d}\mathbf{x}' = \mathcal{I}\,,\ |g\rangle = \nabla^2|f\rangle\right] \\
&= \int_\Omega \langle \mathbf{x}|\nabla^2|\mathbf{x}'\rangle f(\Gamma^{-1}_{\zeta,\mu}\circ\mathbf{x}')\,\mathrm{d}\mathbf{x}' - g(\Gamma^{-1}_{\zeta,\mu}\circ\mathbf{x}) \\
&= \nabla^2_{\mathbf{x}} f(\Gamma^{-1}_{\zeta,\mu}\circ\mathbf{x}) - g(\Gamma^{-1}_{\zeta,\mu}\circ\mathbf{x}) \qquad \left[\nabla_{\mathbf{x}} = \frac{\partial}{\partial x_1}\hat{\mathbf{e}}_{x_1} + \frac{\partial}{\partial x_2}\hat{\mathbf{e}}_{x_2} + \frac{\partial}{\partial x_3}\hat{\mathbf{e}}_{x_3}\right] \\
&= \nabla^2_{\mathbf{x}} f(\mathfrak{R}^{-\mu}_{\varphi}\mathfrak{R}^{-\zeta}_{\tilde{\Theta}}\mathbf{x}) - g(\mathfrak{R}^{-\mu}_{\varphi}\mathfrak{R}^{-\zeta}_{\tilde{\Theta}}\mathbf{x}) \\
&= \nabla^T_{\mathbf{y}}\left(\mathfrak{R}^{-\mu}_{\varphi}\mathfrak{R}^{-\zeta}_{\tilde{\Theta}}\right)\left(\mathfrak{R}^{-\mu}_{\varphi}\mathfrak{R}^{-\zeta}_{\tilde{\Theta}}\right)^T\nabla_{\mathbf{y}} f(\mathbf{y}) - g(\mathbf{y}) \qquad \left[\mathbf{y} = \mathfrak{R}^{-\mu}_{\varphi}\mathfrak{R}^{-\zeta}_{\tilde{\Theta}}\mathbf{x}\right] \\
&= \nabla^2_{\mathbf{y}} f(\mathbf{y}) - g(\mathbf{y}) \\
&= 0\,, \qquad \text{(B3)}
\end{aligned}
$$

where the sixth equality is obtained by using the chain rule, and the seventh equality is obtained by using the orthonormality of the rotation matrices.

The commutation relationship for the second term in Eq. B2 can be derived as follows:

$$
\begin{aligned}
\langle \mathbf{x}|[V_{xc}\,, \Gamma_{\zeta,\mu}]|f\rangle &= \langle \mathbf{x}|V_{xc}\Gamma_{\zeta,\mu}|f\rangle - \langle \mathbf{x}|\Gamma_{\zeta,\mu}V_{xc}|f\rangle \\
&= \int_\Omega \langle \mathbf{x}|V_{xc}|\mathbf{x}'\rangle\langle \mathbf{x}'|\Gamma_{\zeta,\mu}|f\rangle\,\mathrm{d}\mathbf{x}' - \langle \mathbf{x}|\Gamma_{\zeta,\mu}|g\rangle \qquad \left[|g\rangle = V_{xc}|f\rangle\right] \\
&= \int_\Omega \langle \mathbf{x}|V_{xc}|\mathbf{x}'\rangle f(\Gamma^{-1}_{\zeta,\mu}\circ\mathbf{x}')\,\mathrm{d}\mathbf{x}' - g(\Gamma^{-1}_{\zeta,\mu}\circ\mathbf{x}) \\
&= V_{xc}(\mathbf{x}) f(\Gamma^{-1}_{\zeta,\mu}\circ\mathbf{x}) - g(\Gamma^{-1}_{\zeta,\mu}\circ\mathbf{x}) \\
&= V_{xc}(\mathbf{x}) f(\Gamma^{-1}_{\zeta,\mu}\circ\mathbf{x}) - V_{xc}(\Gamma^{-1}_{\zeta,\mu}\circ\mathbf{x}) f(\Gamma^{-1}_{\zeta,\mu}\circ\mathbf{x}) \\
&= V_{xc}(\mathbf{x}) f(\mathbf{y}) - \left(\varepsilon_{xc}(\rho(\mathbf{y}), |\nabla_{\mathbf{y}}\rho(\mathbf{y})|) + \rho(\mathbf{y})\frac{\partial\varepsilon_{xc}(\rho(\mathbf{y}), |\nabla_{\mathbf{y}}\rho(\mathbf{y})|)}{\partial\rho(\mathbf{y})}\right. \\
&\quad \left. - \nabla_{\mathbf{y}}\cdot\left(\frac{\rho(\mathbf{y})}{|\nabla_{\mathbf{y}}\rho(\mathbf{y})|}\frac{\partial\varepsilon_{xc}(\rho(\mathbf{y}), |\nabla_{\mathbf{y}}\rho(\mathbf{y})|)}{\partial\left(|\nabla_{\mathbf{y}}\rho(\mathbf{y})|\right)}\nabla_{\mathbf{y}}\rho(\mathbf{y})\right)\right) f(\mathbf{y}) \qquad \left[\mathbf{y} = \Gamma^{-1}_{\zeta,\mu}\circ\mathbf{x}\right] \\
&= V_{xc}(\mathbf{x}) f(\mathbf{y}) - \left(\varepsilon_{xc}(\rho(\mathbf{x}), |\nabla_{\mathbf{x}}\rho(\mathbf{x})|) + \rho(\mathbf{x})\frac{\partial\varepsilon_{xc}(\rho(\mathbf{x}), |\nabla_{\mathbf{x}}\rho(\mathbf{x})|)}{\partial\rho(\mathbf{x})}\right. \\
&\quad \left. - \left(\mathfrak{R}^{-\mu}_{\varphi}\mathfrak{R}^{-\zeta}_{\tilde{\Theta}}\right)^T\nabla_{\mathbf{x}}\cdot\left(\frac{\rho(\mathbf{x})}{|\nabla_{\mathbf{x}}\rho(\mathbf{x})|}\frac{\partial\varepsilon_{xc}(\rho(\mathbf{x}), |\nabla_{\mathbf{x}}\rho(\mathbf{x})|)}{\partial\left(|\nabla_{\mathbf{x}}\rho(\mathbf{x})|\right)}\left(\mathfrak{R}^{-\mu}_{\varphi}\mathfrak{R}^{-\zeta}_{\tilde{\Theta}}\right)^T\nabla_{\mathbf{x}}\rho(\mathbf{x})\right)\right) f(\mathbf{y}) \\
&= V_{xc}(\mathbf{x}) f(\mathbf{y}) - \varepsilon_{xc}(\rho(\mathbf{x}), |\nabla_{\mathbf{x}}\rho(\mathbf{x})|) + \rho(\mathbf{x})\frac{\partial\varepsilon_{xc}(\rho(\mathbf{x}), |\nabla_{\mathbf{x}}\rho(\mathbf{x})|)}{\partial\rho(\mathbf{x})} \\
&\quad - \nabla_{\mathbf{x}}\cdot\left(\frac{\rho(\mathbf{x})}{|\nabla_{\mathbf{x}}\rho(\mathbf{x})|}\frac{\partial\varepsilon_{xc}(\rho(\mathbf{x}), |\nabla_{\mathbf{x}}\rho(\mathbf{x})|)}{\partial\left(|\nabla_{\mathbf{x}}\rho(\mathbf{x})|\right)}\nabla_{\mathbf{x}}\rho(\mathbf{x})\right) f(\mathbf{y}) \\
&= V_{xc}(\mathbf{x}) f(\mathbf{y}) - V_{xc}(\mathbf{x}) f(\mathbf{y}) \\
&= 0\,, \qquad \text{(B4)}
\end{aligned}
$$

where the fourth equality is obtained using the fact that V_{xc} is a diagonal operator, and the seventh equality is obtained by using the fact that electron density and the norm of its gradient are commensurate with the symmetry

of the structure, while the gradient of the electron density transforms as the position vector when acted upon by the symmetry operator.

The commutation relationship for the third term in Eq. B2 can be derived as follows:

$$\begin{aligned}
\langle \mathbf{x}|[\phi\,,\Gamma_{\zeta,\mu}]|f\rangle &= \langle \mathbf{x}|\phi\Gamma_{\zeta,\mu}|f\rangle - \langle \mathbf{x}|\Gamma_{\zeta,\mu}\phi|f\rangle \\
&= \int_{\Omega} \langle \mathbf{x}|\phi|\mathbf{x}'\rangle\langle \mathbf{x}'|\Gamma_{\zeta,\mu}|f\rangle\,\mathrm{d}\mathbf{x}' - \langle \mathbf{x}|\Gamma_{\zeta,\mu}|g\rangle \qquad \Big[|g\rangle = \phi|f\rangle\Big] \\
&= \phi(\mathbf{x})f(\Gamma_{\zeta,\mu}^{-1}\circ\mathbf{x}) - \phi(\Gamma_{\zeta,\mu}^{-1}\circ\mathbf{x})f(\Gamma_{\zeta,\mu}^{-1}\circ\mathbf{x}) \\
&= \phi(\mathbf{x})f(\Gamma_{\zeta,\mu}^{-1}\circ\mathbf{x}) - \phi(\mathbf{x})f(\Gamma_{\zeta,\mu}^{-1}\circ\mathbf{x}) \\
&= 0\,,
\end{aligned} \tag{B5}$$

where the third equality is obtained using the fact that ϕ is a diagonal operator, and the fourth equality is obtained by using the fact that ϕ is commensurate with the symmetry of the structure (Eq. 19).

The commutation relationship for the fourth term in Eq. B2 can be derived as follows:

$$\begin{aligned}
\langle \mathbf{x}|[V_{nl}\,,\Gamma_{\zeta,\mu}]|f\rangle &= \langle \mathbf{x}|V_{nl}\Gamma_{\zeta,\mu}|f\rangle - \langle \mathbf{x}|\Gamma_{\zeta,\mu}V_{nl}|f\rangle \\
&= \langle \mathbf{x}|\sum_J\sum_{p=1}^{\mathcal{P}_J}\gamma_{J;p}|\chi_{J;p}\rangle\langle\chi_{J;p}|\Gamma_{\zeta,\mu}f\rangle - \langle \mathbf{x}|\Gamma_{\zeta,\mu}\sum_J\sum_{p=1}^{\mathcal{P}_J}\gamma_{J;p}|\chi_{J;p}\rangle\langle\chi_{J;p}|f\rangle \\
&= \sum_J\sum_{p=1}^{\mathcal{P}_J}\gamma_{J;p}\chi_{J;p}(\mathbf{x},\mathbf{R}_J)\int_{\Omega}\chi^*_{J;p}(\mathbf{y},\mathbf{R}_J)\Gamma_{\zeta,\mu}f(\mathbf{y})\,\mathrm{d}\mathbf{y} - \sum_J\sum_{p=1}^{\mathcal{P}_J}\gamma_{J;p}\langle\mathbf{x}|\Gamma_{\zeta,\mu}\chi_{J;p}\rangle\langle\chi_{J;p}|f\rangle \\
&= \sum_J\sum_{p=1}^{\mathcal{P}_J}\gamma_{J;p}\chi_{J;p}(\mathbf{x},\mathbf{R}_J)\int_{\Omega}\chi^*_{J;p}(\mathbf{y},\mathbf{R}_J)f(\Gamma_{\zeta,\mu}^{-1}\circ\mathbf{y})\,\mathrm{d}\mathbf{y} - \sum_J\sum_{p=1}^{\mathcal{P}_J}\gamma_{J;p}\chi_{J;p}(\Gamma_{\zeta,\mu}^{-1}\circ\mathbf{x},\mathbf{R}_J)\langle\chi_{J;p}|f\rangle \\
&= \sum_J\sum_{p=1}^{\mathcal{P}_J}\gamma_{J;p}\chi_{J;p}(\mathbf{x},\mathbf{R}_J)\int_{\Gamma_{\zeta,\mu}^{-1}\circ\Omega}\chi^*_{J;p}(\Gamma_{\zeta,\mu}\circ\mathbf{z},\mathbf{R}_J)f(\mathbf{z})\,\mathrm{d}\mathbf{z} - \sum_J\sum_{p=1}^{\mathcal{P}_J}\gamma_{J;p}\chi_{J;p}(\Gamma_{\zeta,\mu}^{-1}\circ\mathbf{x},\mathbf{R}_J)\langle\chi_{J;p}|f\rangle \\
&= \sum_J\sum_{p=1}^{\mathcal{P}_J}\gamma_{J;p}\chi_{J;p}(\mathbf{x},\mathbf{R}_J)\int_{\Omega}\chi^*_{J;p}(\Gamma_{\zeta,\mu}\circ\mathbf{z},\mathbf{R}_J)f(\mathbf{z})\,\mathrm{d}\mathbf{z} - \sum_J\sum_{p=1}^{\mathcal{P}_J}\gamma_{J;p}\chi_{J;p}(\Gamma_{\zeta,\mu}^{-1}\circ\mathbf{x},\mathbf{R}_J)\langle\chi_{J;p}|f\rangle \\
&= \sum_J\sum_{p=1}^{\mathcal{P}_J}\gamma_{J;p}\chi_{J;p}(\mathbf{x},\mathbf{R}_J)\int_{\Omega}\chi^*_{J;p}(\Gamma_{\zeta,\mu}\circ\mathbf{z},\Gamma_{\zeta,\mu}\circ\mathbf{R}_{J'})f(\mathbf{z})\,\mathrm{d}\mathbf{z} - \sum_J\sum_{p=1}^{\mathcal{P}_J}\gamma_{J;p}\chi_{J;p}(\Gamma_{\zeta,\mu}^{-1}\circ\mathbf{x},\Gamma_{\zeta,\mu}^{-1}\circ\mathbf{R}_{J''})\langle\chi_{J;p}|f\rangle \\
&= \sum_J\sum_{p=1}^{\mathcal{P}_J}\gamma_{J;p}\chi_{J;p}(\mathbf{x},\mathbf{R}_J)\int_{\Omega}\chi^*_{J';p}(\mathbf{z},\mathbf{R}_{J'})e^{-im_p(\zeta\tilde{\Theta}+\mu\varphi)}f(\mathbf{z})\,\mathrm{d}\mathbf{z} - \sum_J\sum_{p=1}^{\mathcal{P}_J}\gamma_{J;p}\chi_{J'';p}(\mathbf{x},\mathbf{R}_{J''})e^{im_p(-\zeta\tilde{\Theta}-\mu\varphi)}\langle\chi_{J;p}|f\rangle \\
&= \sum_J\sum_{p=1}^{\mathcal{P}_J}\gamma_{J;p}\chi_{J;p}(\mathbf{x},\mathbf{R}_J)e^{-im_p(\zeta\tilde{\Theta}+\mu\varphi)}\langle\chi_{J';p}|f\rangle - \sum_J\sum_{p=1}^{\mathcal{P}_J}\gamma_{J;p}\chi_{J'';p}(\mathbf{x},\mathbf{R}_{J''})e^{-im_p(\zeta\tilde{\Theta}+\mu\varphi)}\langle\chi_{J;p}|f\rangle \\
&= \sum_J\sum_{p=1}^{\mathcal{P}_J}\gamma_{J;p}\chi_{J'';p}(\mathbf{x},\mathbf{R}_{J''})e^{-im_p(\zeta\tilde{\Theta}+\mu\varphi)}\langle\chi_{J;p}|f\rangle - \sum_J\sum_{p=1}^{\mathcal{P}_J}\gamma_{J;p}\chi_{J'';p}(\mathbf{x},\mathbf{R}_{J''})e^{-im_p(\zeta\tilde{\Theta}+\mu\varphi)}\langle\chi_{J;p}|f\rangle \\
&= 0\,,
\end{aligned} \tag{B6}$$

where the sixth equality is obtained by using the fact that the domain remains unchanged upon the action of the symmetry operator; the seventh equality is obtained by using the fact that every atom can be uniquely written as the action of a symmetry operator on some other atom in the system; the eighth equality is obtained by using the fact that every nonlocal projector can be written as the product of a radial function and a spherical harmonic, and the action of $\Gamma_{\zeta,\mu}$ on spherical harmonics results in picking up of a constant phase factor $e^{im_p(\zeta\tilde{\Theta}+\mu\varphi)}$, where m_p is the magnetic quantum number associated with the p^{th} projector of the atom; and the ninth equality is obtained using the fact that all images of an atom have the same normalization constant and projectors.

It therefore follows from Eqs. B2—B5 that

$$[\mathcal{H}\,,\Gamma_{\zeta,\mu}] = 0\,, \tag{B7}$$

thereby proving that the Hamiltonian operator commutes with the cyclic+helical symmetry operators. Note that the current work is the first to prove this result, with previous works on cyclic[71] and helical[72] symmetry-adaption assuming its validity. Indeed, the current proof directly extends to the local exchange-correlation functionals adopted there[71,72], which offers considerable simplification in this regard.

Appendix C: Radial boundary conditions for electrostatic potential

The Dirichlet boundary conditions prescribed on the electrostatic potential ϕ—solution of the symmetry-adapted Poisson problem (Eq. 37)—in the radial direction are of the form:

$$\phi(r \leq R_1, \tilde{\theta}, z, \hat{\mathbf{R}}, \mathcal{G}) = \phi_1 \,, \quad \phi(r \geq R_2, \tilde{\theta}, z, \hat{\mathbf{R}}, \mathcal{G}) = \phi_2 \,. \tag{C1}$$

where appropriate values of ϕ_1 and ϕ_2 need to determined. The simplest choice is $\phi_1 = \phi_2 = 0$, an approximation adopted in previous work[71,72], which is likely to work well in systems that do not have a significant dipole moment across the surfaces of the structure. However, when such a dipole moment exists, as is commonly encountered in 1D nanostructures due to the flexoelectric effect[126,127,129], convergence of the results with vacuum can be extremely slow, if at all. This is a consequence of an artificial electric field being introduced across the surfaces of the structure when zero-Dirichlet boundary conditions are employed. To overcome this, here we develop boundary conditions that account for the dipole moment contribution to the electrostatic potential.

As shown in Section III B, the electrostatic potential ϕ, electron density ρ, and pseudocharge density b inherit the symmetry of the structure, i.e., for $f \in \{\phi, \rho, b\}$, we have the following relations in helical coordinates:

$$f(r, \tilde{\theta} + \tilde{\Theta}, z) = f(r, \tilde{\theta}, z) \,, \quad f(r, \tilde{\theta}, z + H) = f(r, \tilde{\theta}, z) \,. \tag{C2}$$

Given the periodic nature of the function in the the $\tilde{\theta}$ and z directions, it admits a Fourier decomposition of the form:

$$f(r, \tilde{\theta}, z) = \bar{f}(r) + \sum_{m,n \in \mathbb{Z}\setminus 0} \bar{f}_{m,n}(r) \exp\left(i \frac{2\pi m \tilde{\theta}}{\tilde{\Theta}} + i \frac{2\pi n z}{H} \right) \,, \tag{C3}$$

where

$$\bar{f}(r) = \frac{1}{\tilde{\Theta} H} \int_z \int_{\tilde{\theta}} f(r, \tilde{\theta}, z) \, \mathrm{d}\tilde{\theta} \, \mathrm{d}z \,. \tag{C4}$$

Substituting this expansion for ρ, b, and ϕ into the Poisson equation (Eq. 37), we arrive at the following differential equation involving the first term in each Fourier expansion:

$$-\frac{1}{4\pi} \left(\frac{d^2 \bar{\phi}(r)}{dr^2} + \frac{1}{r} \frac{d\bar{\phi}(r)}{dr} \right) = \bar{\rho}(r) + \bar{b}(r) \,, \tag{C5}$$

whose solution in integral form can be written as

$$\bar{\phi}(r) = -4\pi \int \left(\bar{\rho}(r') + \bar{b}(r') \right) G(r, r') \, \mathrm{d}r' \,, \tag{C6}$$

where the Green's function

$$G(r, r') = -\frac{1}{2\pi} \begin{cases} \ln r', & \text{for } r < r' \\ \ln r, & \text{for } r > r' \end{cases} \,. \tag{C7}$$

Thereafter, we arrive at the following boundary conditions:

$$\phi_1 = \bar{\phi}(r \leq R_1) = 2 \int_{R_1}^{R_2} \left(\bar{\rho}(r') + \bar{b}(r') \right) \ln r' \, \mathrm{d}r' \tag{C8}$$

$$\phi_2 = \bar{\phi}(r \geq R_2) = 2 \ln r \int_{R_1}^{R_2} \left(\bar{\rho}(r') + \bar{b}(r') \right) \, \mathrm{d}r' \,. \tag{C9}$$

Note that we have neglected the higher-order terms in the expansion, since the current approximation already provides rapid convergence with vacuum for systems with a dipole moment. Also note that a procedure similar to the one described here has been used previously to obtain the boundary conditions for slabs in real-space DFT[130].

Appendix D: Symmetry-adapted quantum molecular dynamics

We now demonstrate that Cyclix-DFT is capable of performing symmetry-adapted quantum molecular dynamics (QMD) simulations. For this study, we perform a NVE microcanonical ensemble simulation for the $(16, 0)$ CNT with a 32-atom unit cell generated by applying the symmetry operation $\Gamma_{\zeta,\mu}$ on the fundamental domain and atoms of the nanotube, where $\zeta \in \{0, 1\}$ and $\mu \in \{0, 1, \cdots, 7\}$. Note that even though the nanotube is achiral, the above choice results in $\alpha \neq 0$, making it representative of general QMD simulations within Cyclix-DFT. We employ a mesh size of 0.25 Bohr, vacuum of 7 Bohr, $N_\eta = 1$ for Brillouin zone integration, initial ionic temperature of 315.773 K, time step of 1 fs, initial velocities randomly assigned according to Maxwell-Boltzmann distribution, and the Leapfrog method[131] to integrate the equations of motion. In Fig. 12, we present the evolution of the total energy of the system, which is the sum of the electronic Helmholtz free energy and the ionic kinetic energy. It is clear that there is excellent conservation in the total energy, with the standard deviation and drift being 5.2×10^{-5} Ha/atom and 6×10^{-5} Ha/atom-ps, respectively, further verifying that there is no systematic error in the formulation and implementation of Cyclix DFT. Therefore, Cyclix-DFT can be used to efficiently study the dynamic behavior of systems with cyclic+helical symmetry. In particular, the highly efficient nature of Cyclix DFT, where the wall time associated with the solution of the Kohn-Sham equations can be brought down to a few seconds, enables simulations that were previously intractable.

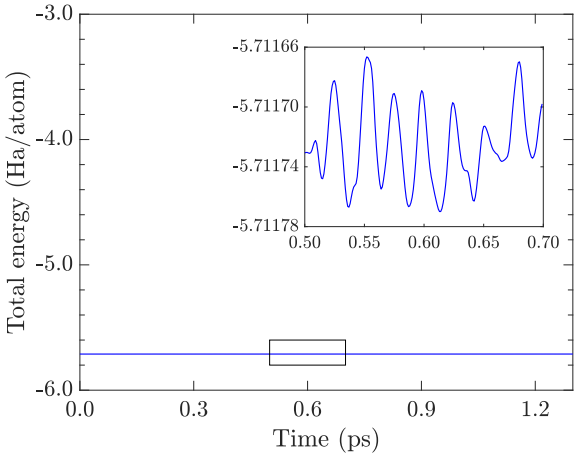

FIG. 12: Variation in total energy for a 32-atom unit cell of a $(16, 0)$ carbon nanotube during a NVE symmetry-adapted QMD simulation. The inset magnifies the variation in total energy between 0.5 and 0.7 ps.

Appendix E: Cyclic+helical symmetry-adapted study of carbon nanocoil

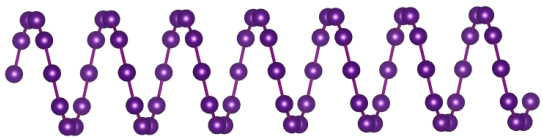

FIG. 13: Illustration of a carbon nanocoil.

In this work, we have focused on applying the cyclic+helical symmetry-adapted formulation and implementation of Kohn-Sham DFT to carbon nanotubes. However, the method is not restricted to this type of system, and is generally applicable all 1D nanostructures that have cyclic and/or helical symmetry. To demonstrate this, we now verify the accuracy of Cyclix-DFT for carbon nanocoils[132,133]. Specifically, we consider a prototype carbon nanocoil with $N = 1$ atom in the fundamental domain, $\mathfrak{N} = 1$ cyclic group order, and intrinsic twist of $\alpha = 0.2094$ rad/Bohr, as illustrated in Fig. 13. We compare the results obtained by Cyclix-DFT with highly converged SPARC[8,34,43] and ABINIT[111] calculations, while employing a mesh-size of 0.2 Bohr and 60 $\eta-$points in Cyclix DFT. In comparison to SPARC, we find that there is very good agreement of 4×10^{-5} Ha/atom, 1×10^{-6} Ha/Bohr, and 0.1% in energy, forces, and stress, respectively. The corresponding agreement with ABINIT is 2×10^{-5} Ha/atom, 2×10^{-6} Ha/Bohr, and

0.1%, respectively. These differences are well within the accuracy targeted in DFT calculations, further verifying the accuracy of the proposed symmetry-adapted formulation and implementation.

---

* Electronic address: phanish.suryanarayana@ce.gatech.edu

[1] P. Hohenberg and W. Kohn, Phys. Rev. **136**, B864 (1964).
[2] W. Kohn and L. J. Sham, Phys. Rev. **140**, A1133 (1965).
[3] B. Austin, W. Bhimji, T. Butler, and J. Deslippe, *2014 NERSC workload analysis*, http://portal.nersc.gov/project/mpccc/baustin/NERSC_2014_Workload_Analysis_v1.1.pdf.
[4] L. J. Vernon, *IC Application Performance Team analysis, as part of IC Knights Special Project*, Tech. Rep. LANL, 2015.
[5] K. Burke, J. Chem. Phys. **136**, 150901 (2012).
[6] A. D. Becke, J. Chem. Phys. **140**, 18A301 (2014).
[7] R. Martin, *Electronic Structure: Basic theory and practical methods* (Cambridge University Press, 2004).
[8] Q. Xu, A. Sharma, B. Comer, H. Huang, E. Chow, A. Medford, J. Pask, and P. Suryanarayana, arXiv:2005.10431 (2020).
[9] G. Kresse and J. Furthmüller, Phys. Rev. B **54**, 11169 (1996).
[10] M. D. Segall, P. J. D. Lindan, M. J. Probert, C. J. Pickard, P. J. Hasnip, S. J. Clark, and M. C. Payne, J. Phys.: Condens. Matter **14**, 2717 (2002).
[11] X. Gonze, B. Amadon, P.-M. Anglade, J.-M. Beuken, F. Bottin, P. Boulanger, F. Bruneval, D. Caliste, R. Caracas, M. Cote, et al., Comput. Phys. Commun. **180**, 2582 (2009).
[12] P. Giannozzi, S. Baroni, N. Bonini, M. Calandra, R. Car, C. Cavazzoni, D. Ceresoli, G. L. Chiarotti, M. Cococcioni, I. Dabo, et al., J. Phys.: Condens. Matter **21**, 395502 (19pp) (2009).
[13] M. Valiev, E. Bylaska, N. Govind, K. Kowalski, T. Straatsma, H. V. Dam, D. Wang, J. Nieplocha, E. Apra, T. Windus, et al., Comput. Phys. Commun. **181**, 1477 (2010).
[14] S. Goedecker, Rev. Mod. Phys. **71**, 1085 (1999).
[15] D. R. Bowler and T. Miyazaki, Rep. Prog. Phys. **75**, 036503 (2012).
[16] J. Aarons, M. Sarwar, D. Thompsett, and C.-K. Skylaris, J. Chem. Phys. **145**, 220901 (2016).
[17] A. D. Becke, International Journal of Quantum Chemistry **36**, 599 (1989).
[18] J. R. Chelikowsky, N. Troullier, and Y. Saad, Phys. Rev Lett. **72**, 1240 (1994).
[19] L. Genovese, A. Neelov, S. Goedecker, T. Deutsch, S. A. Ghasemi, A. Willand, D. Caliste, O. Zilberberg, M. Rayson, A. Bergman, et al., The J. Chem. Phys. **129**, 014109 (2008).
[20] A. P. Seitsonen, M. J. Puska, and R. M. Nieminen, Phys. Rev. B **51**, 14057 (1995).
[21] S. R. White, J. W. Wilkins, and M. P. Teter, Phys. Rev. B **39**, 5819 (1989).
[22] J.-I. Iwata, D. Takahashi, A. Oshiyama, T. Boku, K. Shiraishi, S. Okada, and K. Yabana, Journal of Computational Physics **229**, 2339 (2010).
[23] E. Tsuchida and M. Tsukada, Phys. Rev. B **52**, 5573 (1995).
[24] Q. Xu, P. Suryanarayana, and J. E. Pask, J. Chem. Phys. **149**, 094104 (2018).
[25] P. Suryanarayana, K. Bhattacharya, and M. Ortiz, J Comput. Phys. **230**, 5226 (2011).
[26] P. Suryanarayana, V. Gavini, T. Blesgen, K. Bhattacharya, and M. Ortiz, J. Mech. Phys. Solids **58**, 256 (2010).
[27] C.-K. Skylaris, P. D. Haynes, A. A. Mostofi, and M. C. Payne, J. Chem. Phys. **122**, 084119 (2005).
[28] D. R. Bowler, R. Choudhury, M. J. Gillan, and T. Miyazaki, Phys. Status Solidi B **243**, 989 (2006).
[29] P. Motamarri, S. Das, S. Rudraraju, K. Ghosh, D. Davydov, and V. Gavini, Comput. Phys. Commun. **246**, 106853 (2020), ISSN 0010-4655.
[30] A. Castro, H. Appel, M. Oliveira, C. A. Rozzi, X. Andrade, F. Lorenzen, M. A. L. Marques, E. K. U. Gross, and A. Rubio, Phys. Status Solidi B **243**, 2465 (2006).
[31] E. Briggs, D. Sullivan, and J. Bernholc, Phys. Rev. B **54**, 14362 (1996).
[32] J.-L. Fattebert, J. Comput. Phys. **149**, 75 (1999).
[33] F. Shimojo, R. K. Kalia, A. Nakano, and P. Vashishta, Comput. Phys. Commun. **140**, 303 (2001).
[34] S. Ghosh and P. Suryanarayana, Comput. Phys. Commun. **216**, 109 (2017).
[35] T. A. Arias, Rev. Mod. Phys. **71**, 267 (1999).
[36] J. E. Pask and P. A. Sterne, Model. Simul. Mater. Sci. Eng. **13**, R71 (2005).
[37] L. Lin, J. Lu, L. Ying, and E. Weinan, J. Comput. Phys. **231**, 2140 (2012).
[38] T. L. Beck, Rev. Mod. Phys. **72**, 1041 (2000).
[39] Y. Saad, J. R. Chelikowsky, and S. M. Shontz, SIAM Rev. **52**, 3 (2010).
[40] D. Osei-Kuffuor and J.-L. Fattebert, Phys. Rev. Lett. **112**, 046401 (2014).
[41] P. Suryanarayana, P. P. Pratapa, A. Sharma, and J. E. Pask, Comput. Phys. Commun. **224**, 288 (2018).
[42] Y. Hasegawa, J.-I. Iwata, M. Tsuji, D. Takahashi, A. Oshiyama, K. Minami, T. Boku, F. Shoji, A. Uno, M. Kurokawa, et al., in *Proceedings of 2011 International Conference for High Performance Computing, Networking, Storage and Analysis* (ACM, 2011), p. 1.
[43] S. Ghosh and P. Suryanarayana, Comput. Phys. Commun. **212**, 189 (2017).
[44] W.-Y. Ching and P. Rulis, *Electronic Structure Methods for Complex Materials: The orthogonalized linear combination of atomic orbitals* (Oxford University Press, 2012).

[45] D. Willock, *Molecular symmetry* (John Wiley & Sons, 2009).
[46] T. B. Prayitno and F. Ishii, J. Phys. Soc. Japan **87**, 114709 (2018).
[47] J. M. Turney, A. C. Simmonett, R. M. Parrish, E. G. Hohenstein, F. A. Evangelista, J. T. Fermann, B. J. Mintz, L. A. Burns, J. J. Wilke, M. L. Abrams, et al., Wiley Interdiscip. Rev. Comput. Mol. Sci. **2**, 556 (2012).
[48] A. Erba, J. Baima, I. Bush, R. Orlando, and R. Dovesi, J. Chem. Theory Comput. **13**, 5019 (2017).
[49] Y. Xia, P. Yang, Y. Sun, Y. Wu, B. Mayers, B. Gates, Y. Yin, F. Kim, and H. Yan, Adv. Mater. **15**, 353 (2003).
[50] P. B. Allen, Nano Lett. **7**, 6 (2007).
[51] R. D. James, J. Mech. Phys. Solids **54**, 2354 (2006).
[52] O. O. Kit, L. Pastewka, and P. Koskinen, Phys. Rev. B **84**, 155431 (2011).
[53] P. B. Allen, Nano Lett. **7**, 11 (2007).
[54] T. Dumitrica and R. D. James, J. Mech. Phys. Solids **55**, 2206 (2007).
[55] A. Aghaei and K. Dayal, J. Appl. Phys. **109**, 123501 (2011).
[56] A. Aghaei, K. Dayal, and R. S. Elliott, J. Appl. Phys. **113**, 023503 (2013).
[57] C. White, D. Robertson, and J. Mintmire, Phys. Rev. B **47**, 5485(R) (1993).
[58] P. B. Allen, Nano Lett. **7**, 1220 (2007).
[59] V. N. Popov, Mater. Sci. Eng. R Rep. **43**, 61 (2004).
[60] V. N. Popov and L. Henrard, Phys. Rev. B **70**, 115407 (2004).
[61] D.-B. Zhang and T. Dumitrica, Appl. Phys. Lett. **93**, 031919 (2008).
[62] D.-B. Zhang, R. James, and T. Dumitrica, Phys. Rev. B **80**, 115418 (2009).
[63] P. Koskinen and O. O. Kit, Phys. Rev. Lett. **105**, 106401 (2010).
[64] D.-B. Zhang and S.-H. Wei, npj Comput. Mater. **3**, 1 (2017).
[65] L. Yue, G. Seifert, K. Chang, and D.-B. Zhang, Phys. Rev. B **96**, 201403 (2017).
[66] D.-B. Zhang, X.-J. Zhao, G. Seifert, K. Tse, and J. Zhu, Natl. Sci. Rev. **6**, 532 (2019).
[67] T. Ono and K. Hirose, Phys. Rev. B **72**, 085115 (2005).
[68] Y. Akai and S. Saito, Physica E Low Dimens. Syst. Nanostruct. **29**, 555 (2005).
[69] T. Ono and K. Hirose, Phys. Rev. Lett. **94**, 206806 (2005).
[70] A. S. Banerjee and P. Suryanarayana, J. Mech. Phys. Solids **96** (2016).
[71] S. Ghosh, A. S. Banerjee, and P. Suryanarayana, Phys. Rev. B **100**, 125143 (2019).
[72] A. S. Banerjee, arXiv preprint arXiv:2008.02267 (2020).
[73] N. D. Mermin, Phys. Rev. **137**, A1441 (1965).
[74] A. Sharma and P. Suryanarayana, J. Chem. Phys. **149**, 194104 (2018).
[75] R. McWeeny, *Symmetry: An introduction to group theory and its applications* (Courier Corporation, 2002).
[76] W. Hackbusch, *Elliptic differential equations: theory and numerical treatment*, vol. 18 (Springer, 2017).
[77] T. T. Tung and R. L. Laurence, Polym. Eng. Sci. **15**, 401 (1975).
[78] M. Hoffmann-Ostenhof, T. Hoffmann-Ostenhof, R. Ahlrichs, and J. Morgan, in *Mathematical Problems in Theoretical Physics*, edited by K. Osterwalder (Springer Berlin / Heidelberg, 1980), vol. 116 of *Lecture Notes in Physics*, pp. 62–67.
[79] R. Ahlrichs, M. Hoffmann-Ostenhof, T. Hoffmann-Ostenhof, and J. D. Morgan, Phys. Rev. A **23**, 2106 (1981).
[80] K. Hirose, T. Ono, Y. Fujimoto, and S. Tsukamoto, *First-principles calculations in real-space formalism* (2005).
[81] D. Hamann, Phys. Rev. B **88**, 085117 (2013).
[82] N. Troullier and J. L. Martins, Phys. Rev. B **43**, 1993 (1991).
[83] E. B. Barros, A. Jorio, G. G. Samsonidze, R. B. Capaz, A. G. Filho, J. M. Filho, G. Dresselhaus, and M. S. Dresselhaus, Phys. Rep. **431**, 261 (2006).
[84] A. Jorio, G. Dresselhaus, and M. S. Dresselhaus, *Carbon nanotubes: advanced topics in the synthesis, structure, properties and applications*, vol. 111 (Springer Science & Business Media, 2007).
[85] D. A. Mazziotti, Chem. Phys. Lett. **299**, 473 (1999).
[86] P. Suryanarayana and D. Phanish, J Comput. Phys. **275**, 524 (2014).
[87] A. Sharma and P. Suryanarayana, Chem. Phys. Lett. **700**, 156 (2018).
[88] F. Gygi and G. Galli, Phys. Rev. B **52**, R2229 (1995).
[89] H. J. Monkhorst and J. D. Pack, Phys. Rev. B **13**, 5188 (1976).
[90] P. P. Pratapa and P. Suryanarayana, Chem. Phys. Lett. **635**, 69 (2015).
[91] A. S. Banerjee, P. Suryanarayana, and J. E. Pask, Chem. Phys. Lett. **647**, 31 (2016).
[92] S. Kumar, Q. Xu, and P. Suryanarayana, Chem. Phys. Lett. **739**, 136983 (2020).
[93] Y. Zhou, Y. Saad, M. L. Tiago, and J. R. Chelikowsky, J. Comput. Phys. **219**, 172 (2006).
[94] Y. Zhou, Y. Saad, M. L. Tiago, and J. R. Chelikowsky, Phys. Rev. E **74**, 066704 (2006).
[95] Y. Zhou, J. R. Chelikowsky, and Y. Saad, J. Comput. Phys. **274**, 770 (2014).
[96] P. P. Pratapa, P. Suryanarayana, and J. E. Pask, J. Comput. Phys. **306**, 43 (2016).
[97] P. Suryanarayana, P. P. Pratapa, and J. E. Pask, Comput. Phys. Comm. **234**, 278 (2019).
[98] W. H. Press, *Numerical recipes 3rd edition: The art of scientific computing* (Cambridge university press, 2007).
[99] E. Anderson, Z. Bai, C. Bischof, S. Blackford, J. Demmel, J. Dongarra, J. Du Croz, A. Greenbaum, S. Hammarling, A. McKenney, et al., *LAPACK Users' Guide* (Society for Industrial and Applied Mathematics, Philadelphia, PA, 1999), 3rd ed., ISBN 0-89871-447-8 (paperback).
[100] J. Harris, Phys. Rev. B **31**, 1770 (1985).
[101] W. M. C. Foulkes and R. Haydock, Phys. Rev. B **39**, 12520 (1989).
[102] S. Kumar and P. Suryanarayana, Nanotechnology **31**, 43LT01 (2020).

[103] S. Kumar, D. Codony, I. Arias, and P. Suryanarayana, arXiv preprint arXiv:2010.13899 (2020).
[104] J. R. Shewchuk, *An introduction to the conjugate gradient method without the agonizing pain* (1994).
[105] J. Nocedal, Math. Comp. **35**, 773 (1980).
[106] E. Bitzek, P. Koskinen, F. Gähler, M. Moseler, and P. Gumbsch, Phys. Rev. Lett. **97**, 170201 (2006).
[107] D. Alfe, Comput. Phys. Commun. **118**, 31 (1999).
[108] K. Dayal and R. D. James, J. Mech. Phys. Solids **58**, 145 (2010).
[109] J. P. Perdew and Y. Wang, Phys. Rev. B **45**, 13244 (1992).
[110] D. M. Ceperley and B. J. Alder, Phys. Rev. Lett. **45**, 566 (1980).
[111] X. Gonze, J. M. Beuken, R. Caracas, F. Detraux, M. Fuchs, G. M. Rignanese, L. Sindic, M. Verstraete, G. Zerah, F. Jollet, et al., Comput. Mater. Sci. **25**, 478 (2002).
[112] J. P. Perdew, K. Burke, and M. Ernzerhof, Phys. Rev. Lett. **77**, 3865 (1996).
[113] V. Brázdová and D. R. Bowler, *Atomistic computer simulations: a practical guide* (John Wiley & Sons, 2013).
[114] A. R. Hall, M. R. Falvo, R. Superfine, and S. Washburn, Nat. Nanotechnol. **2**, 413 (2007).
[115] G. L. Zhao, D. Bagayoko, and L. Yang, Phys. Rev. B **69**, 245416 (2004).
[116] *The Elk Code*, http://elk.sourceforge.net/.
[117] A. R. Hall, L. An, J. Liu, L. Vicci, M. R. Falvo, R. Superfine, and S. Washburn, Phys. Rev. Lett. **96**, 256102 (2006).
[118] L. Yang and J. Han, Phys. Rev. Lett. **85**, 154 (2000).
[119] S. Sreekala, X.-H. Peng, P. M. Ajayan, and S. K. Nayak, Phys. Rev. B **77**, 155434 (2008).
[120] D. Shah, N. A. Bruque, K. Alam, R. K. Lake, and R. R. Pandey, J. Comput. Electron. **6**, 395 (2007).
[121] W. Liang, M. Bockrath, D. Bozovic, J. H. Hafner, M. Tinkham, and H. Park, Nature **411**, 665 (2001).
[122] V. Sazonova, Y. Yaish, H. Üstünel, D. Roundy, T. A. Arias, and P. L. McEuen, Nature **431**, 284 (2004).
[123] D.-B. Zhang, R. James, and T. Dumitrica, J. Chem. Phys. **130**, 071101 (2009).
[124] T. Cohen-Karni, L. Segev, O. Srur-Lavi, S. R. Cohen, and E. Joselevich, Nat. Nanotechnol. **1**, 36 (2006).
[125] Z. Ren and P.-X. Gao, Nanoscale **6**, 9366 (2014).
[126] D. Codony, I. Arias, and P. Suryanarayana, arXiv preprint arXiv:2010.01747 (2020).
[127] M. Springolo, M. Royo, and M. Stengel, arXiv preprint arXiv:2010.08470 (2020).
[128] S. Ghosh and P. Suryanarayana, J. Comp. Phys. **307**, 634 (2016).
[129] T. Dumitrică, C. M. Landis, and B. I. Yakobson, Chem. Phys. Lett. **360**, 182 (2002).
[130] A. Natan, A. Benjamini, D. Naveh, L. Kronik, M. L. Tiago, S. P. Beckman, and J. R. Chelikowsky, Phys. Rev. B **78**, 075109 (2008).
[131] D. C. Rapaport, *The art of molecular dynamics simulation* (Cambridge university press, 2004).
[132] W. Davis, R. Slawson, and G. Rigby, Nature **171**, 756 (1953).
[133] X. Chen, S. Zhang, D. A. Dikin, W. Ding, R. S. Ruoff, L. Pan, and Y. Nakayama, Nano Lett. **3**, 1299 (2003).
[134] Though 1D nanostructures subject to applied twists can be considered as chiral, this term in the current work is used to represent the internal twist of the system, as per the standard nomenclature adopted in literature.
[135] Dipole moments are ubiquitous in 1D nanostructures as a consequence of the flexoelectric effect, which represents a two-way coupling between strain gradients and polarization.